OMX – A Novel High Speed and High Resolution Microscope and its Application to Nuclear and Chromosomal Structure Analysis

DISSERTATION

zur Erlangung des akademischen Grades
doctor rerum naturalium
(Dr. rer. nat.)
im Fach Biologie

eingereicht an der
Mathematisch-Naturwissenschaftlichen Fakultät I
Humboldt-Universität zu Berlin

von
Herr Dipl.-Phys. Haase Sebastian
geboren am 02.11.1974 in Stadthagen

Präsident der Humboldt-Universität zu Berlin:
Prof. Dr. Christoph Markschies

Dekan der Mathematisch-Naturwissenschaftlichen Fakultät I:
Prof. Dr. Christian Limberg

Gutachter:

1. Prof. Dr. Harald Saumweber
2. Prof. Dr. Zvi Kam
3. Prof. Dr. Heinrich Leonhard

eingereicht am: 25. Juni 2007
Tag der mündlichen Prüfung: 6. Dezember 2007

DEDICATED TO LIZ

Für den Rest meines Lebens will ich
nachdenken, was Licht ist.
(Albert Einstein im Jahre 1916)

Contents

Summary **v**

Zusammenfassung **vii**

Preface and acknowledgments **1**

I Introduction **3**

1 History of microscopy **5**

2 Why build a new microscope ? **8**

3 The resolution of a microscope **10**

- 3.1 Image degradation 10
- 3.2 Optics theory 11
- 3.3 How to improve resolution ? 13
- 3.4 Structured Illumination Microscopy 14

II Conception and implementation of a new microscope **17**

4 Building a new microscope **19**

- 4.1 Built in-silico 20
- 4.2 Layout of the OMX-room 24
- 4.3 The microscope body 24
- 4.4 Microscope optics 26
- 4.5 OMX laser excitation 28
- 4.6 Structured Illumination (SI) 30
- 4.7 CCD cameras 31
- 4.8 Sample stage 33
- 4.9 Computer infrastructure 33
  - 4.9.1 Camera PCs 36

4.9.2 Motor PC 36
4.9.3 The digital signal processor (DSP) 36
4.9.4 DSP host-PC 37
4.9.5 Main user interface: three panel control screen 37
4.10 LMX: navigation station 39

5 Operation of the microscope 41
5.1 Pre-scanning of sample slide 41
5.2 High resolution microscopy 42
5.2.1 3D stacks of one or more fluorophores 45
5.2.2 3D projections of one or more fluorophores 45
5.2.3 Structured Illumination (SI) 46
5.2.4 '2 $^{1}/_{2}$ D' (stereo) imaging 46

6 OMX requires new software 47
6.1 Data analysis software 49
6.2 The Priithon package 50

III Results 55

7 Flat-field correction 57

8 Acquisition and conditioning of a PSF 60

9 Fluorescent beads in SIM 64

10 Chromosome dynamics 68
10.1 Dosage compensation complex 69
10.2 Densely sampled 4D data 71
10.3 High signal-to-noise in 3D projections 72
10.4 Semi-automatic tracking 72
10.5 Visualizing 4D data 77
10.6 Model-based motion analysis 79

11 Chromosome structure in SIM 82
11.1 Anaphase chromosome structure 83

12 Polytene chromosomes in SIM 89

13 Nuclear pores in SIM 94

IV Discussion 99

14 Ultra-high resolution microscopy 101

15 Application of SIM 104
15.1 Higher resolution of polytene banding patterns 104
15.2 Higher resolution of nuclear pores 105

16 Chromosome structure 107

17 Chromosome dynamics 111

18 Further remarks 114
18.1 Multi color alignment 114
18.2 Spectral overlap – bleed-through correction 114
18.3 Deconvolution and PSFs 115
18.4 Software development 116
18.5 Andor iXon EMCCD cameras 117
18.6 LMX 118
18.7 Flat fielding 119
18.8 Mechanical stability 119
18.9 2 $^1/_2$ D imaging mode 120
18.104D model-based motion dynamics of interphase chromatin . . 120

19 Materials and methods 122
19.1 Building the OMX microscope 122
19.2 Protocol for isolation of *Drosophila* primary cell cultures . . . 125
19.3 Protocol for staining *Drosophila* salivary gland squashes . . . 127

Appendix 130

Abbreviations 130

Bibliography 139

Curriculum Vitae 142

Selbstständigkeitserklärung 144

Summary

We have designed and implemented a novel fluorescence 3D wide-field light microscope called OMX: Optical Microscope eXperimental. Not based on prior microscopes, crucial design changes have been implemented to address improved speed and resolution requirements of current biology research. The microscope stand is a complete redesign to provide better mechanical and temperature stability. Stage motion is computer controlled. The microscope body is housed on an optical table inside a small "walk-in cabin" that is completely dark and features clean-room quality air. It does not have an eyepiece, but instead for focusing and finding an object the computer provides a real-time image on the screen. It uses four lasers as illumination sources for their superior light output intensity and it can image up to four emission wavelengths simultaneously.

After designing and building the microscope body I designed and implemented the needed computer software for the eight computers required to operate OMX. Most of that implementation happened while biologists in our lab were already using OMX for their research. This arrangement provided invaluable feedback, so that I could add features the way they were most practical and helpful to conduct experiments. Over the course of the project I also designed and implemented a new Open-Source software platform for algorithm development and image analysis. It focuses on very large multi-dimensional image data handling and visualization in general.

OMX can operate in two modes: a) fast speed for live imaging and b) ultra-high resolution Structured Illumination. In the first mode a live specimen can be observed at a resolution up to the Abbe diffraction resolution limit (approx. 250 nm) at speeds up to 100 sections per second simultaneously in multiple wavelength channels. This equals about 10 3D images per second (10 .4μm sections for a 4 μm stack). The second mode is for observing fixed preparations at resolutions below the Abbe diffraction limit. This is achieved by computationally combining multiple exposures acquired using Structured Illumination Microscopy (SIM). This produces 3D volumetric image data with lateral resolution near 100 nm and axial resolution of about 200 nm as demonstrated for model objects. Various biological samples imaged using this modality prove that SIM is bridging the gap between the high resolution of electron microscopy and the high labeling specificity of conventional epifluorescence light microscopy.

In the second part of this thesis I show first results achieved using the OMX microscope. Chromosome dynamics is analyzed using various newly developed image analysis algorithms. Sub-second motion was observed for *in situ Drosophila* X chromosomes tagged with a GFP-MSL3 construct. Parts of the chromosome could be traced within the nucleus and time-series data shows its folding and unfolding as a function of time. Chromosome structure was imaged using SIM on formaldehyde fixed primary embryonic cultures stained with DAPI. Features of the sub-structure with sizes around 100–200 nm were apparent. Many chromosomes show an outer layer along the chromatin axis appearing persistently denser in DNA than the central core. Polytene chromosomes were imaged using SIM. Band patterns are visible in much more detail than in conventional deconvolution microscopy and longitudinal fibers – known only from electron microscopy – were visible. As another example of the improved resolution of SIM nuclear pores were imaged. Mouse cells stained with DAPI show dark circular holes, $\approx 120\,\mathrm{nm}$ in size, in the nuclear envelope colocalized to a nuclear pore specific protein.

Zusammenfassung

Im Rahmen dieser Arbeit wurde ein neuartiges 3D Fluoreszenz Mikroskop entworfen und gebaut. Es heißt OMX, “Optical Microscope eXperimental”. Da es nicht auf einem kommerziell verfügbaren Mikroskop aufbaut, konnte durch einen umfassenden Neuansatz den neuen Anforderungen der aktuellen Biologie bezüglich erhöhter Auflösung in Zeit und Raum Rechnung getragen werden. Mit Ausnahme vom Auflegen des Objektträgers sind alle Aspekte des Mikroskops Computer-gesteuert. Es ist in einer Dunkelkabine eingeschlossen und auf ein Okular wurde verzichtet. Dies ist nötig, um bestmögliche Temperaturstabilität und Reinraum Luftqualität zu gewährleisten. Als Lichtquelle werden vier Laser eingesetzt, mit denen es möglich ist, bis zu vier Fluorophore gleichzeitig zu beobachten.

Aus der umfassenden Automatisierung folgen erhöhte Anforderungen an die Software, um ein reibungsloses und benutzerfreundliches Arbeiten zu ermöglichen. Somit habe ich besondere Aufmerksamkeit darauf verwendet, die acht Computer, die nötig sind, um OMX zu benutzten, möglichst transparent in ein einfach zu bedienendes Gesamtsystem zu integrieren. Der Großteil dieser Arbeit fand statt, während bereits Biologen aus unserer Arbeitsgruppe das Mikroskop für ihre Untersuchungen nutzten. Dieses Arbeitsumfeld half, Systemkomponenten in einer Weise zu implementieren, dass diese sowohl einfach bedienbar sind, als auch alle benötigten Funktionen zur Verfügung stellen. Im Verlauf des OMX-Projektes, habe ich einen Großteil der Software in ein neues, eigenständiges Open-Source Projekt einfließen lassen können. Das Ziel dieses Projekts ist es, sehr große, mehrdimensionale Bilddaten zu verarbeiten und zu analysieren. Der Schwerpunkt liegt in einer flexiblen Oberfläche, um neuartige Algorithmen hierzu entwickeln zu können.

OMX hat zwei Betriebsarten: a) schnelle Lebendaufnahmen, und b) ultrahochauflösende Structured Illumination Mikroskopie (SIM). Im ersten Modus können bis zu 100 Bilder pro Sekunde mit einer Auflösung bis zum Abbe-Limit gleichzeitg in mehreren Farbkanälen aufgenommen werden. Dies entspricht z.B. 10 3D Bildern pro Sekunde (10 .4μm Schnitte für ein Volumen von 4 μm). Im SIM-Modus können fixierte Präparate mit eine Auflösung unterhalb des Abbe-Limits untersucht werden.

Im zweiten Teil dieser Arbeit, stelle ich erste Forschungsergebnisse von OMX vor. *Drosophila* X chromosomen markiert mit GFP-MSL3 wurden *in situ* im sub-Sekunden Bereich beobachtet. Mit Hilfe neuentwickelter Algorithmen konnte ich die Chromosomendynamik analysieren und Bereiche eines Chromosomen, sowie dessen Falten und Entfalten, als Funktion der Zeit darstellen. Chromosomenstrukturen wurden mit Hilfe der SIM an fixierten primären embryonalen Kulturen untersucht. Unterstrukturen von 100–200 nm sind erkennenbar. Viele Bilder zeigen eine DNA-reiche Hülle die einen DNA-armen Chromosomenkern umgibt. Ausserdem habe ich polytäne Chromosomen mit SIM aufgenommen. Bandstrukturen zeigen sich mit deutlich erhöhter Detailklarheit, und Längsfasern sind sichtbar, die ansonsten nur vom Elektronenmikroskop her bekannt sind. Als weiteres Beispiel der verbesserten Auflösungsfähigkeit habe ich Kernporen untersucht. In mit DAPI gefärbten Mauszellen zeigen diese sich als dunkle Punkte mit einer Größe von etwa 120 nm.

Preface and acknowledgments

In 2001 I joined John Sedat's Lab at UCSF in San Francisco. John proposed a project to develop a new kind of high-resolution light microscope (called OMX, Optical Microscope eXperimental) which was needed to answer biological questions that his lab and many others have come up against. It should be more light conserving and more light sensitive than other microscopes. Most of all it should be able to acquire many multi-color 3D images per second to study fast dynamics. It quickly became clear that OMX was also a good platform to incorporate a new ultra-high resolution imaging mode developed by Mats Gustafsson in John's lab (Structured Illumination Microscopy).

The first eight months of the OMX project we spent creating a *virtual* prototype of the three dimensional OMX microscope body in the computer. In the lab AutoCAD was already used for many previous projects to create professional technical drawings, but John encouraged me to learn the newest version, called AutoCAD Mechanical Desktop, which could semi-automatically generate the drawings from a 3D model. Once the many dozens of parts making up the OMX microscope were created "in silico", the parts were virtually *assembled* in the computer and we could *see* how they fit together.

The OMX microscope system includes a rather extensive computer hardware infrastructure. To develop the required software I made use of multiple novel programming technologies. Most of these are actively developed by various Open-Source communities. Rather unforeseen was the inception of a new open-source project (Priithon) which resulted quite naturally from the software modules that I used to control OMX. I consider it a large success that Erik Hom was able to use this as the sole development platform for his PhD thesis.

There were many people involved in the OMX project. John Sedat and David Agard together with Mel Jones had discussed many of its crucial features a long time before I joined. Without the support of Harald Saumweber I could not have turned this into a biology thesis. Most of all I would like to thank John for creating an always (scientifically) challenging environment and trusting me to work on a project with such a broad and interdisciplinary focus.

Lukman Winoto helped to install the laser illumination part and made crucial design contributions to the overall OMX optics. Pete Carlton gave valuable feedback as the main user of OMX. He coaches everyone who wants to put OMX to scientific use and knows how to steer them through the entire process of OMX imaging. I would like to thank Yuri Strukov for his continuous moral support and for providing and helping me with many chromosome preparations. Last but not least I was very happy to have Lin Shao on my side. He was my friend and co-student from the first day on and always demonstrated his trust in my software by using it for his own projects.

Part I

Introduction

Chapter 1

History of microscopy

Microscopy has revolutionized biology many times in history. Shortly after microscopes were invented in the first half of the 17th century [Wikipedia, 2006a; Alberts et al., 2002], Robert Hooke*(1635–1703)*, after looking at sections of cork, observed small compartments surrounded by dense structures that he called cells. He believed these special structures were empty chambers that produced the cell fluid they contained. Hooke however did not recognize yet that his observation was a general phenomenon that was common to all living organisms. Anton van Leeuwenhoek*(1632–1723)* observed many protozoa and in 1676 the first bacteria using a single-lens microscope. The internal structure of these cells was still uncharacterized due to the limited resolution of his instrument.

It took 150 years to develop more complex compound microscopes that were superior in imaging quality than van Leeuwenhoek's simple single-lens design. *Cell biology* was initiated when in 1839, Schleiden and Schwann proposed that every organism was composed of one or more cells. Thus the cell was a principle unit of all living organisms and in 1855 Rudolf Virchow proposed that all cells can only come from others cells (*"omnia cellula e cellula"*). As a consequence of the now recognized importance of cells a wake of activity was initiated. Early cytologists were interested in how cells were formed (cell division and mitosis) and they intensely studied the internal organelles of cells. This was supported by the simultaneous development of new dyes in chemistry that could be used to visualize such structures with the available microscopes.

At the same time, optics were improved in resolution by the use of oil immersion lenses, and new techniques were introduced, for example the microtome by Wilhelm His$^{(1831–1904)}$ in 1866. In 1876 Ernst Karl Abbe$^{(1840–1905)}$ analyzed the effects of diffraction on image formation and showed how to optimize microscope design[Alberts et al., 2002]. He also later stated the law of diffraction-limited resolution recognizing its dependency on the electromagnetic wavelength used. Consequently, efforts were made to use shorter wavelengths for microscopy.

Thus the invention of the electron microscope in the 1930s allowed scientists to look further inside the makeup of a cell. For the first time many sub-cellular organelles could be seen with much detail [Alberts et al., 2002]. In 1953 the Dutch physicist Frederik Zernike$^{(1888–1966)}$ received the Nobel prize for the *phase contrast* microscope that he invented a year earlier. This new imaging modality permitted imaging of internal structures of living cells without staining. Furthermore, for the first time, cells could now be grown and monitored in tissue cultures. The same year the system of *differential interference contrast (DIC)* was invented and patented by Nomarski$^{(1919–1997)}$. DIC was a major tool enabling the study of cell motility. However, phase contrast and interference contrast were again limited by the wavelength of the visible light. Electron microscopy on the other hand revealed detailed structures but could not relate them with the emerging repertoire of the various biological molecules.

In 1852 George Stokes $^{(1819–1903)}$ described the phenomenon of fluorescence. Some materials or dyes exhibit this effect: when excited with light of a certain wavelength they emit light of a longer wavelength. The difference in wavelength is called Stokes shift. This effect was put to use for the observation of biological samples by fluorescence microscopy. The first fluorescence microscopes were developed already in 1911/13 by Heimstädt and Lehmann to study autofluorescence of bacteria, protozoa, plant and animal tissues, and bioorganic substances such as albumin, elastin, and keratin. They were able to see the weak fluorescence since the strong excitation UV light was blocked by the glass optics of the eye piece. This demonstrated the ability of fluorescence microscopy to distinguish specific molecular sites in their natural environment. But to be able to image other fluorophores excited in the visible range a different way to separate the strong excitation from the very weak fluorescent emission was needed. Improved Neofluar objectives, good dichroics and sharp band-pass filters became available in the late 1960s and are still being continuously improved.

Soon, a large variety of different fluorophores were used to stain and detect specific proteins or other molecules in cells and tissues. Two common fluorescent dyes were, and still are, *fluorescein* and *Rhodamine*. In a powerful technique called immunostaining these are coupled to antibody molecules, which then serve as highly specific and versatile staining reagents that bind selectively to a particular macromolecule that they recognize inside the cell or in the extra cellular matrix [Alberts et al., 2002]. It is possible to combine different fluorophores with different antibodies to distinguish multiple types of molecules in the same cell. Small fluorophores with high affinity to well defined sub-cellular structures often supplement the staining procedures, e.g. DAPI to stain DNA.

While some dyes were usable in living cells, many fluorophores are only usable in fixed cells. Advances in genetics eventually produced green fluorescent protein (GFP) as a new live dye in the early 1990s [Prasher et al., 1992; Chalfie et al., 1994]. This was another important milestone that can not be underestimated. GFP is expressed by the living organism itself and expressed as a fusion protein makes for a very universal live-marker for essentially any target protein. In recent years a wide range of variants of fluorescent proteins emitting in different wavelengths has become available [Shaner et al., 2005; Patterson et al., 2001].

Light microscopes have been used with photographic films and cellophane movies for recording images. As soon as electronic video recording and digitized imaging technologies were available they have been applied [Inoué, 1989]. The advantages of online electronic contrasting were extremely important in transmitted light microscopy for observing low contrast features such as lamellapod activities, polarization-dependent images, etc. With increasing sensitivity of video cameras, availability of fast frame grabbers, photo-multiplication plates and the introduction of CCD cameras fluorescent microscopy turned completely digital.

Chapter 2

Why build a new microscope ?

The study of chromosome dynamics and three dimensional organization of chromosomes in the cell nucleus is giving new insights into how the genomic information is expressed at the right times of the cell cycle. However, in order to visualize and analyze molecular events within live cells dynamically, high-resolution three-dimensional images must be acquired at a very fast speed so that tagged molecular sites can be followed. Many studies in our lab (for example [Vazquez et al., 2002, 2001]) have shown first insights into how chromosome motion changes throughout the cell cycle and during development. Often it can be divided up into random Brownian and non-random directed motion. These motion types have been shown to occur on multiple time scales, some being too fast to be captured by commercially available microscopes. Further studies in chromosome dynamics require the following improvements:

Speed:	Many 3D images should be acquired on the sub second time scale possibly in multiple color channels. Current systems can only image one or a few 2D sections per seconds in a single channel.

Light conservation:	To image for longer times while minimizing photo-bleaching and related photo-toxicity light scattering has to be minimized. The optical design can be improved for higher photon efficiency and for lower stray light inside the microscope; more sensitive CCD cameras can be used.
Mechanical stability:	High resolution and fast stage motion require improved mechanical stability
Temperature stability:	To prevent stage drift during the experiment environmental conditions must be controlled.
High resolution:	To study sub-cellular structures optical resolution has to be improved.

The new OMX microscope provides multiple operating modes to address these needs:

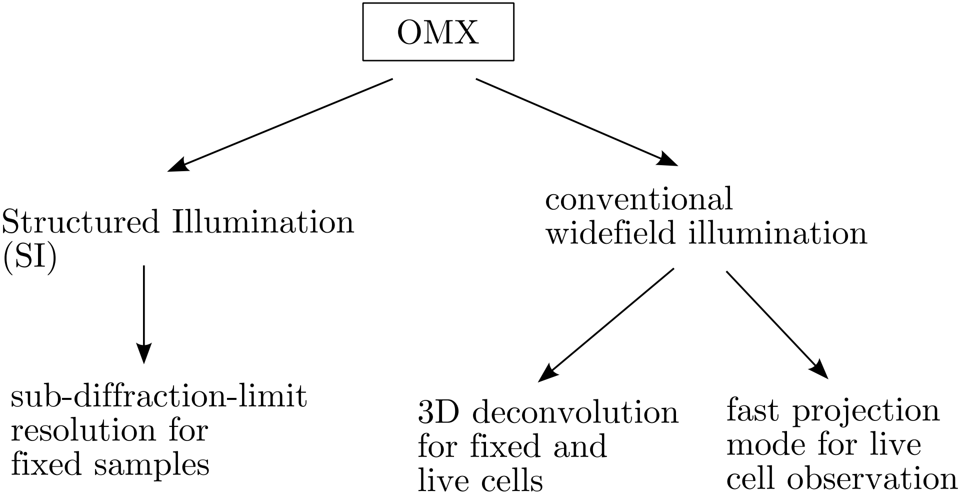

The following chapters will discuss these modes in further detail.

Chapter 3

The resolution of a microscope

Of the many tools available to the biologist for studying samples, optical fluorescence microscopy has many advantages: the possibility of in vivo imaging, low sample damage, high specificity and relative ease of sample preparation to name just a few. The biggest disadvantage compared to electron microscopy is its relatively low resolution. (>200 nm vs. <20 nm). OMX implements a novel technique called structured illumination (SI) to improve upon the resolution limit of conventional light microscopy. To explain how this is done I will give some background.

3.1 Image degradation

Ideally the image acquired by a microscope would be identical to the biological object being viewed. In reality, however, images are degraded by noise, scatter, glare and blur [Wallace et al., 2001]. *Noise* originates both from the quantum statistics of photons and from the digital imaging electronics of the CCD sensor and the electron amplifier. *Scatter* refers to the disturbance of light as it passes through the sample: Heterogeneous regions within the sample vary in refractive index diffracting portions of the light into random directions. Thicker samples generally exhibit more scatter than thin ones. The area of interest within the sample should be as close as possible to the coverslip to minimize scatter.

Glare, like scatter, refers to the random disturbances of light, however it occurs in the lenses and filters inside the microscope rather than within the sample. This is minimized by using anti-reflective coatings on optical surfaces within the imaging system. *Blur* is the nonrandom spreading of light. It is a fundamental limit of physics and if the imaging resolution is only limited by blur it is called “diffraction-limited”. The underlying theory is important for the understanding of image deconvolution algorithms and SI.

3.2 Optics theory

The 2D resolution of a microscope can be defined by the Rayleigh-limit [Abbe, 1873]:

$$R = \frac{1.22\,\lambda}{2\,NA}$$

Hence the resolution is proportional to the emission wavelength λ and is inversely linear to the numerical aperture (NA) which is given by the objective lens used . R is the distance at which two "point sources" would just be separable by the human eye. The number 1.22 comes from the Airy function describing the blur of each point source. The best possible numbers are $\lambda = 450$ nm for blue light and $NA = 1.46$ for an oil immersion lens giving an upper limit for the resolution or $R = 188$ nm [Wikipedia, 2006c].

For 3D microscopy the theory is more complex [Born and Wolf, 1980]. In practice the microscope can acquire a *3D image* of the object by varying the focus or Z position. This is called *optical sectioning.* The image of a small (sub-resolution) plastic fluorescent bead shows how every point of an object gets blurred. This image is also called the *point-spread function (PSF)* which is shown in figure 3.1a.

Blurring and resolution are better visualized using the terminology of inverse or Fourier space. Here broad (low resolution) features, which change slowly across the field of view have a low spacial frequency and are therefore represented in Fourier space by points near the coordinate system’s origin. Sharp (high resolution) features like edges or small point markers have high

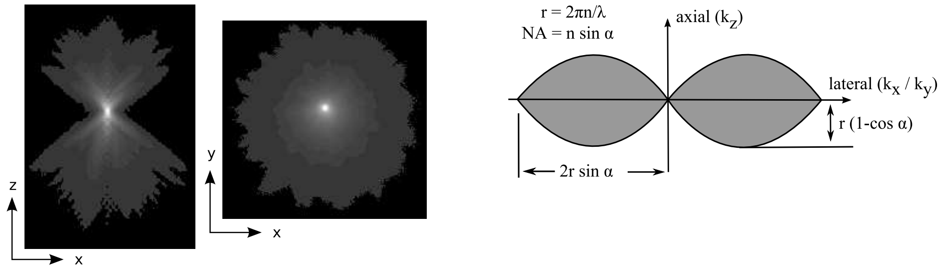

(a) (b)

Figure 3.1: The three dimensional image is a *blurred* version of the 3D object. This is quantified by the PSF or its Fourier transform, the OTF. (a) The point-spread-function (PSF) shows how every feature of the object is blurred (*real space* representation) (b) The OTF of a microscope objective lens characterizes the optical resolution in Fourier space. The area where the OTF is non-zero is called its *support*. α is the objective acceptance half-angle of light. n is the refractive index of the immersion oil. λ is the emission wavelength. NA is the numerical aperture.

spacial frequency and are represented by the points on the perimeter of Fourier space. Now the resolution limit of a microscope can be easily visualized by its object transfer function (OTF) – the Fourier transform of the PSF. Observation is possible where the OTF is non-zero, this region is called the *OTF support* (figure 3.1b). The lateral extent can be shown to be proportional to the numerical aperture (NA) of the objective and inversely proportional to the wavelength of the light. Furthermore, it can be seen that for the lateral frequencies k_x and k_y both being zero the support in the axial k_z direction vanishes. This means that if a given object has only small lateral frequencies, for example an evenly fluorescing nucleus, there is no observable structure towards Z remaining – the concept of 'optical sectioning' fails. Luckily it is possible to recover some axis resolution with the help of computational image processing: constrained iterative deconvolution [Agard, 1984; Wallace et al., 2001].

3.3 How to improve resolution ?

Over recent years many new techniques have been proposed and implemented to improve on the above described resolution limit. (see a review by Gustafsson, 1999).

The best known is laser scanning confocal microscopy [Minsky, Dec. 19, 1961]. It improves the *axial* resolution by using a pair of pinholes to physically reject the out-of-focus light. Very fast scanning of these across the 3D space of the object fills in an image, just like a TV screen builds up the picture in 2D. While there are new schemes to increase the readout speed by using more than one pinhole pair (spinning disc confocal [Wang et al., 2005]), the major drawback, that the second pinhole throws most emitted light away, stays unchanged. This restricts its usability for weakly fluorescent samples.

Another quite intuitive scheme is called SPIM: selective plane illumination microscopy [Huisken et al., 2004]. Here only a thin section of the sample gets illuminated from the side through a thin slit. Consequently, only emitted light from this section, which is at the same time the in-focus section, is imaged. This is best suited for thick samples and gives essentially isotropic resolution of up to 1 μm.

Technically more challenging schemes try to increase the axial resolution with the help of a second objective. Simply stated, if one objective can collect incoming light from a certain acceptance angle α then two opposing objectives should see “twice as much”, 2α. In fact when the sample is not only observed through the two objectives but also illuminated through both objectives the theoretically expected axial resolution is around 50 nm, or sevenfold better than conventional resolution [Gustafsson et al., 1999]. The biggest practical problem with this scheme is that the two objectives need to be perfectly aligned relative to each other. This is necessary so that the light coming from both objectives can be brought together to form the resulting interference patterns. This arrangement is also called an interferometer. A very similar approach, called 4Pi, is based on scanning confocal microscopy [Hell and Stelzer, 1992; Bewersdorf et al., 2006].

A variant that also uses two objectives, but has them geometrically oriented at 90 degrees towards each other is called Theta Microscopy [Stelzer and Lindek, 1994]. As in confocal microscopy, the emitted light is detected through a pinhole. The system resolution is more isotropic since the hourglass shaped PSF is essentially cropped by a copy of itself rotated by 90 degrees. This way the (high resolution) lateral extent of the PSF applies also in the axial direction. Two drawbacks of this imaging modality are that samples need to be mounted on a rod, since a standard slide would not allow access from the 90 degree direction, and second, only low numerical aperture (NA$\approx$.7) objectives can be used, since a large working distance is needed, so that the two objective would not run into each other. This last limitation prohibits Theta Microscopy from being used when sub-micron resolution is required.

To improve on the lateral resolution one could, in theory, use confocal microscopy [Gu and Sheppard, 1992]. However, as is discussed in Wilson (1995) a significant improvement is only achievable with a pinhole that is much smaller than the Airy disc, consequently, this means that even more light would be discarded.

Abbe's theory defining the diffraction limit of light microscopy assumes evenly (flat) illumination. In structured illumination microscopy (SIM) the lateral resolution can be increased by a factor of two [Gustafsson, 2000; Gustafsson et al., 2000]. When combining this scheme with nonlinear effects in the photo-chemistry of some fluorophores at high intensity illumination the theoretical resolution capabilities become unlimited [Gustafsson, 2005]. However, this last step has so far only been demonstrated with plastic beads that were imaged resulting in a resolution of 59 nm.

3.4 Structured Illumination Microscopy

OMX implements an extended 3D version of SIM [Gustafsson et al., 2007; Shao, 2005]. This method increases both the lateral and the axial resolution by a factor of two. It is light conserving since it is a wide-field method and does not discard any emission photons. Images are acquired in conventional wide-field mode while the illumination source features an imprinted stripe

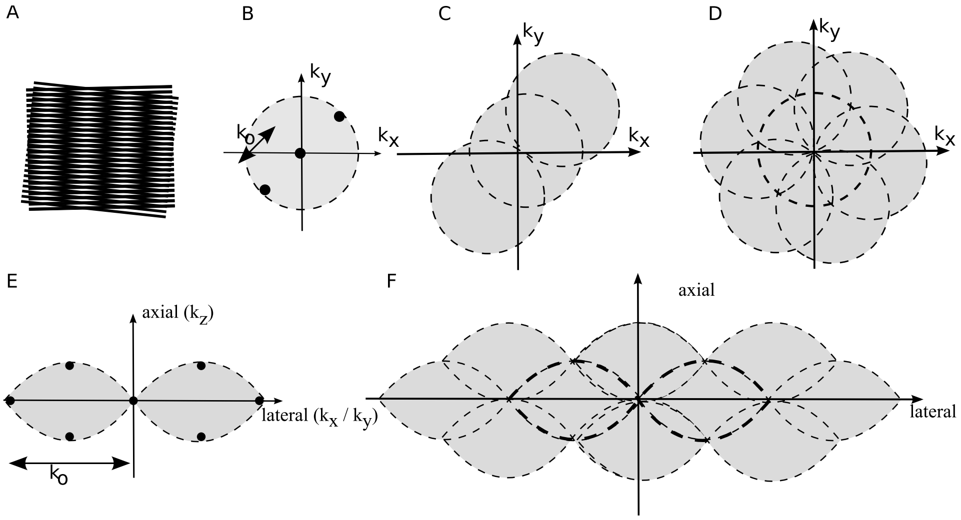

Figure 3.2: Structured illumination is based on a principle analogous to the commonly known *Moiré Fringes*. See explanation in main text.

pattern. The underlying principle is analogous to *Moiré Fringes*: The illumination pattern is right *at* the diffraction limit and the sample features are partially even *below* the diffraction limit. The resulting Moiré pattern encodes the sub-resolution information so that they can be observed at and above the diffraction limit.

Figure 3.2 demonstrates how SIM increases the lateral resolution beyond the diffraction limit. 3.2a shows the Moiré Fringes as apparent vertical broad lines resulting from two sets of finer (high resolution) stripes. To better visualize what happens in SIM the following argument is done in Fourier space. Conventional microscopy is limited to frequencies within the observable region dictated by Abbe‘s law (shaded circle in 3.2b). In 2D SIM the sinusoidally striped illumination pattern has only three Fourier components which themselves also have to lay inside that region (point markers in 3.2b). When an arbitrary sample object is illuminated using SIM the objects *real-space* image multiplies with the stripe pattern. In *frequency-space* this multiplication translates into a convolution of the image with the three points defining the stripe pattern. This essentially adds new area to what is observable towards the direction of the stripes 3.2c. When the stripe pattern is rotated by 120 ° another direction is added. With a total of three angles this effectively fills a larger circle defining the new observable region of twice the resolution limit (3.2d).

In 3D SIM a more complex sinusoidal strip pattern is used. Here the strips extend not only in the x-y-plane (as was the case for the three dots in figure 3.2b, but it consists of 7 points extending also into the z direction (figure 3.2e). This results both in twice the lateral resolution (as in 2D SIM) and also in physical (not deconvolution based) optical sectioning at an axial resolution of about 200 nm (figure 3.2f). The increased pattern complexity requires exposing each stripe orientation with 5 different phase-shifts to ensure that the resulting data can be mathematically decomposed into the constituting high-resolution parts. To be able to computationally reconstruct a high-resolution 3D-SIM data set, each Z-section requires 15 exposures: 5 phases times 3 angles. The sections have to be taken not more than .125 μm apart, resulting in a total data stack of about 1000 images for an 8 μm sample volume.

Part II

Conception and implementation of a new microscope

Chapter 4

Building a new microscope

The OMX microscope is a new microscope design that diverts from any existing platform. A fresh design was necessary to incorporate the various features required to perform fast multi-wavelength, high-resolution biology experiments. Building on the experience gained from previous microscope designs in our lab, OMX shares some aspects with a previous design called *OM1* (Optical Microscope 1)[1].

OMX is a wide-field 3D deconvolution microscope. It uses multiple lasers instead of an arc-lamp as an excitation light source. A novel optical dichroic design transmits the excitation light path while reflecting the emission wavelength bands. To be able to image up to four wavelengths at once a filter wheel is not used. Instead a train of different dichroics selects the different color channels (see section 4.4). To minimize glare all optical surfaces have anti-reflective coating. Stray light inside the microscope is also minimized by enclosing the entire light path with sand-blasted metal tubes. Furthermore, all parts are black anodized. All optical components that are specific to the set of color channels used are attached to an exchangeable optics-drawer module. This facilitates using a different set of four color channels by simply switching the optics drawer.

The most striking new features of OMX are:

- The microscope is enclosed in a "walk-in cabin": this provides clean

---

[1] The DeltaVision deconvolution microscope is the result of the technology transfer of OM1 to Applied Precision Instruments.

room quality air, ensures complete darkness during data acquisition and controls environmental parameters like temperature and noise.

- The omission of an objective turret: To provide better mechanical stability and better optical alignment OMX has only a single high numerical immersion objective installed. It is mounted in a ceramic ring and can be easily exchanged for a lens with a different magnification and for a different immersion medium.

- The omission of an eye-piece: To ensure a clean environment and optimize the optical design OMX does not provide for an eye-piece. Instead a real-time digital computer display provides the needed feedback. This has many advantages, like image enhancement and better ergonomics for the microscopist.

After manually loading the sample onto the microscope stage all further operations are computer controlled. The stage is moved in X,Y and Z by micro-stepper motors. In addition, for very fast short range motion piezo actuators can be used. Images are recorded with four cooled scientific grade CCD cameras. For very low signals these feature a low noise electron multiplication mode. The work is split up between multiple computers, which is required both for computing speed and to provide a more flexible modular computer infrastructure.

Sample finding is supported by a second conjugated low magnification microscope (LMX) which is described in section 4.10. OMX implements the structured illumination (SI) sub-resolution technique. Furthermore, a DIC module adds transmitted Nomarski illumination. The design also allows the addition of a TIRF module, and a FRAP and FLIP module.

4.1 Built in-silico

The machining of parts requires accurate and detailed technical drawings. Every part, every distance and every screw hole needs to be carefully specified. Each drawing of a part consists of multiple *orthogonal views* showing the part from different angles. A 3D parameterized computer aided design

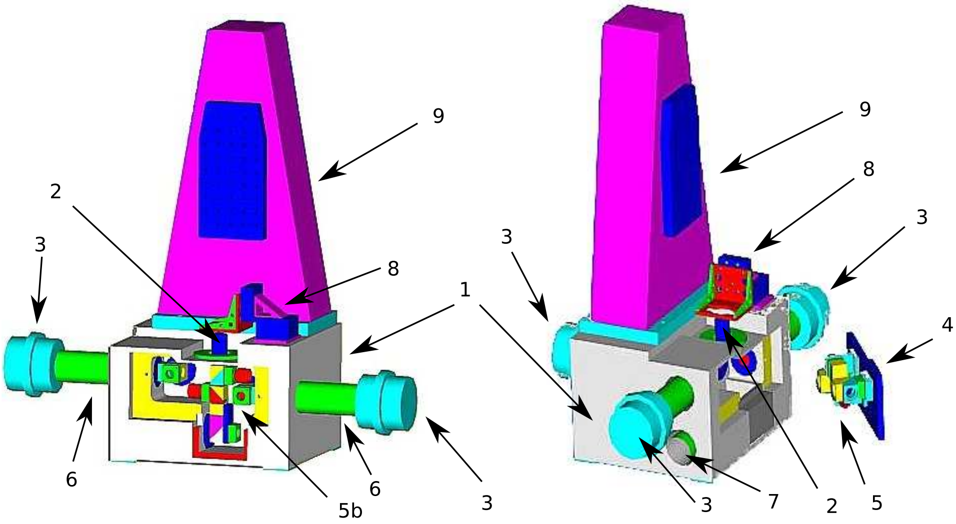

Figure 4.1: 3D rendering of in-silico version of the OMX microscope body. All parts were modeled as accurately as possible allowing cross-checks on how they fit together. The optics parts visible inside the microscope (left rendering) are in reality attached to the drawer front plate. 1: aluminum body; 2: objective; 3: CCD cameras (one left and right, two on the back); 4: optics drawer; 5: filter and dichroic holders attached to drawer; 5b: same as 5, but front plate not drawn; 6: tube lens assembly; 7: entrance hole for excitation (tube lens not shown); 8: sample x-y-z-stage (attached motors and piezos not shown); 9: "Z-tower" to hold DIC-optics

(CAD) software (AutoCAD Mechanical Desktop, version 5) was used to create a 3D model in the computer. The drawings were generated from this semi-automatically.

Figure 4.1 shows a rendering of the in-silico assembled microscope. The center piece is a sturdy block of massive aluminum. The large "tower" on top of it is for holding the DIC optics (not shown) in place. It is a motorized Z-stage that can move 15 cm upwards to provide access to the sample stage. Four CCD cameras are attached each to an Olympus tube lens: two towards the left and right and two towards the back. All main opto-mechanical components are mounted to a "drawer module". Figure 4.2 shows a rendering of the optics-drawer assembly. About 50 different parts are fit tightly together. The software aligns them according to constraints that I had to specify. For example: part A and part B are screwed together at screw hole S, and part C is then perpendicular to the bottom edge (E) of part B, . . .

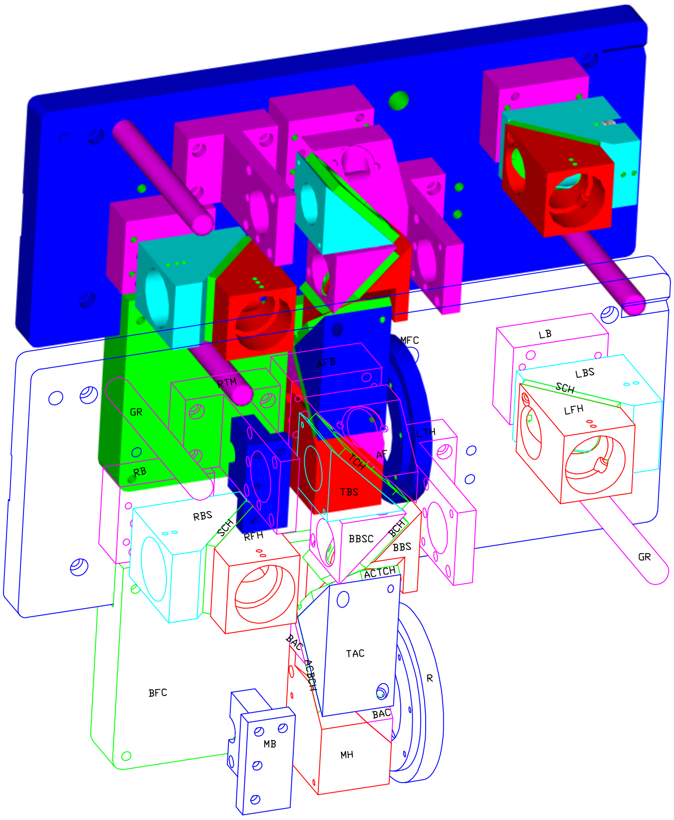

Figure 4.2: The optics drawer is made up of more than 40 parts. The 3D computer model helped to ensure that no part would run into another part. GR: guide rod; LB, RB, MB, AFB: left, right, mirror, auto-focus block; LTM, RTM: left, right 'T' mount; MFC, BFC: main, bottom front cover; LFH, RFH: left, right filter holder; LBS, RBS, TBS, BBS: left, right, top, bottom beam splitter holder; BBSC: bottom beam splitter cover; SCH, TCH, BCH, ACTCH, ACBCH: side, top, bottom, AC-top, AC-bottom "cheese"; TAC, BAC: top, bottom AC; R: ring (to hold tube lens); AF: auto-focus beam splitter holder; MH: mirror holder (AC: astigmatism correction)

A representative technical drawing is shown in figure 4.3. The CAD software generates the plot semi-automatically showing the part, in this case the bottom beam splitter holder, with all necessary dimensions and from multiple viewing angles.

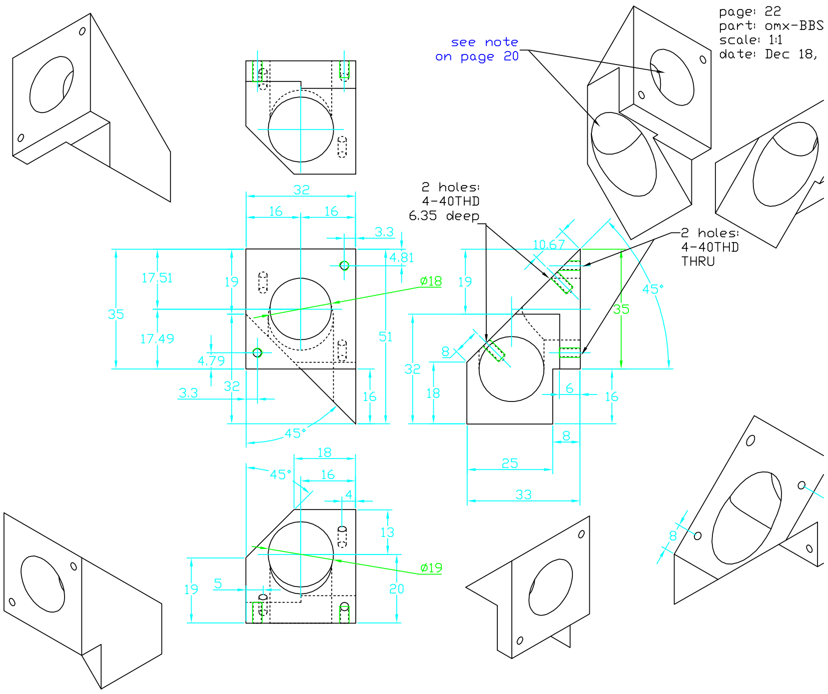

Figure 4.3: As an example the technical drawing of one of the beam-splitter holders is shown. To be able to machine the part it is required that all distances and sizes are carefully "dimensioned". Edges that would be obscured have to be drawn as dashed lines by convention. Every screw hole needs careful specifications. The original drawing was printed slightly bigger at the exact scale of 1:1 – all units are given in `mm`.

4.2 Layout of the OMX-room

Many computers, lasers, optical tables, computer screens, a ‘walk-in cabin’ and a separate (low magnification) dissection microscope (LMX) make up the *OMX microscope system*. Figure 4.4 shows how we have them placed in the ‘OMX room’ at UCSF. The most important feature of OMX, and likely most novel, is that the actual microscope is completely enclosed in a dark, clean, temperature controlled cabin. All heat or vibration producing hardware is carefully kept *outside* of that cabin. (The only exceptions are the Nanomovers and the CCD camera – but even the camera water cooling is outside the cabin). This is important to ensure a steady sample and minimize drift during data collection. The laser light sources are also kept away, and the excitation light is brought into the microscope via long optical fibers. An important side-effect of those fibers is that they reduce the coherence of the laser light.

4.3 The microscope body

High resolution microscopy puts special requirements on the mechanical stability of the microscope. The OMX microscope is placed on an air-buffered optical table. Active feedback compensates for low frequency vibrations. The whole microscope and table is housed in a walk-in cabin. The inside of the cabin features clean room quality air. It also ensures complete darkness, acoustical isolation and temperature stability during data acquisition.

Related to the microscope being placed in a separated cabin is the fact that OMX provides no eye piece. This essentially follows the same direction already taken by astronomers: they don’t look through the telescope by eye, instead all images are digitally recorded. Besides allowing the biologist to sit in a comfortably lit room, this is the only way to ensure the desired environmental control. Furthermore, stability requires not having a objective turret: only a single objective is mounted on OMX at any given point in time. According to the application it can easily be changed together with its mount.

The microscope body is made of a sturdy block of stress-relieved 7075

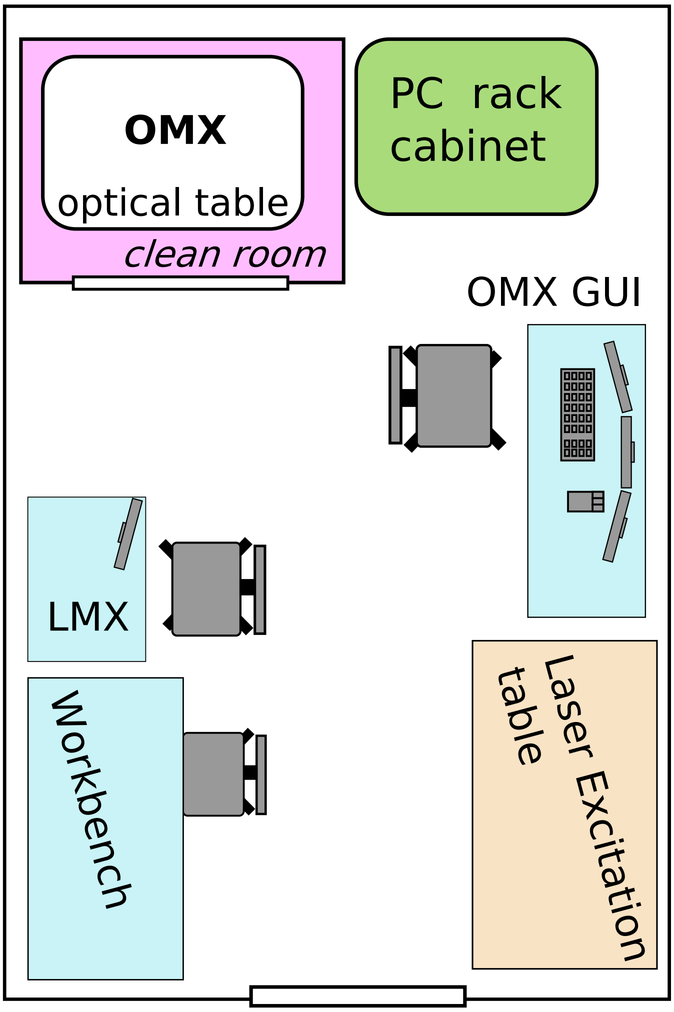

Figure 4.4: The many components of the OMX microscope system are not just *randomly* placed. Heat and vibration is one concern. The entire experiment is controlled from the desk showing the graphical user interface (GUI) on the three panel display. The sample is mapped on the LMX microscope which is controlled either by touch screen or remote control (not shown). All computer and controller hardware is housed in the PC rack cabinet. Some short cables require that it is close to the OMX microscope. The microscope is separated off inside a closed “walk in cabin” or “mini clean room”. The laser light sources are placed on their own dedicated optical table – long fiber optics cables (not shown) feed the light into the OMX microscope. Extra room is taken up by a miscellaneous workbench.

aluminum. All parts are non-glossy black anodized to minimize stray light. The objective sits in a ceramic ring which is kinematically mounted in the microscope body. The ceramic used is Zerodur made by Schott AG, which is known for its exceptional temperature stability: it has a nearly zero thermal expansion and is commonly used by astronomers both for earthbound and for orbital telescope mirror substrates [Schott AG, 2006].

The same ceramic is used for the slide holder. This is to ensure minimal drift during data acquisition. For example when the sample is heated to 37 °C the slide and the objective would drift by many microns if the temperature change were to reach the aluminum parts. The top of the microscope body makes the stand for the "Z-tower" which holds the DIC optics (see end of next section).

4.4 Microscope optics

To be able to acquire up to four wavelengths simultaneously OMX uses a new kind of reflective dichroic mirror, where the exciting beam is transmitted through the mirror, and each color image is reflected out of the emission light path and through a single-band emission filter into a separate camera. Most commercially existing microscopes choose to reflect the excitation beam on the dichroic mirror into the optical path. Then the emission is being transmitted through the dichroic, which imposes less stringent optical flatness on the dichroic manufacturing.

Figure 4.5 shows a schematic view of the light paths inside the OMX microscope body. The excitation laser light is coupled out of the incoming fiber. A silver coated mirror reflects the light stream upwards, through two dichroics into the microscope objective. The sample emits the fluorescent light back through the objective onto a cascade of different dichroics. First the long (redder) wavelengths get reflected out to the left, while the shorter (bluer) ones get transmitted down and then reflected to the right. For each group a second dichroic splits the light again, so that a total of four wavelength bands are distinguishable. Before each of these color channels gets imaged onto its dedicated CCD it is filtered by a narrow band emission filter.

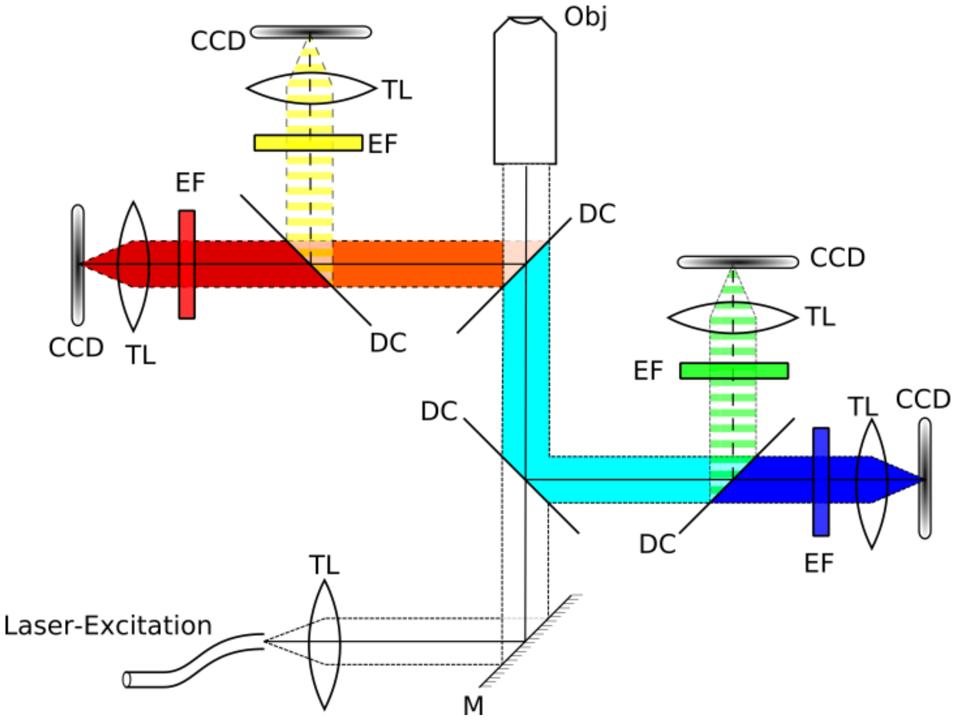

Figure 4.5: In contrast to all commercially available microscope systems, the OMX optics transmits the excitation path, and reflects the emission path.
CCD: CCD camera, *DC* dichroic, *EF*: emission filter, *M*: mirror, *Obj*: objective, *TL*: tube lens

All dichroics are mounted on tilt stages that can be adjusted by access from outside the fully assembled microscope. Together the stages and the dichroics are attached to a sturdy *front plate* making up the OMX *optics drawer* module (see figure 4.2). The user can exchange the drawer module easily — by loosening two screws — when he/she wants to use a different set of dichroics (different set of imaging colors). The drawer is reliably positioned by a three-point kinematic mount which ensures reliable optical alignment when drawers are exchanged.

The objective screws into a standard C-mount in a three-point kinematically mounted ring. As already mentioned this ring is made of Zerodur to ensure the best possible temperature stability. To minimize stray light and internal reflections all optical surfaces have anti-reflective coating. Unused reflection beams are trapped by special beam traps.

To provide a complementary mode of imaging a DIC system was added to OMX. Its light source is mounted on a vertical computer controlled stage sitting on top of the OMX aluminum body as indicated in figure 4.1. Its fast and precise motor can move all condenser DIC components 15 cm upwards within 3 seconds to quickly allow free access to the slide mount. When the DIC mode is active it brings the condenser within 4 seconds back into focus with 0.1 μm accuracy. The DIC system supports both air and oil immersion condensers.

Listed below are the two optics drawers currently in use on OMX:

Drawer A:

Emission wavelength (central)	Spectral width	Application
450 nm	60 nm	DAPI
515 nm	25 nm	FITC
590 nm	40 nm	Rhodamine
685 nm	30 nm	CY5

Drawer B:

Emission wavelength (central)	Spectral width	Application
505 nm	20 nm	GFP
540 nm	25 nm	YFP
605 nm	50 nm	RFP
700 nm	70 nm	DIC

4.5 OMX laser excitation

Situated on a separate optical table outside the OMX-cabin are four strong lasers. The different laser wavelengths together with common fluorophores that can be excited with them are:

Wavelength	Application	Laser output power
405 nm	DAPI	50 mW
488 nm	FITC, Alexa488, GFP,YFP, ...	200 mW
532 nm	Rhodamine (also works for Cy5)	2 W
650 nm (soon)	Cy5	$\approx$ 500 mW

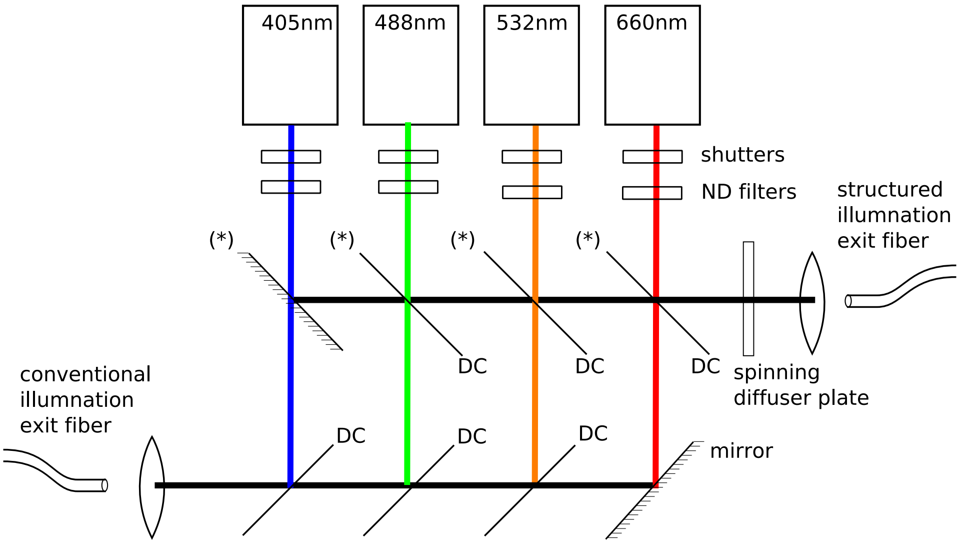

Figure 4.6: Instead of an arc-lamp, the OMX design utilizes solid-state lasers. Four different wavelengths are available. The dichroics marked with (∗) are mounted on a flip-mount that can precisely flip them in and out of the light path — ‘in’ for SI, ‘out’ for conventional illumination source

A schematic diagram showing the layout of the lasers and how they feed into the two different excitation fibers is shown in figure 4.6. Each laser beam is interrupted by a fast mechanical shutter. It is then focused through an ND filter of selectable strength. Laser light is often used because of its remarkable spacial and temporal coherence characteristics. We however want to use lasers in wide-field microscopy because of their superior total light output, and the coherence would produce a speckle pattern rendering any resulting image useless. Therefore the light beam is scrambled by a fast rotating wheel of a transparent phase scrambling surface (spinning holographic diffuser plate). Furthermore, the light beam is guided through an optical fiber of sufficient length to remove most remaining coherence. This ensures that the sample is illuminated evenly across the field of view [Kam et al., 1993].

Computer controlled flip mirrors (dichroics) can switch the special SI optics in and out of the light path. It takes about 1 second to change from one position to the other. Both the up and the down position is reached in a very repeatable and reproducible manner. All four mirrors change in synchrony with two more mirrors that are situated in the OMX cabin (not shown).

4.6 Structured Illumination (SI)

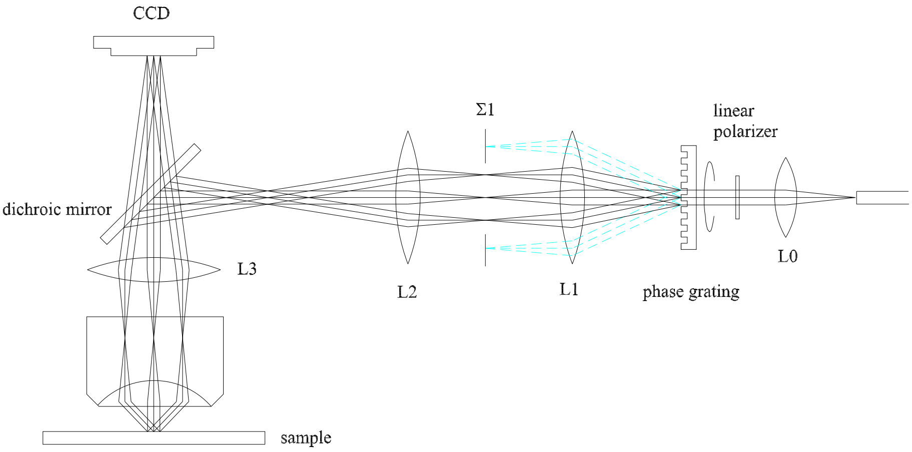

Figure 4.7: The 3D structured illumination optics. Illumination light is relayed into the system through a multi-mode optical fiber, collimated by lens L0, S polarized, and diffracted by a phase grating placed at a secondary image plane. Only diffraction orders 0, +1, and -1 are allowed to pass on to illuminate the sample as three plane waves, which then interfere to form both lateral and axial sinusoidal patterns. (Plane Σ1 is conjugate to the objective lens' back focal plane.) The phase grating, together with the polarizer, can be rotated around the optic axis so that any orientation of the lateral pattern can be generated. The phase grating is also transversely driven by a piezoelectric actuator so as to change the phase of the lateral pattern, which is necessary for raw data separation [Shao, 2005]. (To simplify the diagram excitation is drawn as being reflected on the mirror – this is not the design used in OMX.)

OMX implements an extended 3D version of 2D SIM: structured illumination microscopy (see section 3.3). OMX can acquire SI data sets exiting fluorophores with 405, 488 and 532 nm so that very high resolution images can be acquired of triple stained samples, using stains such as DAPI, Alexa488 and Rhodamine. SI imaging can be done using either the 100x 1.4NA oil or a 60x 1.2NA water objective.

In this scheme the light exiting the fiber is collimated, linearly polarized, and then directed onto a linear transmitting phase grating, which diffracts the beam into several orders. A beam block discards all but the -1, 0 and +1 orders. The grating is designed to have about 75% of the incoming laser power in these three orders, with order 0 getting 80% of this. The three orders are refocused to form an image of the fiber end face in the back focal plane of the objective lens. A schematic diagram of this setup is shown in Figure 4.7. To be able to acquire all needed phases and angles the grating is mounted on a piezoelectric actuator which is close-loop controlled using a self designed capacitive distance sensor. The actuator in turn is mounted on a motorized rotation stage.

4.7 CCD cameras

The OMX microscope uses modern scientific grade [Hiraoka et al., 1987], cooled electron multiplication charged coupled devices (EMCCD [Wikipedia, 2006d]). The cameras are made by Andor Technology, who uses the 'L3Vision' CCD sensors made by E2V Technologies (former Marconi). Each CCD is cooled by a solid-state peltier cooler to about $-70\,^{\circ}\mathrm{C}$ and the cooler in turn is water cooled. The low temperature ensures low image background noise caused by thermal photons which are detected the same way as the visible photons that make up the signal.

The CCD chip is operated in frame-transfer mode, so that the next image is being exposed while the current image is still being read out. This is accomplished by having two full image areas on the chip: only the first one (top half) is exposed while the second one (bottom half) is covered behind an aluminum foil. The image transfer from the top to the bottom half can be done in a fast burst (about 1ms) while the line-by-line readout of the image takes up to 300ms.

The electron multiplication capability allows the acquisition of a very low-intensity signal [Coates et al., 2004]. The CCD chips are back-thinned/back-illuminated, which already improves the quantum efficiency to about 90%, while commonly used font-illuminated CCD chips have quantum efficiencies below 50%.

OMX operates the Andor CCDs in several possible modes:

- Electron multiplication (EM) mode at 10 MHz pixel rate; 14bit read-out.
- EM at 5 MHz pixel rate; 14 bit read-out
- EM at 1MHz pixel rate; 16 bit read-out
- non EM (conventional) 1 MHz pixel rate; 16 bit read-out

Each of the above modes can be operated in full image mode – 512x512 pixels – or in sub image mode with half size at 512x256 and quarter size at 512x128 pixels.

In EM mode the EM gain level can be chosen according to sample and imaging conditions. The slower speeds can be chosen to take advantage of lower electronic readout noise at lower amplifier speeds. The lowest readout noise is attained by choosing the 1MHz conventional mode. In this mode a full 512x512 image can be collected every 300 ms at noise levels of about 5 electrons.

One problem we encountered while using the Andor CCD cameras, was "baseline drift": Each pixel of the image digitizes the number of incoming photons that are converted into electrons into one positive integer value. In 14bit mode the mathematical maximum value is 16383, in 16bit mode it is 65535. In complete darkness the resulting value is still some positive number with a value determined by the amplification electronics. It is strongly temperature dependent and its specific way of *how* it changes with temperature cannot be predicted since the electronics is comprised of many different modules, each responding in a different way. Therefore the design of the chip together with its peltier cooler is crucial to ensure temperature stability. However, we reproducibly measured a drift of many tens of counts for any sequence of images acquired at rates of 1Hz, or slower or faster. Luckily there is a solution. With the helpful instructions from Andor we could re-program the CCD electronics to readout 528 by 526 pixels with each acquisition. The extra pixels are bordering the image area and are covered behind an aluminum foil. That is, they are always reading dark values that can be used to normalize the data images to a steady baseline. Since all resulting pixel values have to be positive, and actual pixel values may be lower than the average dark value calculated from the border, I chose 1000 to be the reference “mean dark” baseline value.

4.8 Sample stage

The sample is mounted on a standard 3 by 1 inch glass slide and held in place over the objective by the slide mount. The slide mount was designed in AutoCAD and is made out of ceramic (Zerodur) to minimize temperature drift. It is attached to a high precision, interferometric-grade XYZ-stage made by Newport. Three fast micro-stepper motors, called Nanomovers, made by API, can navigate 21 mm in each direction. They can move the stage at speeds of up to 2.5 mm/second with a precision of 100 nm. But stepper motors are not fast for short range motion, especially when the moving direction is changed repeatedly. For this, OMX uses three piezo actuators made by piezosystem jena. Their travel range is limited to 35 μm in closed loop operation. The vertical piezo is used for fast and precise focus changes while the X and Y piezos are only used for certain experimental imaging applications (‘stereo imaging’, see below: 2.5D). The piezos can move back and forth (i.e. go through focus) as fast as 30 times a second (15 ups and 15 downs). This speed is obtained in closed-loop (drift controlled) mode – in open-loop mode it could be done faster.

The LMX microscope, which will be described in 4.10, uses an XY version of the same stage and uses the same Nanomover micro-steppers for the computer controlled motion.

4.9 Computer infrastructure

To provide flexibility and reliability the OMX system is run by 8 PCs. A schematic layout diagram is shown in figure 4.8. It shows the multiple interconnection lines between the computers and other hardware components. Different types of connections are indicated: Gigabit Ethernet for

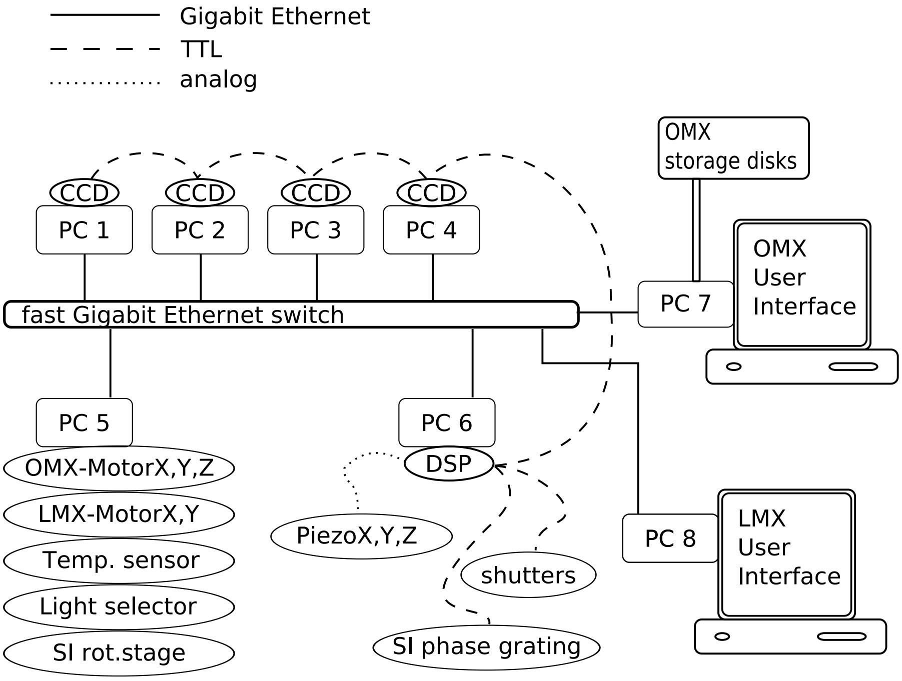

Figure 4.8: The OMX microscope system is using multiple computers to provide reliability and flexibility. The 8 PCs and the devices they control are indicated along with the types of their connecting lines. For detail refer to text.

the TCP/IP communication between computers, TTL digital trigger lines for real-time hardware synchronization and analog low noise connection cables to drive the piezo actuators. To ensure reliable operation of the CCD cameras at frame rates up to 100 frames per second, each camera is controlled by a dedicated PC. Another PC controls the stage motors as well as other miscellaneous controllers for temperature monitoring and illumination source selection. All hardware events are synchronized by a dedicated digital signal processor (DSP) controller housed in a separate PC.

All the PCs are connected to a fast Gigabit backbone across which they are connected to the central dual-processor graphics workstation. This is where the biologist's user interface provides access to all components of OMX. The logical topology of how the computers interact is more like a "star formation" (figure 4.9). This ensures the highest degree of flexibility and allows the future addition of new components without increasing the overall complexity of the system.

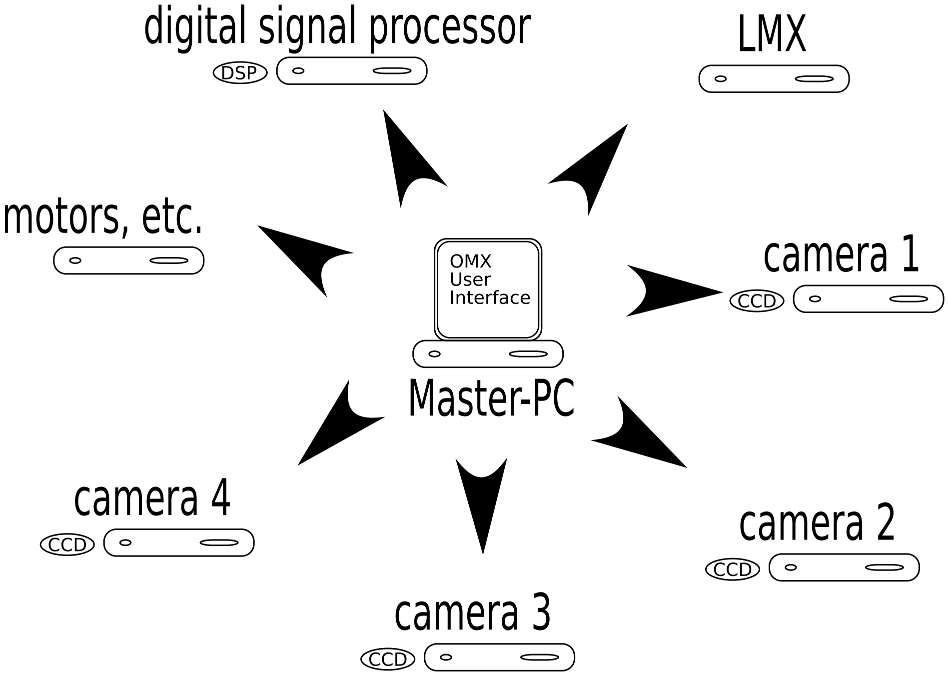

Figure 4.9: The OMX microscope system uses multiple computers to provide reliability and flexibility. Software control between the many different programs running on the different computers is done via `Pyro`: a modern Python module which transparently handles all networking tasks, so that the main code (running on the Master-PC) sees all components as if they were local.

The OMX software is written in a mixture of C++ and Python. C/C++ is required to access most of the hardware driver codes which also requires running on the Microsoft Windows operating system. They are provided with the respective hardware device by the vendor as linkable libraries (DLLs). Automatically generated wrapper code allows accessing all functionality from a more convenient and more maintainable Python script. Only *speed critical* code is written in C++. All other codes, including graphical user interface code and all networking codes are written in Python.

The Python Remote Object library (Pyro) is used to interconnect the multiple applications on the different PCs with minimal overhead.

The graphical user interface is implemented with the platform independent wxWidgets and OpenGL software libraries, so that both Linux and MS-Windows can be used to operate the microscope. The Python interactive scripting environment allows both flexible system development and efficient real time data analysis.

4.9.1 Camera PCs

Each CCD camera is controlled by its dedicated PC. The PCs are rack-mounted 1U (2.5 inches high) fast (3GHz) single processor Pentium-4 servers. The speed is necessary to be able to flat-field (see chapter 7) images in real time. At the same time they correct for the floating baseline problems (see section 4.7) observed with Andor CCD cameras.

4.9.2 Motor PC

The "motor PC" houses the PC-board (ISA card) which talks to the API Nanomover controller box. In addition, a couple of miscellaneous controller cards are placed here. Together they are:

- Nanomover controller card (for OMX xyz-stage *and* LMX xy-stage)
- temperature sensor and I/O controller card (National Instruments, NI435x). Digital I/O is for control of the SI/conventional illumination flippers. It also provides one bit for a cabin-light-sensor.
- SI grating rotational stage controller card (National Aperture)
- Z-tower TSV / UniDrive6000 controller card (Newport)
- A spectrometer – this was only used as part of the development process of OMX

4.9.3 The digital signal processor (DSP)

For high speed data acquisition it is important that all hardware events are reliably synchronized. This can not be accomplished by a common PC that is operated by a conventional operating system. Even though PCs often react very quickly to a given event, such as an Internet data packet arriving on the network interface card, they might also get interrupted by other competing events resulting in delays. At best a PC can only guarantee an *average* response time – which is known as "soft real-time". However, microscope data acquisition requires a guaranteed *worst-case* response time – this is called "hard real-time". This is only provided by a dedicated computer processor that is not running a (conventional) operating system.

In addition to hard real-time with a timing of 1 μs accuracy, the DSP used for OMX features 32 digital output lines, 4 analog output and 4 analog input converters. The digital ports are used to control shutters, camera triggers and the digitally controlled SI phase grating. Three analog outputs control the piezo actuators. The analog input is for piezo position read-back. The analog A/D and D/A converters have a 16 bit dynamic range.

The DSP is programmed in standard C. The application loaded implements a "state machine" which iterates over a table that defines for every time point of the experiment all analog voltages for the piezo control and all digital output values for camera and shutter trigger lines, and for the SI phase grating phase position.

4.9.4 DSP host-PC

For more flexibility and because the motor PC could host only a limited number of hardware extension cards, the DSP board is placed in a separate PC. Since the DSP is an autonomous computer, the PC is mostly just providing electricity and is otherwise idle. The exception is when the OMX user sends new instructions for a new experiment, which are received via the PC's Ethernet connection.

4.9.5 Main user interface: three panel control screen

While the OMX software suite is a composition of multiple applications running on multiple computers with (possibly) different operating systems, all necessary instrument controls are accessible from a single central graphical user interface (GUI). The GUI program runs on a fast dual-processor graphics workstation – it can run on either Microsoft Windows (XP) or GNU/Linux. Special emphasis was put on not overwhelming the user with

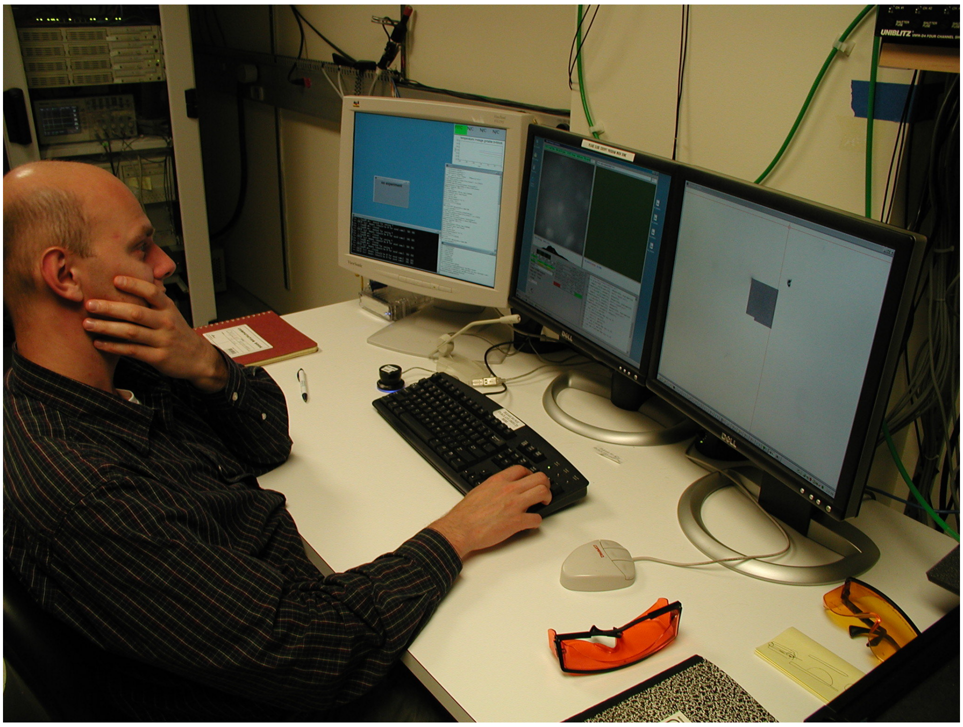

Figure 4.10: The OMX graphical user interface is spread across three LCD panels. It shows up to four wavelength images in real-time feedback. All components of the microscope system are monitored and controlled from here. The photograph shows Yuri running OMX with two wavelength channels (top half in center panel) and a MOSAIC navigation window filling the right panel. The left panel shows miscellaneous message windows.

too much information and too many controls.

A single main graphical user interface (GUI) is displayed across three flat-panel displays (figure 4.10). From here all experiment parameters are controllable and real-time video images from all cameras are displayed. The top two thirds of the right two panels show up to four real time wavelength images side by side. Each image is shown with its intensity histogram profile right underneath it. The histogram control can also be used to interactively change brightness and contrast of how the images are being displayed – this is done by adjusting the minimum and maximum value by sliding a “red bracket” using the mouse. Image histograms and intensity scaling are updated in real time during data acquisition. The third panel on the left shows a multi resolution mosaic map (see section 5.1) and status indicators for excitation sources, cabin light, camera modes, temperature measurements and an overall status message log. Temperature is measured at several different points in the OMX cabin. The temperatures are displayed as a function of time in a graph showing the trend over the past three hours.

Simple menu and button controls allow setting exposure times, selecting camera modes and excitation light sources. More detailed menus and dialogs are provided for various experiment settings. Additionally a real time interactive Python scripting console allows access to all components of the OMX system for the most advanced instrument control. New scripts for task automation can be easily written and dynamically assigned to a graphical button. A library of many experimental procedure scripts is accessible and ready to be used.

4.10 LMX: navigation station

One of the main design criteria of the OMX microscope is its mechanical stability. It is known that high resolution optical microscopes are very sensitive to even the smallest vibrations. This is why the OMX microscope body resides on an optical table with active low frequency vibration compensation. To further improve mechanical stability of the optical imaging components OMX does not have an objective turret: it has only one objective at a time; usually a high NA 60x or 100x oil or a 60x water objective.

The high resolution imaging of OMX is obviously associated with a small field of view. For rapid screening and sample slide mapping the OMX system therefore includes a second low magnification, wide view dissection microscope called LMX (low magnification microscope of OMX). It provides three air objectives: 1.3x, 10x/.45NA and 20x/.42NA with additional 0.6x–6.0x 10 step zoom and it has transmitted bright field and dark field modes, and a Hg-Arc lamp for fluorescent imaging modes. The microscope is the commercially available M^2Bid Quad Stereo dissection microscope from Kramer Scientific, which is built around the Zeiss Stems SV 11 APO microscope. We customized it by adding a computer controlled motorized stage and added a scientific grade (10 bit gray scale, 1024x1024 pixels, up to 10 frames per second, not cooled) CCD camera made by Ikegami. Figure 4.11 shows the setup at UCSF.

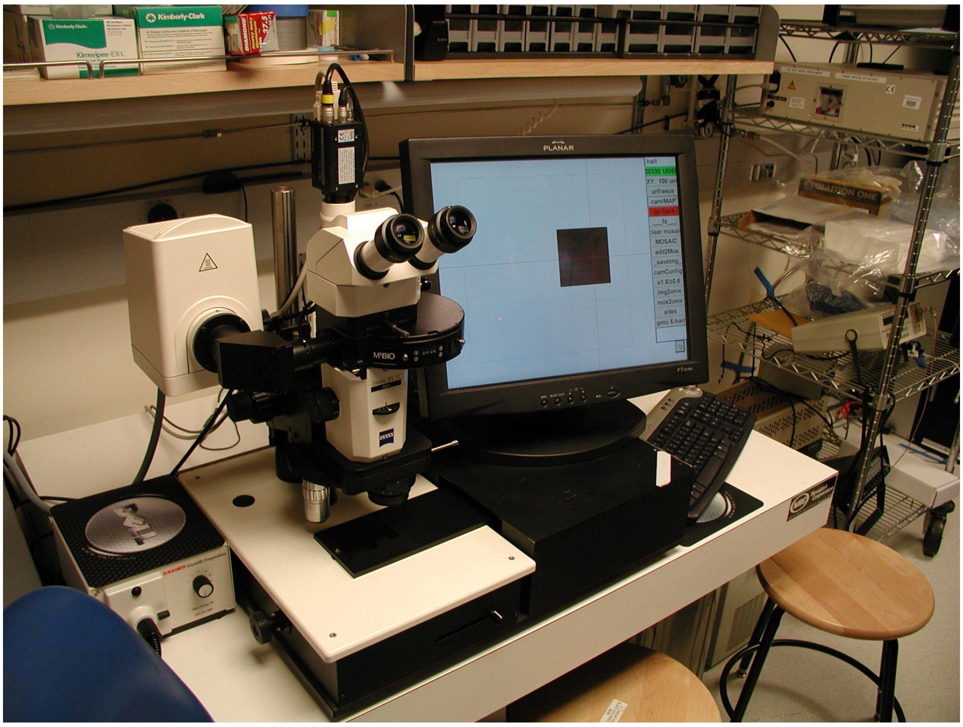

Figure 4.11: To complement the high resolution of OMX, the LMX microscope provides a larger field of view with low magnification air objectives. The stage is motorized and can be operated via a touch-screen. The image can be seen digitally on the screen or with stereo eye pieces.

Stereo eye pieces allow conventional inspection of the sample. Alternatively a real time video image is displayed on a 19 inch touch screen right next to microscope. Images are acquired using a light sensitive scientific grade gray scale CCD camera. The stage is motorized and computer controlled. The LMX stage positions are calibrated to match the OMX stage coordinates. This way images and/or marked positions can be transfered to OMX; then positions of interest can be directly targeted once the sample slide is put onto the OMX microscope stage.

Chapter 5

Operation of the microscope

The OMX system is comprised of two microscopes: The actual OMX high resolution 3D deconvolution microscope and a low magnification dissecting microscope (LMX). The OMX design allows only for a single high magnification objective. This can be changed manually, but there is no turret. Hence, the second microscope is needed to assist in sample finding. This two microscope set-up has proven to be a great advantage compared to conventional multi-objective microscopes.

At UCSF both LMX and OMX reside in the same room (see section 4.2) which allows quick sample transfer. For extended uniform samples like a lawn of cells the slide is generally put directly on the high magnification microscope, but for sparser samples, like fly embryos, dissected tissues or when there are only few single cells across the whole cover slip, pre-scanning with LMX make operations more efficient.

5.1 Pre-scanning of sample slide

The low magnification dissection microscope can be used to do preliminary sample screenings and to assist in finding objects of interest once the slide is put on OMX. It allows the compilation of "navigation maps" so that later sample finding on the OMX microscope is a matter of a single mouse click in order to arrive at the correct X-Y-coordinates.

When the sample, mounted on a standard coverslipped glass slide, is put under the LMX microscope it can be viewed through the stereo eye pieces choosing between three (1.6x, 10x/.45NA and 20x.42NA) air objectives while also using a 10 step .6x to 6x zoom. The object can be illuminated with transmitted light in bright-field or dark-field mode. Alternatively the Hg-Arc lamp can be used to look at fluorescent markers. The focus is adjusted manually, the sample stage moves laterally using computer-controlled motors. This can be done either by pressing left, right, up and down keys on a key pad (remote control) or by tapping on the touch screen right next to the scope.

The touch screen is the most functional interface for LMX. Instead of looking through the eye pieces, the light can be diverted into a video CCD camera. Then the touch screen display shows a real-time video image of the sample. One can digitally zoom in and out, or tap on the image to move the sample stage to the pointed position. Individual images can be placed together to build up a "mosaic" of parts or the entire sample slide. Using the 1.3x objective with 0.6x zoom, the entire coverslip can be imaged into 16 "mosaic tiles"; this can be done in a fully automated way. If needed it is possible to image more than one area at more then one magnification. All images can be stuck together to create a multi-resolution map. But most of the time a single or few images taken at the right magnification contain sufficient information to allow easy sample finding on OMX.

In addition to sticking images together, any number of *points of interest* can be marked by simply tapping on the touch screen. These numbered points can be categorized by multiple colors – meaning "good", "bad" or "to be determined" – for future reference on OMX. Figure 5.1 shows an example MOSAIC map of a slide with multiple *Drosophila* embryos.

5.2 High resolution microscopy

The high resolution imaging of OMX is obviously associated with a small field of view. To facilitate rapid and convenient sample finding a multi resolution mosaic is drawn on the screen. If the map is loaded from LMX a residual "misalignment offset" has to be manually corrected. In general the offset is less than 100μm. The OMX microscope can be controlled in a

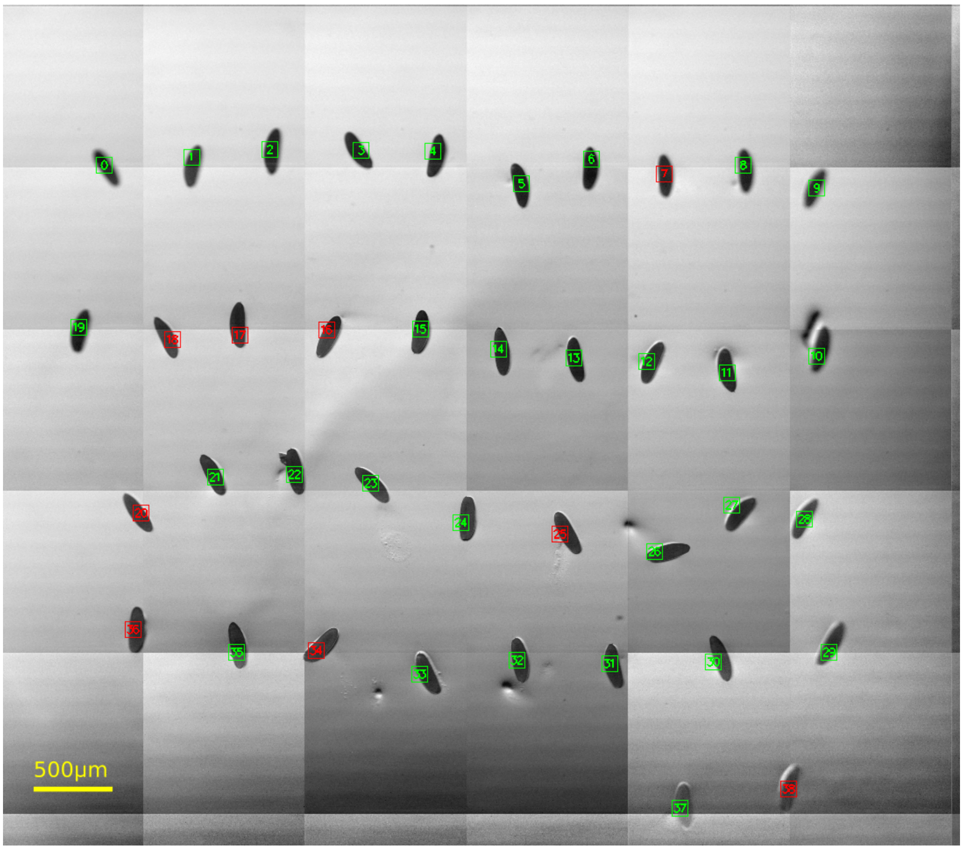

Figure 5.1: A MOSAIC navigation map acquired on LMX. The slide has multiple *Drosophila* embryos for study with high resolution on OMX. Green and red markers number the sites of interest before the slide is taken from LMX onto the OMX microscope. (Thanks to Heather McCune for providing the sample.)

variety of different ways:

- a computerized dial can be used for focusing
- the keyboard can be used for stepping across the field and changing the focus – the step size can be adjusted
- targeted moves across the slide are done via mouse-click into the map view window or into the live camera image
- camera and exposure settings as well as the selection of excitation source are changeable via one mouse click
- top and bottom focus positions can be saved and used later when running the data collection
- several experiment macros are selectable from a graphical menu – some have extra parameter fields
- all settings and macros are accessible via an interactive prompt – this also provides full featured image analysis and data handling capabilities (e.g. line-profile plots and Fourier transforms)
- new macros can be written using a standard Python programming language
- advanced macros, e.g. for auto-focusing or for fully automatic acquisition of many PSFs of many beads, are provided

The OMX sample stage is stable and reproducible enough, so that the *absolute* focus (Z motor) position is unchanged to within less than 10 μm between different sample slides and on different days. It might be different for different kinds of slides (e.g. metal vs. glass slides) but for each case it is so reproducible that the sample can generally be brought immediately into focus ("blind focusing"). This is very helpful in experiments were live objects are to be imaged immediately after dissecting on LMX.

Sample finding is then done with the help of the above described "navigation map" from LMX. New images acquired on OMX at full resolution can be added into the map – making a truly multi-resolution map – allowing continuous digital zooming in and out from the overview of the full slide down to the details of the sub cellular regime. Positions can be marked and numbered with different colors and are added into the map.

Navigation is done by mouse clicking into the map viewer or by successive stepping controlled with the number-pad on the keyboard. Focus is adjusted by turning a special computerized focus dial that is linked to the fine-motion piezo actuator.

The current system can scan 3D specimens in different ways. Once the object of interest is found and in focus, there are the following "standard data acquisition modes" to choose from:

5.2.1 3D stacks of one or more fluorophores

To acquire high resolution 3D images the sample volume has to be imaged with 2D sections about 0.2 μm – 0.4 μm apart. That is, an object 3 μm thick requires about 10 sections. Since the Andor CCD cameras (10MHz pixel rate in EM mode) can acquire 30 full size (512x512) frames per second (fps) OMX can acquire 3 3D volumes per second. For images a quarter of that size (512x128) the speed quadruples to above 10 3D volumes a second. The OMX optical design allows this to be done for up to four fluorophores simultaneously without compromising for speed.

In the case of a single focal section the maximum speed possible for quarter sized images is above 100 Hz.

5.2.2 3D projections of one or more fluorophores

In this mode the stage is performing a "Z-sweep" during each exposure. This results in an on-chip integration of the different focus section and is used for fast imaging of extended objects. For example, a chromosome will likely not lie in a single focal plane and this mode allows imaging it over time without missing parts above or below a given Z section. The stage should allow up to 30 projections per second (15 ups and 15 downs). The Andor CCD cameras (10MHz pixel-rate) can also image 30 512x512 images a second – the 5MHz camera (this model is currently used for the CY5 channel) can acquire images of half that size (512x256) at 30Hz.

5.2.3 Structured Illumination (SI)

The SI mode is used in the same way as the 3D-stacks – only the 'SI' field in the experiment interface dialog has to be checked. This automatically switches the experiment script to acquire 5 phase-shift images per optical section, and repeats the 3D stack for a total of 3 grating angles. The light source 'SI'-selector flips all flip-mirrors as needed so that the SI-illumination light path and the right optical fiber is used. For SI imaging the optical sections should not be more than .125 μm apart. Since OMX features SI imaging for 60x Water and for 100x Oil objective and for illumination wavelengths of 405,488 and 532 nm the proper SI *zoom plate* has to be chosen. By experience we found that the 532 nm-Oil plate tends to give good results for all three wavelengths. Currently stage drift is still a remaining concern – drift has to stay below 1 pixel for periods up to 30 minutes. Waiting for about 4 minutes right before starting the data acquisition seems to alleviate most of the problem.

5.2.4 '2 $^1/_2$ D' (stereo) imaging

As a novel mode of imaging we have developed a very fast, quasi 3D stereo mode, that we call "2 $^1/_2$ D" imaging: here the 3D volume gets projected twice. The first projection (downwards) is done the same way as in the above described "3D projections" mode. The second (upwards) projection though is executed with a lateral sweep being executed in synchrony. This effectively generates a stereo pair image.

In (the default) close-loop operation of the piezo actuators this can generate up to 15 3D views per second. For structures that are not to complicated (e.g. few point markers) the full 3D information can be computationally recovered.

We are currently exploring combining this mode with special open-loop motion control which would, for the first time, allow the study of 50 3D data-points per second.

Chapter 6

OMX requires new software

The software used to control the previous microscopes built in the Sedat lab, namely the *OM1* and *OM0* microscopes, is called *Resolve3D*. It is built on IVE ([Chen et al., 1996]; also see section 6.1 below), runs on SGI Irix and on Linux, and is close to identical to the software used to control API's DeltaVision microscope, a commercialized version of *OM1*.

When we started the OMX project the new features introduced required a new kind of software design. Having no eye-piece requires fast real-time video graphics updates and a user-interface design that is more *direct* than conventional hardware control programs. New software is also required because the hardware control libraries need to run on Microsoft Windows.

The programming language I chose was C++. This is a modern, object oriented extension to the older programming language C, which is what Resolve3D and IVE are written in – parts of IVE are written in Fortran. For all graphical user interface code OMX uses *wxWidgets*: this is a flexible, Open-Source (free) and powerful library taking advantage of the object-orientedness of C++. The most striking feature of wxWidgets is that a program using it can be compiled and run (without changes) on Windows, Linux (or other Unixes) and Mac-OS. This allows flexibility for future developments where one might prefer an operating system other than Windows.

A far reaching decision was made when we needed to add scripting capabilities into OMX. Originally it was only intended to control the timely sequence of the different steps during an experiment. An experiment could for example consist of first selecting a light source and then iterating over a series of steps, each adjusting the focus position and taking an image exposure. Resolve3D uses a self-made scripting language that recognizes a fixed set of a few commands with arguments. The only supported control structures (like repeats) are loops over wavelengths and over focus steps. There are no general variables. For OMX I decided to chose a *full-featured*, existing programming language: Python.

Python was created in the early 1990s by Guido van Rossum at Stichting Mathematisch Centrum (CWI) in the Netherlands. It has found very widespread use since. It is a modern multi paradigm programming language with strong support for object oriented software design. Over time – after starting to work and getting more familiar with Python – more and more features became apparent which are now integral to any current and future software development in our group. Most of them are directly connected to specific open-source projects each in use and developed by an extended Internet community. An overview is given by the following list:

Python	[Python.org] A modern scripting language. Includes a large amount of ready-to-use packages.
SWIG	[SWIG.org] SWIG stands for Simplified Wrapper and Interface Generator. It automatically generates all necessary binding code needed to call any C/C++ function from Python. This is used extensively to access OMX's underlying C++ program from its experiment scripts. As the OMX project progressed, this was the centerpiece for converting all hardware controlling software to Python [Beazley, 1996; Beazley and Lomdahl, 1996; Beazley, 1998].

wxPython	[wxPython.org] An open source library that allows you to create, access and modify all parts of the (C++) wxWidgets components in OMX. Using this I could gradually transition most software parts from C++ to Python: mostly for convenience in the conception, testing and maintenance phase of the software development.
Pyro	[pyro.sourceforge.net] Allows calling functions across the network: Not only can functions be executed on another PC but both return values and error-handling is transparently communicated back across the network.
Numarray	[numpy.scipy.org] Numarray is part of Numerical Python at scipy.org. It adds the language support for high level mathematical operations (like fast Fourier transformation) from the Python script. In OMX this is used for both simple things, such as displaying of temperature curves, and for sophisticated auto-focus routines [Greenfield et al., 2003; Dubois et al., 1996].

6.1 Data analysis software

The Sedat and Agard labs have compiled a plethora of image analysis routines over many decades. In 1992 they put together a software package for 3D image analysis which they called IVE ("Image Visualization Environment") and Priism [Chen et al., 1992, 1996]. It is designed to be as generic and flexible as possible using the software technology available at the time. It built the foundation for all further image analysis software development in these labs. It originally ran only on SGI Irix workstations but has since been ported to Linux and Apple's OSX. API's DeltaVision and SoftWoRx are direct descendants of Priism.

Since OMX runs on MS Windows we could not use IVE, so we had to start over. Furthermore, it seemed to be a good opportunity to build on new software paradigms and benefit from the new open source movement. Python for “gluing” the parts together, Numerical Python for interactive hight-level computation and wxPython for a modern (cross platform) graphical user interface. To incorporate existing C/C++ or Fortran routines SWIG can be used to automatically generate the needed “binding” code. For lack of a better name I called this new direction Priithon.

6.2 The Priithon package

To provide a comfortable environment for developing new data analysis software I have assembled a collection of very powerful software engineering technologies. These benefit greatly from the open-source movement. Instead of continuing the current path of writing more and more “low level” routines in Fortran or C the new approach is built around the high level scripting language called Python. Python is a free programming language. It runs on any operating system and comes with a very extensive library of “ready to use” modules assisting in many different kinds of tasks [van Rossum, 1995].

The new package is called Priithon[1]. Its focus is on multi-dimensional image analysis and visualization. It has been used in several research collaborations I have participated in: a new myopic deconvolution algorithm [Hom, 2006; Hom et al., 2007], a wavelet based filtering algorithm [Moss et al., 2005], an electron microscope CTF estimation algorithm [Shah et al., 2006a] and an electron microscope deconvolution algorithm [Shah et al., 2006b]. It is also extensively used in all of the OMX applications and played an enabling role in the development of the overall OMX system. By popular demand I provide a precompiled installation package for Linux, Windows and Mac OS-X.

Priithon provides tools for a number of different tasks:

- learning the environment is supported by an especially helpful interactive programming shell
- multi dimensional image data analysis

---

[1] The term Priithon refers interchangeably to a) the entire collection of (precompiled) packages, b) the interactive shell and c) the specific Python package of code that I wrote, which is accessed by `from Priithon.all import *`

- algorithm development – specifically for multi-dimensional image analysis
- access to fast C/C++/Fortran code
- adding a graphical user interface to make programs more usable
- hardware control
- easy and transparent network communication

Image data is efficiently represented as a multi-dimensional array. With respect to optical microscopy data, a single sample section would be two dimensional data, a stack of 2D images is 3D. A time series of these images would be 4D and if this was done for more then one wavelength, the overall data would be 5D. 2D could also be a sample projection. 3D and 4D data could also represent a different subset of the 5D case: E.g. 3D could be a given optical section in more than one color. The Python support for multi-dimensional (nd) arrays is developed by the Numerical Python community. Priithon uses an implementation done at the Space Telescope Science Institute called "numarray". They chose Python for the analysis of large image data sets acquired by the Hubble Space Telescope. ND arrays are supported for all data types: we are especially interested in "unsigned short (16 bit) integer", which is the native data type of images acquired by OMX, and "single precision floating point" which we prefer over "double precision" since it requires only half the memory space.

All basic mathematical operations are supported for arrays and can be used like scalars. For example: Subtracting a 'camera background image' b from an acquired sample image a can easily be written as $c = a - b$; c then gives the original image without background. For higher order operations like Fourier transform or noise filtering Numerical Python provides ready to use functions. I have added some additional functions that are missing, such as access to the fast Fourier transform library (FFTW) for single precision data arrays.

The main user interface to Priithon is its interactive shell window. Image data can be loaded and viewed using either menu commands or by just dragging the file into the shell window. Programming commands can be entered and are directly executed. Priithon shows some helpful information text regarding a given function while that function is being typed in. I have sorted commonly used functions into a few modules which are accessible via their few letter shortcuts. The modules are: `U`, `F`, `Y`, `Mrc` and `na`. `U` contains a collection of some *useful* shortcuts, `Mrc` facilitates reading and writing of Mrc/Priism files. `na` is a shorter name for the array module `numarray`. `F` provides shortcuts to the Fourier transform routines and also many base arrays useful in image analysis: examples include arrays filled with a circle, a sphere, a ring, a Gaussian bell shape or a *Mexican hat* shape. The `Y` module gives access to all functions requiring a graphical display, i.e. they are not accessible when a script is executed as a batch process. The helpful Priithon shell lists all available functions as the module name is typed.

Integration of fast optimized C/C++/Fortran code is one of the main focuses in Priithon. This is accomplished with the help of another freely available Open Source tool, called SWIG (Simplified Wrapper and Interface Generator). This tool can automatically generate needed wrapping code to access a native linkable programming library from a number of different scripting languages. Specifically for Python a large collection of input and output variable types, all kinds of global variables and, most importantly, Python error handling mechanisms are supported. SWIG can be extended by providing further so called “typemaps” to support custom data types. I have provided a collection of typemaps to transparently work with 1D, 2D and 3D image arrays of any pixel data type. Since the data access is done without copying the data memory, native functions are executed with mostly negligible overhead at essentially 100% of their original speed.

SWIG proved especially helpful for controlling hardware. Any hardware device is usually supplied together with a C library and a user manual. In some cases this also includes example code. The latter tends to be especially helpful since it allows starting from a self-contained and working code base. However, using SWIG adds a new and much more direct way to explore and test the library-hardware-interaction. Commands can be executed from the interactive Priithon shell. The direct feedback of every command facilitates much quicker development and lowers the initial learning threshold noticeably.

As the OMX hardware is distributed across many computers on a local Ethernet network, another open source Python project has proven to be invaluable: Pyro (Python Remote Objects). Pyro provides an infrastructure that allows functions called on one computer to be executed on a different computer. It forwards both return values and error indicating exceptions back to the calling program. This technology greatly simplifies and streamlines the overall code. Any need for parsing and unparsing of network messages is now hidden. What might be more important is that remotely executed commands can now seamlessly wait and check for successful execution. Before, when I tried to implement error handling without Pyro, it was a very complex and time consuming task.

For the graphical user interface (GUI) I am using another open source project called wxPython. While standard Python comes with support for Tcl/Tk based GUI, I chose wxPython because it is much more feature rich and faster. The code is entirely cross platform, which means that, for example, a program written on Windows, runs the same on Linux or Macintosh.

Drawing of large 2D images with arbitrary amounts of additional line and vector graphics can these days all be done directly on the video card. The computer gaming industry is driving the graphics hardware market to make increasingly cheaper and more powerful devices. A programming library is available to address this hardware in a way independent of the operating system used, it is called OpenGL. There is also an efficient wrapper module for Python. This is what I use in Priithon to draw images and line graphics. It is compatible with wxPython and allows you to zoom in/out and pan at video (real time) speed.

Part III

Results

Chapter 7

Flat-field correction

The first step in image processing of digitally acquired images is called *flat fielding* [Howell, 2000]. When photons are being converted into electrons after hitting the silicon on the charged-coupled device (CCD) camera, the image is built up from the response of each sub-area (pixel). While CCDs are known for their superb quantum efficiency and linearity there is always a certain degree of variance across the different pixels – for example some pixels are physically larger, collect more photons and consequently generate systematically higher counts than other pixels. By measuring the dark value and the light response for each pixel across the field of view each image can be computationally normalized. At the same time this also accounts for other effects such as non uniform field illumination and dust particles.

Figure 7.1 shows the pattern visible in an image acquired with the Andor EMCCD camera in EM mode in *complete darkness*. The image shown is the average of 500 individual exposures. The pattern seen is probably caused by various electronic timing clocks on the CCD chip and/or the CCD read-out electronics. The intensity variation across the field is .3 counts standard deviation and 1.5 counts peak-to-peak.

Figure 7.2 shows the *flat field* image. The flat field does not change noticeably between different camera modes. Most striking are the dust spots and the relatively strong variations across the field. See discussion in section 18.7.

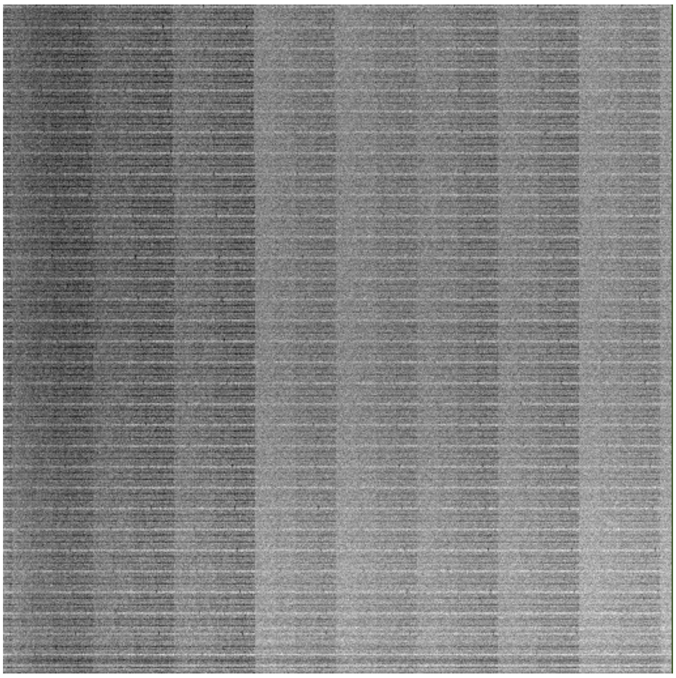

Figure 7.1: The dark field image measures the CCD response on complete darkness. Visible patterns are caused by various non-random (clock-)noise sources in the amplifier electronics. The image shown is the average of 500 dark-exposures for a representative dataset for the Andor iXon CCD camera in EM mode. The standard deviation across the field is .3 digital counts. Peak-to-peak variation is 1.5 counts.

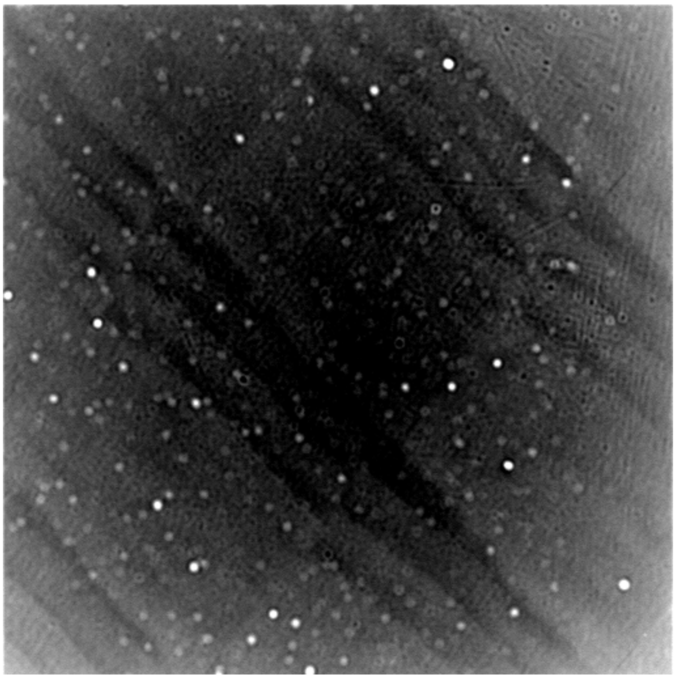

Figure 7.2: The flat field image measures the CCD response when illuminated with an even sample. The shown image is the inverse slope measured from a pixel-wise straight-line fit when exposing an evenly fluorescent plastic slide with varying exposure times. A pixel that appears bright in this image requires digital amplification, i.e. it receives less than average light. The image is representative for all the Andor iXon CCD camera modes. Many dust spots are visible. In this example the corners receive about 5% less light than average. The strongest dust spot (at the top right) requires amplification to 150% of the measured level. The standard deviation across the field is 3%.

Chapter 8

Acquisition and conditioning of a PSF

As discussed in section 3.2 wide field imaging always produces out-of-focus blur and instead of just removing it, a better treatment reassigns the out-of-focus blur back to the in-focus plane of the fluorescent object. This is done by *image deconvolution* [Agard, 1984; Swedlow et al., 1997; Wallace et al., 2001]. Image deconvolution is an iterative algorithm approximating the inversion of the imaging equation of the optical system. The quality of the resulting object estimate depends strongly on the quality of the point spread function (PSF) used. While a default theoretical PSF is often used, better results can be achieved by using a measured one. In that case the prime sources for errors are mismatching imaging conditions and noise introduced by the PSF data set. The imaging conditions can change throughout the sample, when, for example, depth effects create spherical aberrations when focusing deeper into the sample. This should be addressed by depth-dependent-deconvolution [Kam et al., 2001; Hanser et al., 2004].

To reduce PSF noise, PSFs are often radially averaged. However, to potentially correct for higher order aberrations we need to resort to a more sophisticated approach. The obvious one is to acquire as many independent PSFs as possible and average over the whole ensemble. This is done in a multi step procedure:

1. automatically acquire 100 PSFs for well separated fluorescent beads

mounted on a slide under conditions similar to condition used for biological samples

2. select for “well behaved” PSFs by eliminating higher-than-normal intensities. High intensities could indicate that two beads are stuck together, which would constitute a non-ideal point source.
3. normalize PSFs and subtract background
4. find center of each PSF
5. align all PSFs to a common center and average

This procedure has been implemented as a fully automated routine. A resulting high quality PSF that was obtained by this routine using a 100x oil objective is shown in figure 8.1. More than 16 airy rings can be seen at 9 μm out-of-focus. Additionally, many distinct non-radially symmetric features are visible. Experiments have shown that some of these rotate when the objective is rotated, while others maintain their position. Figure 8.2 shows only the non-radially symmetric components of the PSF. It is clear that many features are missed if a radially averaged PSF is used for deconvolution.

To test the effect of the improved PSF on the deconvolution performance we deconvolved a high-quality data set with a high signal-to-noise ratio. A comparison of two runs of deconvolution – one using the here shown PSF, one using a standard, radially averaged, PSF – shows that the deconvolution metric value (the R-value) is significantly better when using the full one: $R = 8\%$ vs. $R = 10\%$. A test on live sample data sets did not show such an improvement. See discussion in section 18.3.

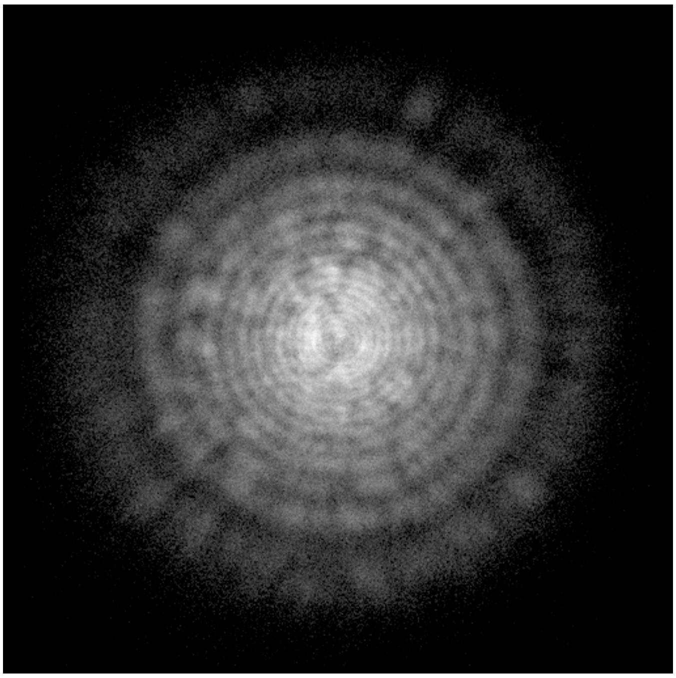

(a) optical section 9 μm out-of-focus

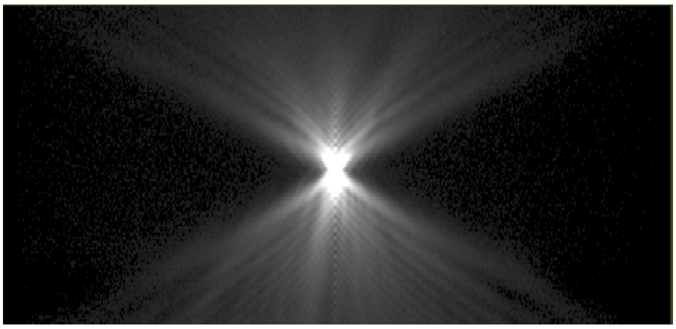

(b) x-z section through center of PSF

Figure 8.1: A high quality image of a PSF is computed as the average of 64 3D images of individual fluorescent plastic beads. The beads used were sub-resolution sized at 115 nm, excited at 488 nm and imaged in the green (FITC) channel using the 100x oil objective. Shown is the optical section 9 μm out-of-focus and a x-z section through the center of the PSF. The images are 40 μm wide and the x-z section is 19 μm high.

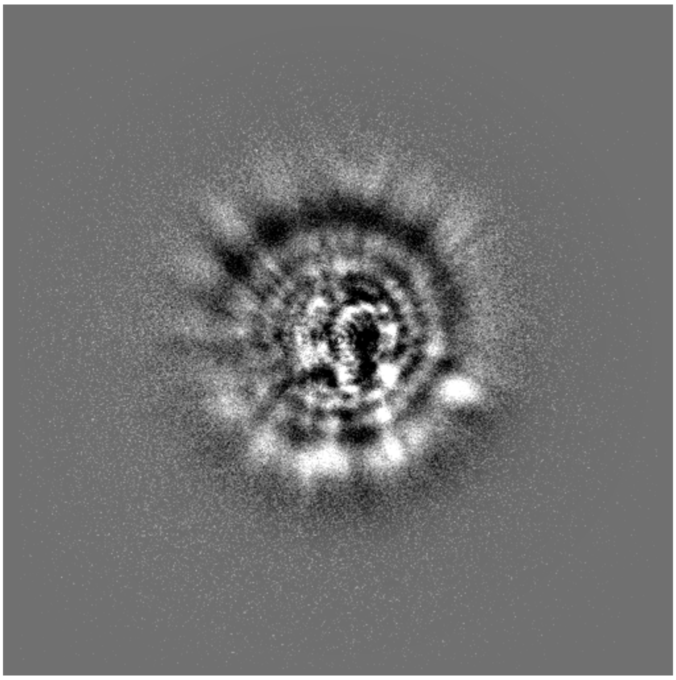

Figure 8.2: This image is obtained by subtracting the PSF shown in figure 8.1) by a radially averaged version of that PSF. This way the non radially symmetric components of the microscope's PSF become apparent. The shown section is 5 μm out-of-focus towards the cover slip.

Chapter 9

Fluorescent beads in SIM

To demonstrate the increased resolution capabilities of structured illumination microscopy test samples containing fluorescent beads were imaged.

Sample preparation: a drop of fluorescent polystyrene micro-spheres (yellow, 115 nm nominal diameter, FluoSpheres Molecular Probes, Eugene, OR) suspended in Ethanol was air-dried on a coverslip. The coverslip was then mounted in glycerol on a glass slide and sealed with nail polish. The beads were excited using the 488 nm laser and imaged in the FITC channel.

Figure 9.1 shows an in-focus section image recorded using a 100x oil objective. It is obvious how much more details can be seen in the SIM image. The apparent size (FWHM) of isolated beads is approximately 130 nm in the structured illumination image and 250 nm for the conventional image. Also shown in figure 9.1c is the deconvolved image of (a): it can be seen that deconvolution increases the contrast, but generally does not increase the (lateral) resolution as was already discussed by Wallace et al., 2001. . Deconvolution was done using a measured and radially averaged PSF.

Figure 9.2 shows the respective three images in a x-z section view. The conventional wide-field image shows, as expected, a very extensive out-of-focus blur. Just the image of a PSF itself. There is no optical sectioning as discussed in section 3.2. Iterative deconvolution increases the contrast by computationally reassigning (most of) the out-of-focus blur back into the in-focus section. That is, the axial resolution is effectively increased (see figure 9.2). It can again be seen that the lateral (horizontal in the x-z view) resolution is *not* changed by deconvolution. Structured illumination on the other hand does not produce any out-of-focus blur: there is physical optical sectioning. All three views are shown using a higher that usual contrast to emphasize the dark out-of-focus regions in (b) and (c). Hence, the increased lateral resolution in figure 9.2c might not be displayed appropriately.

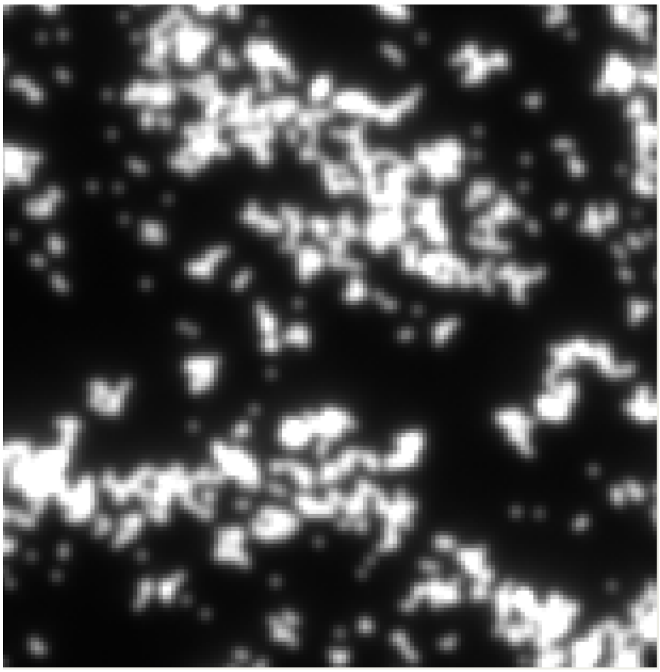

(a) conventional wide-field

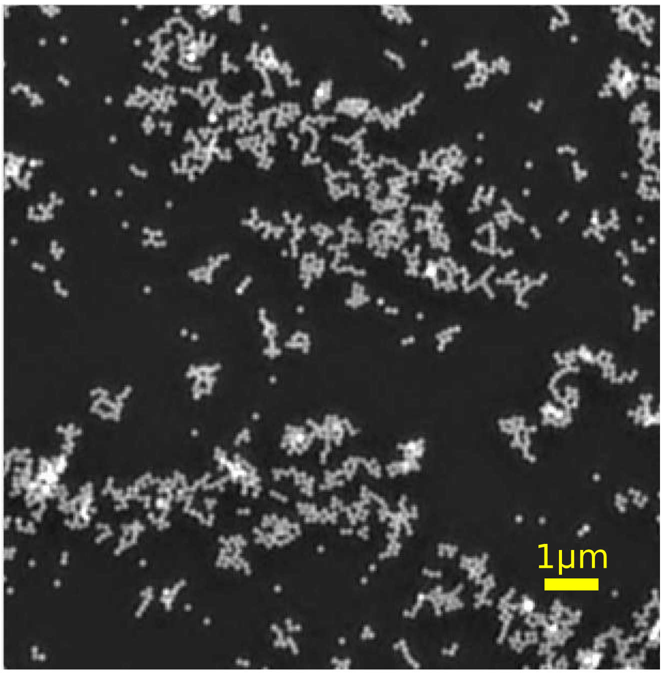

(b) Structured Illumination1

Figure 9.1: 115 nm fluorescent beads were recorded and processed by conventional microscopy and SIM using a 100x oil objective. The shown in-focus sections demonstrate the increase in resolution when using SIM.

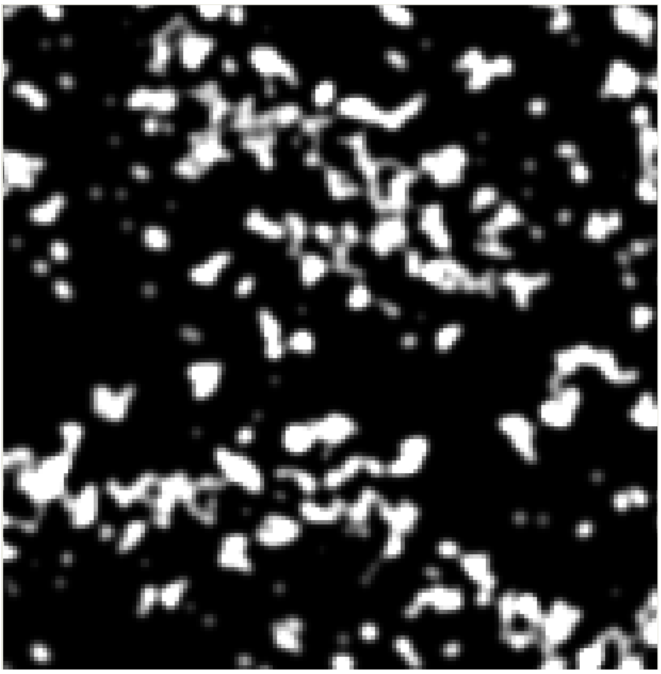

(c) deconvolved of (a)

Figure 9.1: Deconvolution does generally not increase the resolution. The same in-focus section of 115 nm beads after deconvolution shows increased contrast relative to the original data.

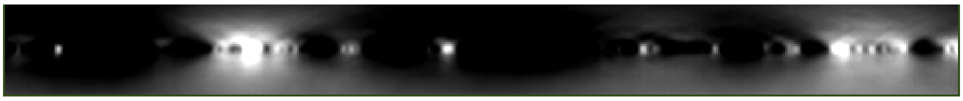

(a) conventional wide-field

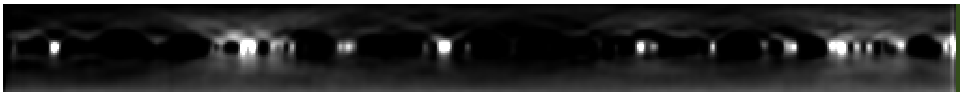

(b) deconvolved

(c) Structured Illumination

Figure 9.2: The X-Z side view shows the optical sectioning capability of SIM. The blur in conventional wide-field imaging (a) is somewhat suppressed by deconvolution (b). In SIM no such blurring occurs and resolution is increased both in lateral and in axial direction. All images are shown using increased contrast to emphasize blurring as well as “reconstruction artifacts” of SIM.

Chapter 10

Chromosome dynamics

Throughout the cell cycle the chromatin within an eukaryotic nucleus is in constant flux. It shows dynamic rearrangements on various scales [Gasser, 2002; Bubulya and Spector, 2004; Ehrenhofer-Murray, 2004; Swedlow and Platani, 2002]. Movement is often correlated with metabolic activity. To modulate access of regulatory factors to the genetic material interphase chromatin has to be dynamic. This was studied by in vivo staining of the X chromosome.

In our experiments we have imaged live *Drosophila* tissues, such as dissected nervous system from third instar larvae. X chromosomes were tagged with a GFP-MSL3 fusion protein so that in males the euchromatic arm of the X chromosome which contains $\approx$ 20 Mbp of DNA is labeled. This is only about one twentieth (1/20) of the total DNA in diploid nuclei. The fly lines were generously provided by Dr. Mitzi Kuroda. Figure 10.1 shows a representative image. The nucleus is outlined. Fast imaging was performed at various speeds and various modes. 3D stacks were acquired with a 100x oil objective at rates up to 8 stacks per second and 3D projections were acquired at slower rates of one per second.

In figure 10.1 the territorial organization of the X chromosome is clearly visible. Within this territory several globular domains stand out by MSL3 staining, with an average diameter of 200–300 nm. This is similar in size of globular domains that have been observed in other organisms [Habermann et al., 2001]. I count on average 15–25 such domains per nucleus. Sometimes

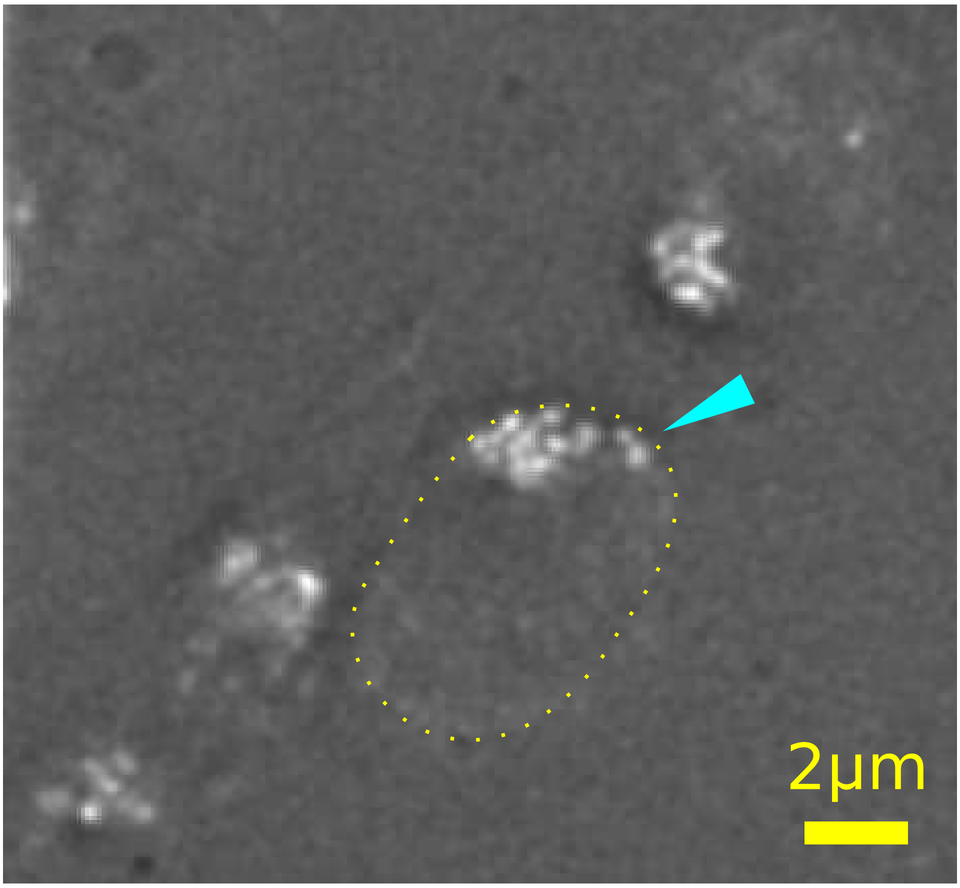

Figure 10.1: A *Drosophila* male cell in live dissected nervous system tissue in interphase with GFP-MSL3 on the X chromosome were imaged by using a 100x oil objective. A cell nucleus is outlined and the euchromatic arm is visible. We often see a protrusion extending outside of the chromosome territory as seen in the outlined nucleus (arrow). The shown image is an optical section taken out of a 4D dataset: 15 Z-sections covering 3 μm height, 20 ms exposure time, 370 ms between exposures, 10 seconds between 3D stacks.

single domains can be found to be rather distant from the remainder of the territory (arrow in figure 10.1) which may reflect a dynamic looping of particular active loci as was observed by others [Chambeyron and Bickmore, 2004]. The dynamic behavior of the X chromosome will be described in the following sections.

10.1 Dosage compensation complex

To study the chromosome dynamics I decided to label the X chromosome in vivo by a GFP-MSL3 fusion protein. MSL3 is a component of the dosage compensation complex (DCC) that is highly enriched on male X chromosomes. For organisms that employ the XX/XY sex determination system the ratio of sex chromosomes to autosomes differs in males and females. Since all autosomes are present twice in the chromosome set, the ratio in females is 1:1, but 0.5:1 in males which have only one X chromosome. This presents a problem for many genes on the X chromosome whose function is dosage dependent. There are three possible solutions for this problem: First, one could have one of the female X chromosomes inactivated. Second, one could halve the activity on both female X chromosomes, or Third, one could boost the activity of the single X chromosome in males by a factor of two. The first is employed by humans and other higher vertebrates. The second is employed by *C. elegans* and the third is employed by *Drosophila*.

In *Drosophila*, dosage compensation is regulated by a set of genes that are male specific lethals (MSLs), at least five proteins that bind abundantly to the X chromosome in the male, but not in females. These proteins are: MSL1, MSL2, MSL3, MLE and MOF (male-specific lethal-1, -2, -3, maleless, and males absent on the first, respectively). The term "male specific lethals" is derived from the fact that mutations of these genes are lethal to males, but not to females.

These proteins together with two non-coding RNAs that are transcribed from X chromosomal sites (roX1 and roX2) form a complex, the dosage compensation complex (DCC) that is specifically bound to sites on the male X chromosome (reviewed by [Straub et al., 2005; Gilfillan et al., 2006; Buscaino et al., 2006]).

MSL1 contains basic, glycine-rich and leucine zipper-like motifs. It is essential for X chromosome binding and serves as a central scaffold for the DCC assembly [Li et al., 2005]. MSL2 contains a cyteine-rich sequence known as the 'RING' finger motif, which is a Zn^{2+} binding domain found in a number of proteins thought to interact with nucleic acids [Rastelli et al., 1995]. MLE is a DExH RNA/DNA helicase. MSL3 and MOF are chromodomain proteins with RNA-binding activity [Rattner and Meller, 2004].

The hyperacetylation of the histone H4 at lysine 16 (H4K16Ac) correlates with the DCC binding to the X chromosome. This is mediated by the MYST histone acetyltransferase MOF [Akhtar and Becker, 2000; Smith et al., 2000]. Increased H4K16 acetylation might induce a chromosome-wide chromatin decondensation leading to an elevated transcription in the proper range of magnitude.

For the full function of the DCC additional factors may be required like the JIL1 tandem kinase that phosphorylates H3S10 and is enriched on the X chromosome. However, JIL1 and maybe other factors involved in dosage compensation have not been uncovered in screens for male lethality because besides dosage compensation they have additional essential functions in the chromatin based gene regulation.

MSL3 is a member of the MRG family of proteins. It is characterized by an amino-terminal chromo-barrel domain (CBD) flanked by a positively charged polar region and a carboxy-terminal MRG domain. The CBD is a protein motif structurally related to chromodomains. The MRG domain is a novel protein motif of unknown function. It is found in large chromatin remodeling complexes, all of which contain MYST family acetyltransferases.

The DCC binds to a 22 Mb euchromatic fragment of 42 Mb X chromosome. On polytene male X chromosomes the DCC is localized at approximately 300 discrete regions of the decompacted bands of the chromatin called interbands [Kotlikova et al., 2006]. Present models propose that the DCC binding is established early in the embryo and then stably transmitted to all cells throughout development.

10.2 Densely sampled 4D data

Chromatin domains show constrained motion within eukaryotic nuclei [Vazquez et al., 2001] that may be very rapid. Moreover, such domains also may dynamically change their composition by the addition and the loss of specific proteins. Such events can only be observed by fast 3D data acquisition in vivo. As a proof of principle I recorded 4D datasets from GFP-MSL3 expressing brain cells (figure 10.2).

Acquiring images using only a quarter of the CCD's sensor allows frame rates approaching 100 frames per second. The 3D stack mode described in section 5.2.1 was used exposing 8 sections per volume. The observed volume extended 3 μm in height. The fast imaging speed requires that the stage is continuing the upwards or downwards ramp motion while the images are being exposed. The average image intensity as a function of time is shown in figure 10.2. The decay in fluorescence was acceptable for up to 500 images or a total imaging time of 7.5 seconds. Since the shutter is used for each exposure, the total time where the sample was exposed – and subject to photo-bleaching – was only about 50% of the the total experiment time. Also shown in figure 10.2 are two stereo pairs taken at the indicated times. Over the course of two seconds some domains of the chromosome have moved while the overall shape of the chromosome has not changed. In the schematic next to each stereo pair a red box indicates the 2–3 domains that have moved.

10.3 High signal-to-noise in 3D projections

To obtain higher signal-to-noise ratios in the images simplifying the analysis of the dynamics, 3D-projections were acquired as a function of time using the 3D projection mode described in section 5.2.2. Figure 10.3 shows a representative field of view of multiple GFP-marked X chromosomes recorded by using a 100x oil objective. The GFP marked chromosomes show roughly 20 visually separate domains. We have acquired many time series in this manner. Again, the domains appear to be very dynamic. They appear as bright spots which are sometimes connected and sometimes not.

10.4 Semi-automatic tracking

Sometimes connections disappear and new ones are established. Spots also move, disappear and reappear. To quantify the kinematics of these spots I have implemented a tracking algorithm. Instead of attempting to get fully automated tracking the system is purposefully kept in a *semi*-automated mode. This is guided by the experience that automated tracking often pro-

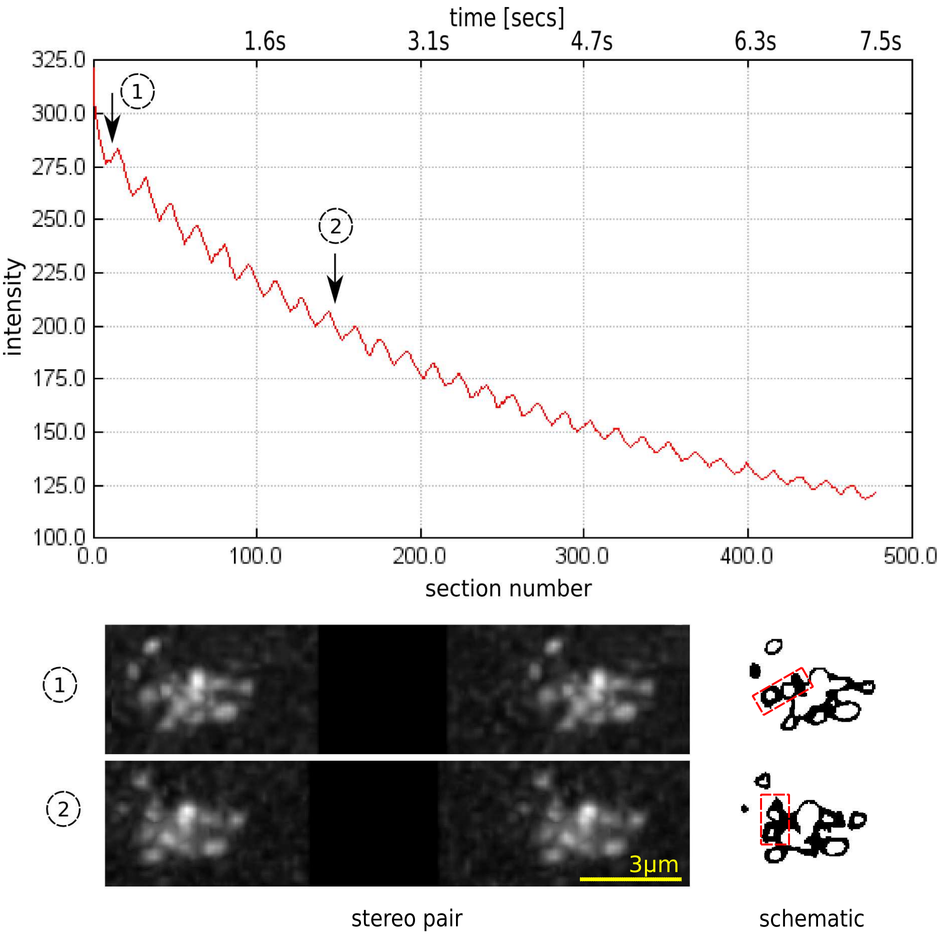

Figure 10.2: Fast chromosome dynamics is imaged at 64 exposures per second using a 100x oil objective. With 8 optical sections acquired per 3D volume you can see 8 intensity maxima (each at the center of the nucleus) as the focus plane moves up and down through the sample. The graph shows an acceptable level of bleaching for up to 500 exposures; during the total 7.5 seconds the sample is only exposed 50% of the time. Two stereo pairs taken at time point (1) and (2) demonstrate how the chromosome has changed shaped within approximately two seconds time. The schematic outlines obvious changes.

duces erroneous time-traces that require manual intervention.

There are many established automatic tracking algorithms [Cheezum et al., 2001], but we found that convolution of the raw data by a Mexican hat filter greatly improves the algorithm's robustness and overall performance.

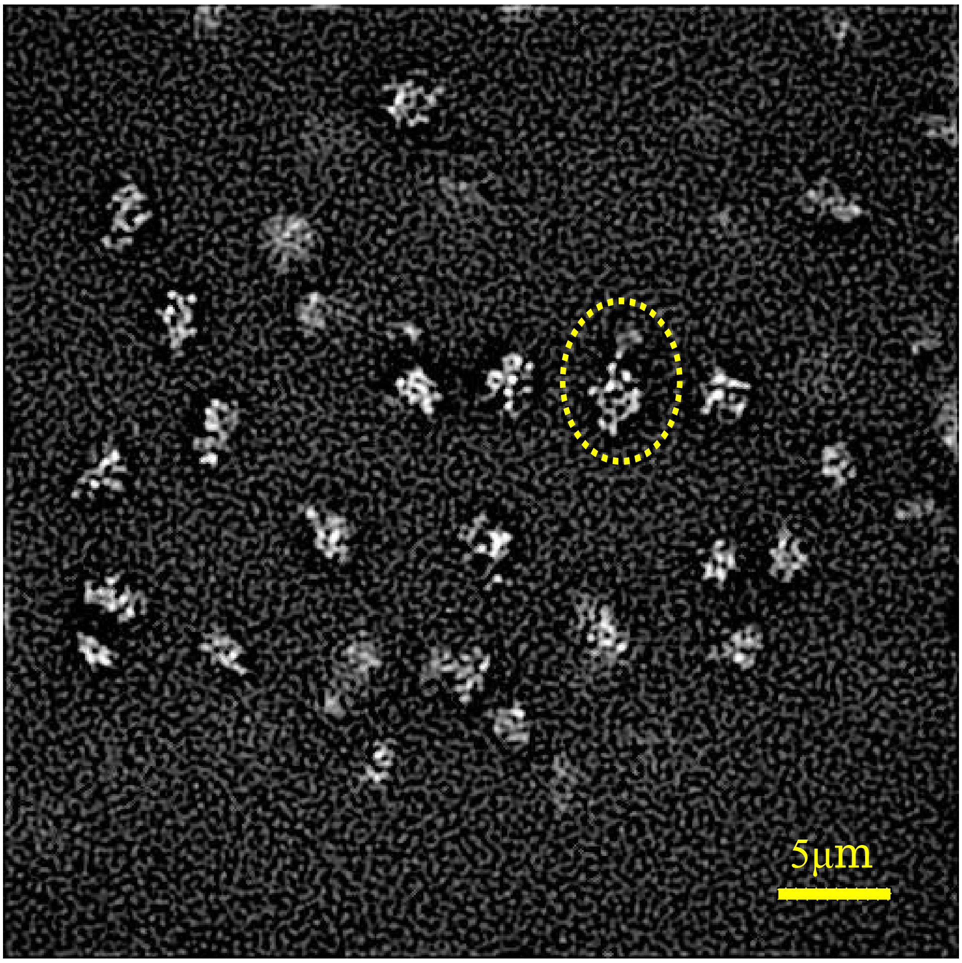

Figure 10.3: 3D projections were acquired at a rate of 1 per second using a 100x oil objective. Projections were done each during a 20 ms exposure and a 3 μm focus sweep. Multiple nuclei with GFP-marked MSL3 X chromosome are seen in the image field. The circled nucleus is was used to test various analysis algorithms in later sections of this chapter.

This turns out to be very similar to the Laplacian of a Gaussian (LoG) approach taken by [Sage et al., 2005]. Using the Priithon package described in section 6.2 I have added a real-time updating graphical user interface with sliders allowing adjustment of the Mexican-hat radius and the segmentation cut-off threshold level. The program is developed for 2D-time data. The same code also works for 3D-projection time data. Once the filtering and segmentation has converted each time point image into a small number of possible spot positions, the time points' positions are automatically selected and cross-connected along the time axis. This is done by manually picking an initial spot position in the first time image. Then this spot gets automatically connected to the nearest spot position calculated for the next time image and so on to build up a complete trace through time. A time-slider is provided to manually cut the trace, when, for example, the spot disappears, or when it merges with another trace. Any number of traces can be created and are displayed in different colors on top of an image of any, independently chosen times. Figure 10.4 shows a screen shot of 8 traces produced this way. The image data comes from the nucleus marked in figure 10.3. As can be seen in the figure the domains labeled by GFP show a rapid constrained motion. Between two time points of 1 sec there is an average 2D movement of single domains in the order of 100–200 nm with the largest distance of 500 nm traveled between two consecutive time points. In 2D spots move in an constrained area with a diameter of 300–800 nm.

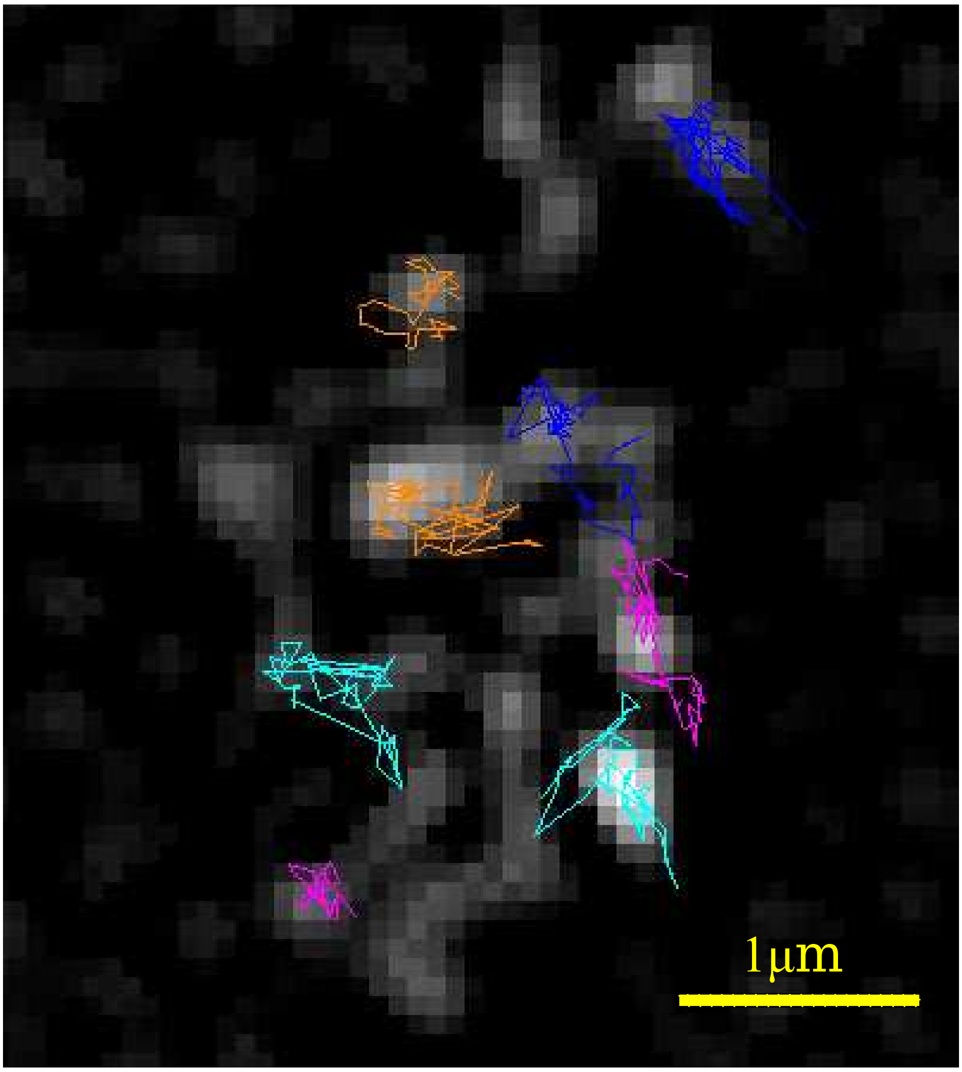

Figure 10.4: To quantify the degree of dynamics occurring at different places along the chromosome we implemented software that automatically tracks locally marked regions along time. The algorithm was tested using data of the in figure 10.3 circled nucleus. Bright spots are regions of high GFP concentration. They are followed until they disappear or until they merge with a neighboring spot. Shown are the traces of 8 representative traces, with the image taken at the start of theses traces in the background. The automated tracking of these bright spots on the chromosome indicate various different levels of dynamics. The movement of single domains is constrained to a small area. For a detailed description see text.

10.5 Visualizing 4D data

Visualizing the full extent of four dimensional data – three spacial (x, y, z) dimensions plus one time (t) dimension – in one image might be impossible for the human brain. Therefore the data at hand must be mathematically *reduced* before it can be visualized in a convenient way. One such reduction approach is provided by a kymograph (e.g. in [Sagolla et al., 2003; Mallavarapu et al., 1999; Maddox et al., 2000]). Commonly these kymographs are 2D images in x-t-space. After a z projection followed by a projection of the y-axis the remaining two dimensions are easy to display in a gray scale intensity image. To show more information the kymograph in figure 10.5 is a (3D) stereo view of a quasi-volume constructed from the '3D projection' × time product: time is displayed in the downwards direction, but the 3D projection images are preserved and displayed tilted into the 3D horizontal plane.

Shown are representative kymographs of the nucleus marked in figure 10.3 and three neighboring nuclei: two to the left and one two the right. It can be clearly seen how the spots move locally, while generally preserving their local relative topology towards each other. Furthermore, exemplified in the second nucleus from the left, it can be seen how a spot appears and later disappears again for a certain period of time.

Besides the possibility of a discontinuous saltatory movement of domains that would be too fast to be imaged even by the given method the (dis)appearance of labeled domains could reflect a dynamic GFP-MSL3 binding. The proposed reversible association and dissociation of MSL3 at particular sites would suggest a much more dynamic assembly of the DCC than previously thought. Such a hypothesis could be further tested by measuring local exchange rates of GFP-labeled MSL3 by application of FRAP or related techniques. Another possibility would be a depth dependent quenching of the GFP signals though this seems less likely, since disappearing domains only marginally change their intranuclear position as seen in figure 10.5.

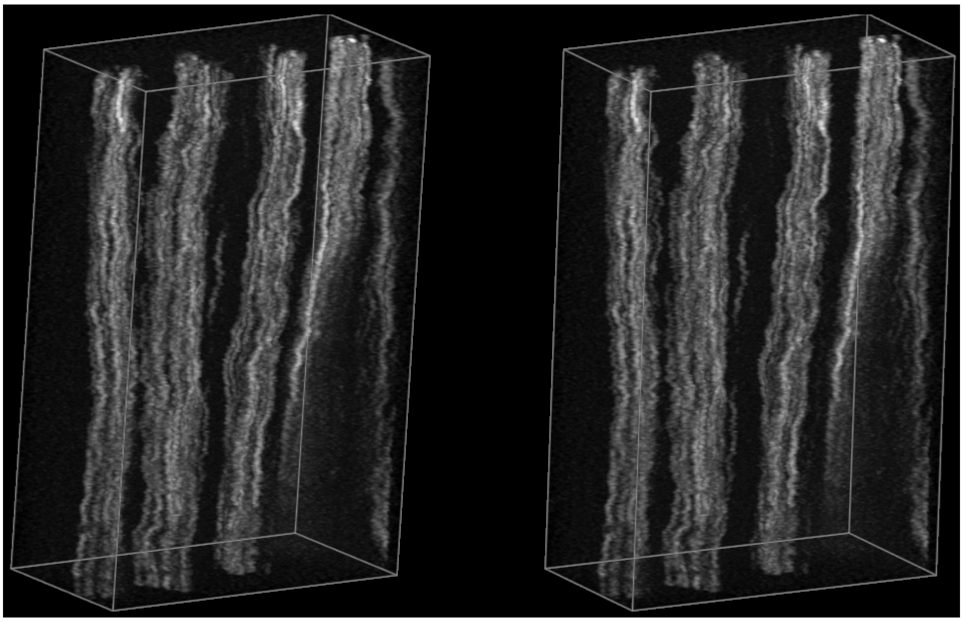

Figure 10.5: A kymograph rotates the 4D dataset so that the time axis lays in the paper plane. The volume Z-axis is mechanically projected using the OMX 3D-projection acquisition mode. The remaining 3 axis (X, Y, T) are shown in a stereo view. To demonstrate this the dataset from figure 10.3 is used. Four neighboring nuclei are shown with time being displayed in the downwards direction. The width of the displayed area is about 200 μm. The second nucleus from the right is the one marked in figure 10.3. The total timespan displayed is 5 minutes.

10.6 Model-based motion analysis

As a new approach for understanding chromosome dynamics I combined chromosome imaging with chromosome modelling. This was inspired by reflecting on how the human brain often seems to pick up a rather clear picture even when presented with noisy images. If you "sit back" from the computer screen, structures are often more apparent than when looking too close to the details of the image. Secondly, watching moving pictures of chromosome dynamics can often bring out a connecting theme that disappears as soon the movie is stopped. Our explanation of these two phenomena is that our brain seems to constantly go back and forth between the seen image and a interpolated model of the seen image.

To implement this I adopted an algorithm used for fitting electron microscopy images to X-ray crystallography based polymer models [Korostelev et al., 2002; Topf and Sali, 2005]. In crystallography the model connects atoms with chemical bonds at scales of a few Ångstrom. For our fluorescent chromosome data the equivalent scale would be around 100 nm. The "atoms" would be the MSL3 domains seen in our images. And the "bonds" are conceptual rather than physical elements that ensure connectivity between the visible spot along the chromatin.

The underlying equation represents the image as a mountainous landscape where the atoms are trying to roll downwards into the valleys which are the regions where the data pixels are brightest. The atoms are mathematically represented as n-dimensional Gaussian bell curves that give them a characteristic radial dimension. The "potential energy" E_{pot} is calculated as the sum of the cross-correlations of the atoms and the image landscape over all atoms. Additional terms of E_{pot} are given by a parabolic "spring-force" modelling the bonds and by a quadratic angular term that gives our chromosomes a preferably straight configuration rather then having them folding back on themselves. This last term though suggests that the model should be applied to sections of the chromatin instead of trying to follow the whole chromosome folded back and forth within the nucleus. These section-wise models could then be strung together in a second pass of the simulation.

The minimization of the potential energy (quantifying the data model mismatch) is computed via a molecular dynamics engine. Gradients are calculated by pixelwise evaluation of the analytical n-dimensional derivative of the cross-correlation and all other terms in E_{pot}. To better navigate through local minima an adjustable random-force term is added and to stabilize the simulation an – also adjustable – friction force ensures that the kinetic energy gradually dissipates so that a final "best fit" is obtained.

The model fitting a sub-region of the MSL3 data is shown in figure 10.6. A sequence of 12 time points is shown. It can be seen that the model finds a good overall fit to the chromosome segment while being able to "bridge" time points where spots have temporarily disappeared. One has to be aware though, that specific connections made by the simulation might not match an intuitive tracing. For example, in the last three images one would likely not place a connection into the bulky part of the chromosome, instead one would judge that the lowest two domains of the left-most image in the bottom row have merged. For further discussion see section 18.10.

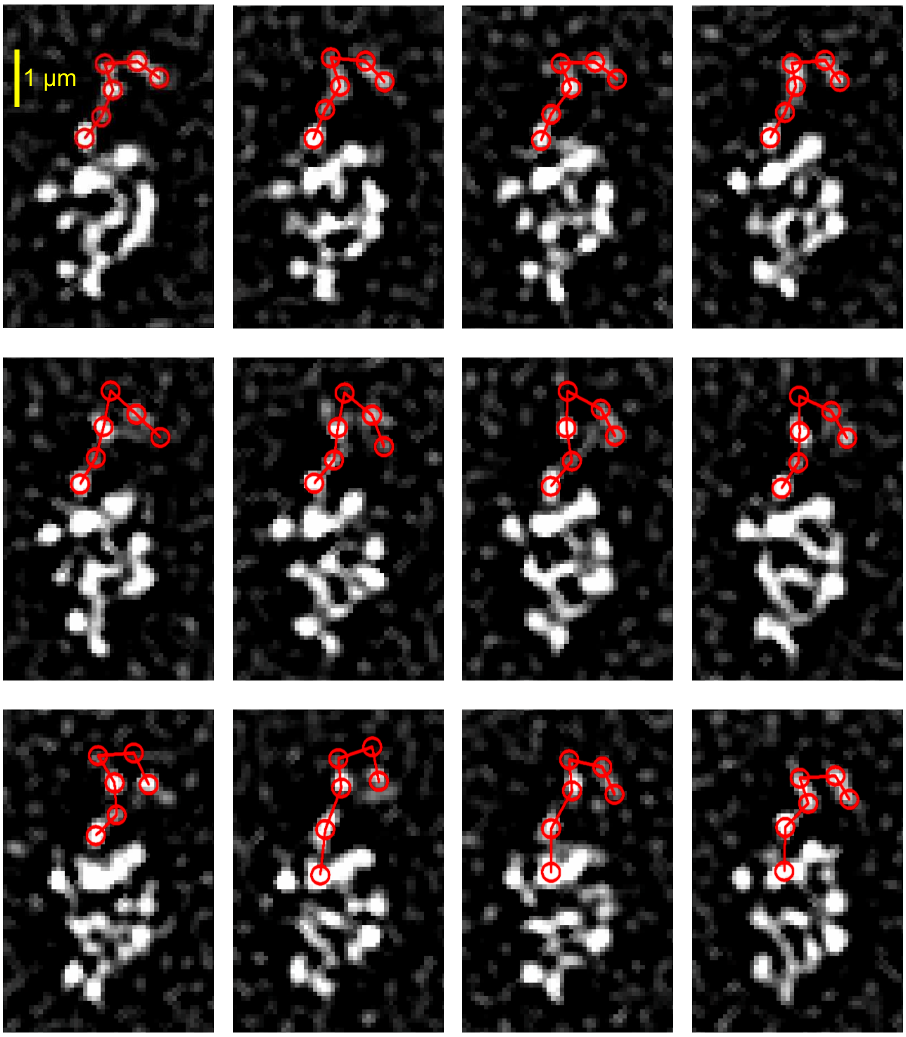

Figure 10.6: A time series of images showing sub-second chromosome dynamics is automatically traced. A simple model, that assumes that chromatin is following a linear chain, is fit to the data. The best fit is found using constrained optimization combined with a molecular dynamics simulation of soft spheres connected by directional bonds.

Chapter 11

Chromosome structure in SIM

The understanding of mitotic chromosome condensation is not very well developed [Swedlow and Hirano, 2003]. Condensation is important for the segregation of sister chromatids. DNA condensation is achieved on multiple levels. It is well understood how, on the lowest level, a linear compaction of the DNA molecule achieves a 6– to 7–times length reduction in the nucleosome. The next level forms the so-called 30 nm fiber with another 6– to 7–fold reduction in length. To succeed in cell division and not being broken during mitosis, chromosomes must be significantly shorter than the 5–20 μm separation resulting from the movement in anaphase of animal cells. Consequently further higher order folding schemes are needed to achieve a final 10,000– to 20,000–fold linear compaction.

One classical model suggests incremental orders of folding or helical coiling of the 30 nm fiber [Inoué and Sato, 1964; Sedat and Manuelidis, 1978; Belmont et al., 1987]. Classic experiments involving high-salt extraction of chromosomes produced a structure containing a proteinaceous axial core decorated by a series of DNA loops [Stubblefield and Wray, 1971; Paulson and Laemmli, 1977]. Together with other experiments these suggest the presence of a chromosome scaffold. DNA seems to be attached by dedicated regions (scaffold attachment regions, SAR; [Boy de la Tour and Laemmli, 1988]) to a special component of the scaffold called DNA topoisomerase II (topo II). Recent studies by Laemmli et al. suggest a helical coiling of the chromatic fiber on the highest level [Maeshima and Laemmli, 2003; Boy de la Tour and Laemmli, 1988].

11.1 Anaphase chromosome structure

Using the protocol described in section 19.2 we have prepared primary cell cultures from 4–5 hours (at room temperature) old *Drosophila* embryos. Suspension of primary embryonic culture was deposited on poly-L-lysine coated coverslips and fixed with 2% fresh made formaldehyde in buffer A. DAPI in buffer A was used to stain DNA. Samples were mounted in VectaShield. These were then imaged by Structured Illumination Microscopy. All SIM imaging was done using a 100x oil objective.

Figures 11.1 to 11.5 show various high resolution images of anaphase chromosomes. Most of the time chromosome arms are seen side-on, i.e. they are aligned along the image plane (figure 11.1, 11.2 and 11.3). However, sometimes they are found to be perpendicular to the image plane. In these cases a higher resolution, lateral view of the end-on cross-section of the chromosome is obtained (11.4 and 11.5). Comparing 11.4 and 11.5 it is apparent that not all chromosomes have the same structure: While in 11.4 the cross section appears homogeneously speckled, the chromosome in figure 11.5 is thinner (by a factor of two – note scale bars!) and shows a "ring-structure" in cross section: The central axis along each chromosome appears darker than the outer shell layer along each chromosome and therefore appears to contain less DNA. The outer layer of about 150 nm is about a third of the total chromosome arm diameter of about 400–500 nm. The chromosome arm shown in the top right of figure 11.1(c) shows the same structure from the side: Two brighter outer bands with a central darker region in the middle. Matching the dimensions above the brighter and darker bands are respectively 150 nm and 400 nm in size. Figure 11.2 shows similar structures in some optical sections (e.g. at the two arrow heads in section 7); here however, the overall structure of chromosome arms appears "wildly twisted" (e.g. as indicated by arrow head in sections 6). Figure 11.3 shows a speckle structure similar to the chromosome seen (in cross-section) in figure 11.4. For an interpretation see chapter 16.

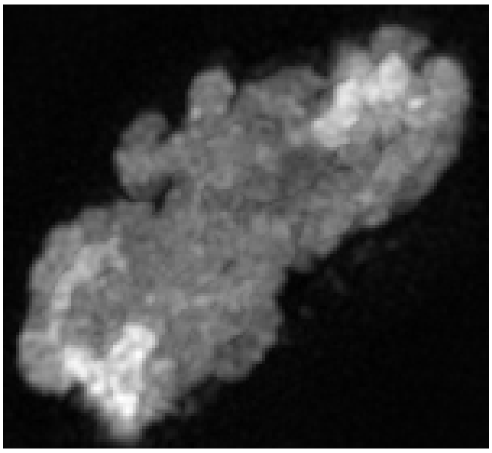

(a) maximum intensity projection

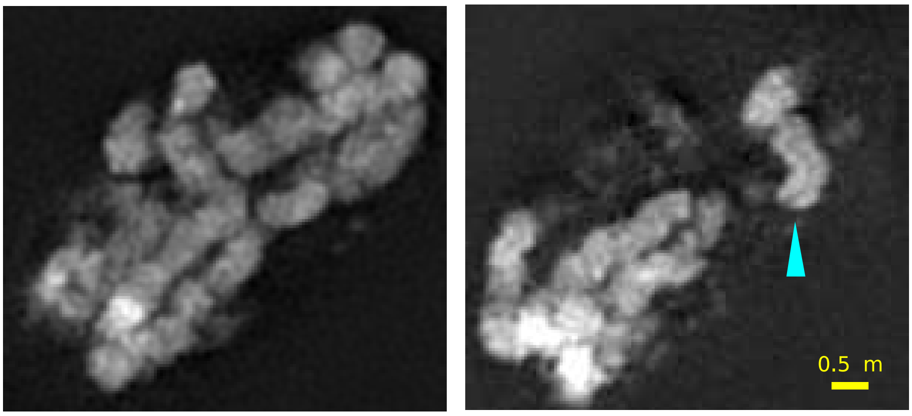

(b) optical section

(c) optical section

Figure 11.1: A maximum intensity projection over the entire volume and 2 different optical sections .875 μm apart. The second section shows a characteristic dark line along the center of the chromosome arm (arrow).

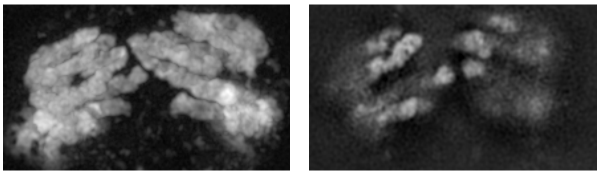

(a) maximum intensity projection

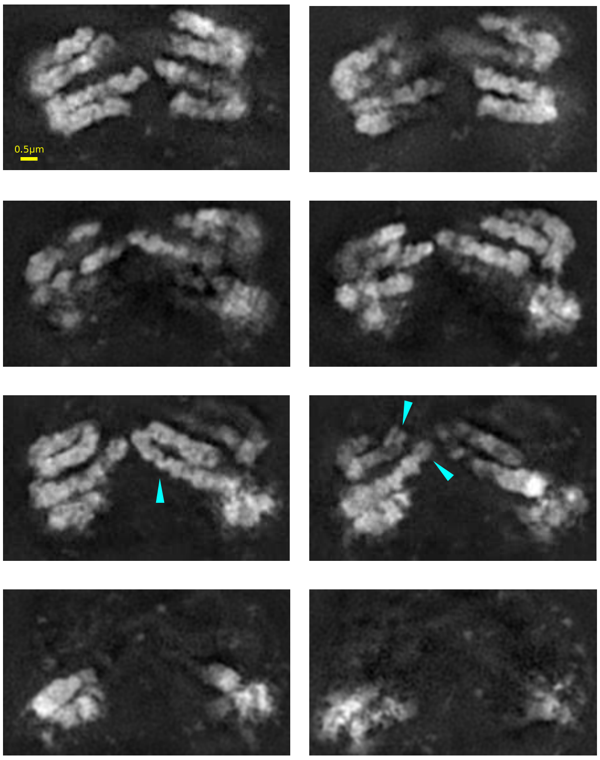

Figure 11.2: A maximum intensity projection over the entire volume and 9 different optical sections are shown. The sections are .375 μm apart. Some sections show the center of a chromosome appear darker than the outer shell layer (2 arrows in 7th section). Overall multiple chromosome arms appears "wildly twisted" (e.g. see arrow in 6th section).

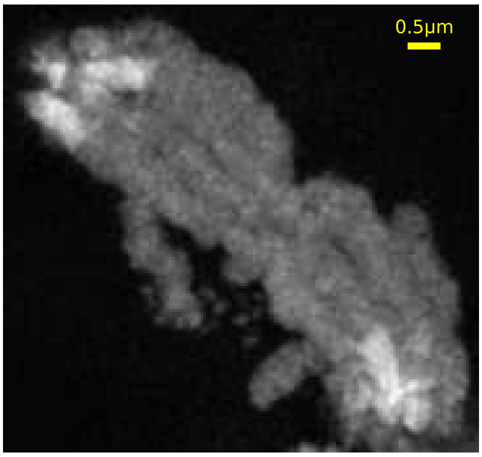

(a) maximum intensity projection

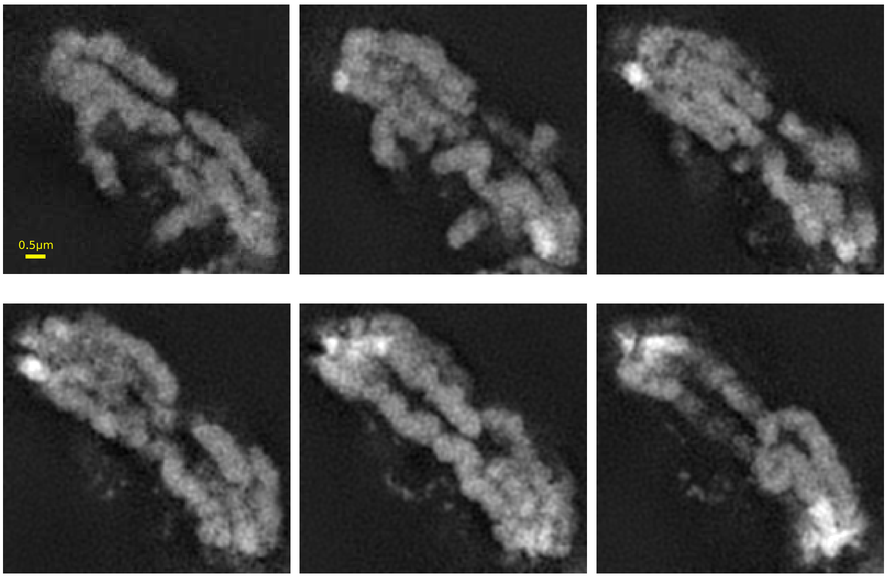

Figure 11.3: A maximum intensity projection over the entire volume and 6 different optical sections are shown. The sections are .375 μm apart.

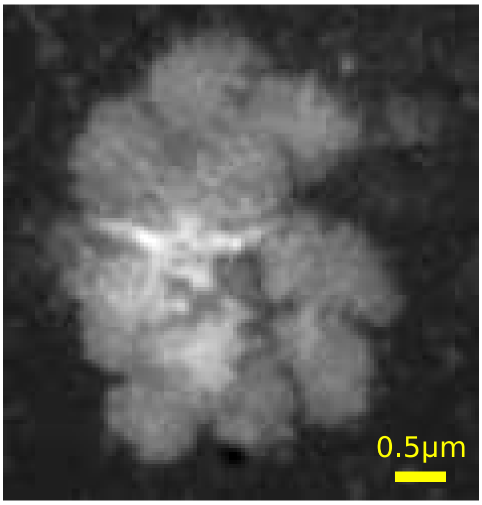

(a) maximum intensity projection

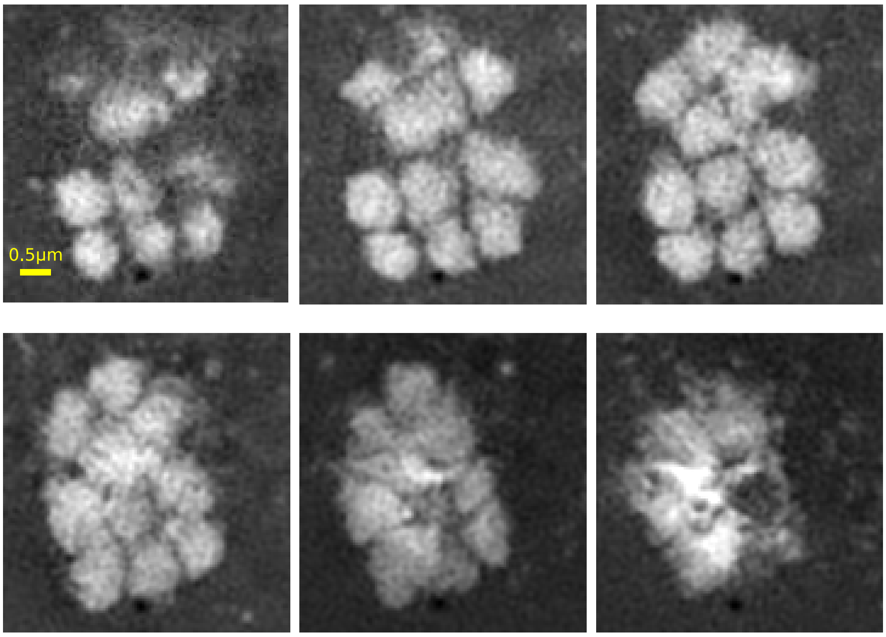

Figure 11.4: These chromosomes are perpendicular to the image plane. The chromosomes are relatively large and appear homogeneously speckled in cross section. (A maximum intensity projection over the entire volume and 6 different optical sections are shown.)

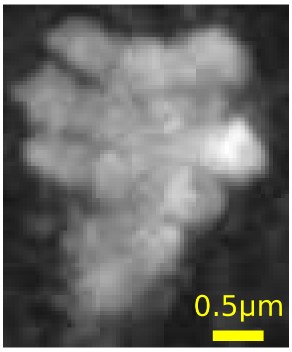

(a) maximum intensity projection

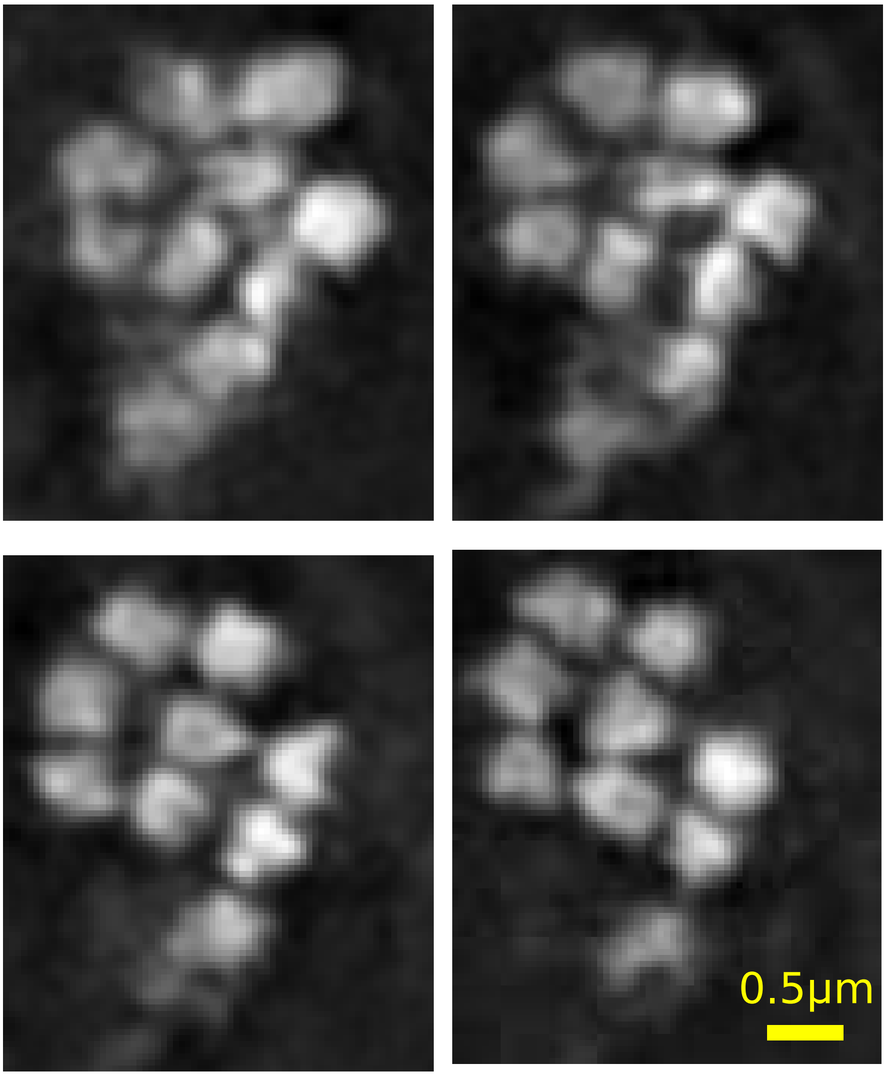

Figure 11.5: These chromosomes are perpendicular to the image plane. The chromosomes are relatively small and show a “ring”-structure in cross section. (A maximum intensity projection over the entire volume and 4 different optical sections are shown.)

Chapter 12

Polytene chromosomes in SIM

Cells with more than two sisters of homologous chromosomes are called polyploid. In certain cell types of fly larvae, however, the sisters are aligned side by side, like drinking straws in a box, creating a single polytene chromosome. By the alignment corresponding condensed and open chromatin regions are arranged in register forming the reproducible banding pattern that is a hallmark of polytene interphase chromosomes [Bauer and Beermann, 1952; Zhimulev, 1996]. It has been shown that these polytene chromosomes sometimes disperse to form conventional polyploid cells. Consequently, they must be closely related and the basic band/interband structure of polytene chromosomes may be similar to that of normal interphase chromosomes.

In salivary gland cells of *Drosophila* larvae replication goes through 10 cycles without separation of daughter chromosomes. The resulting polytene chromosomes are therefore made up of 1024 (2^{10}) identical strands of chromatin. *Drosophila* has four chromosome pairs. In polytene chromosomes however the pairs are tightly paired so that each pair appears as one structure. For chromosome 2 and 3 two arms (left and right) are distinguished so that the total set of chromosomes is labeled as X, 2L, 2R, 3L, 3R and 4.

To visualize *Drosophila* polytene chromosomes fly larvae were dissected. The salivary glands were squashed between a glass slide and coverslip. Before staining the preparations were screened and selected on a conventional inverted phase contrast microscope. Only DAPI staining was applied. Figure 12.1 shows parts of the X chromosome. Shown are the images acquired by conventional wide-field microscopy, the deconvolved image and the image acquired by SI microscopy. The region 8E1 to 9A1 is marked. It can be clearly seen that SI shows more bands in much more detail.

In figure 12.2 this region is compared to an image acquired with electron microscopy (courtesy of Dr. S. Demakov, Novosibirsk). All bands visible in the EM image could be easily mapped to bands seen in SIM. Also visible in SIM are the longitudinal chromatin fibers at the end of region 8 which are invisible in conventional light microscopy and are only known from EM images.

Figure 12.3 shows such fibers imaged on a different chromosome section 2R(?). Multiple groups of longitudinal fibers are clearly distinguishable. On a lateral view of the chromosome shown in figure 12.3 I count on the order of 10–12 such fibers. The observed diameter of single chromatid bundles is in the order of 140 nm, similar to such bundles observed in EM. The resolution obtained under *in situ* conditions on a biological sample is unprecedented by any other existing microscope, demonstrating, that SIM can be used to close the gap between light microscopy and the EM.

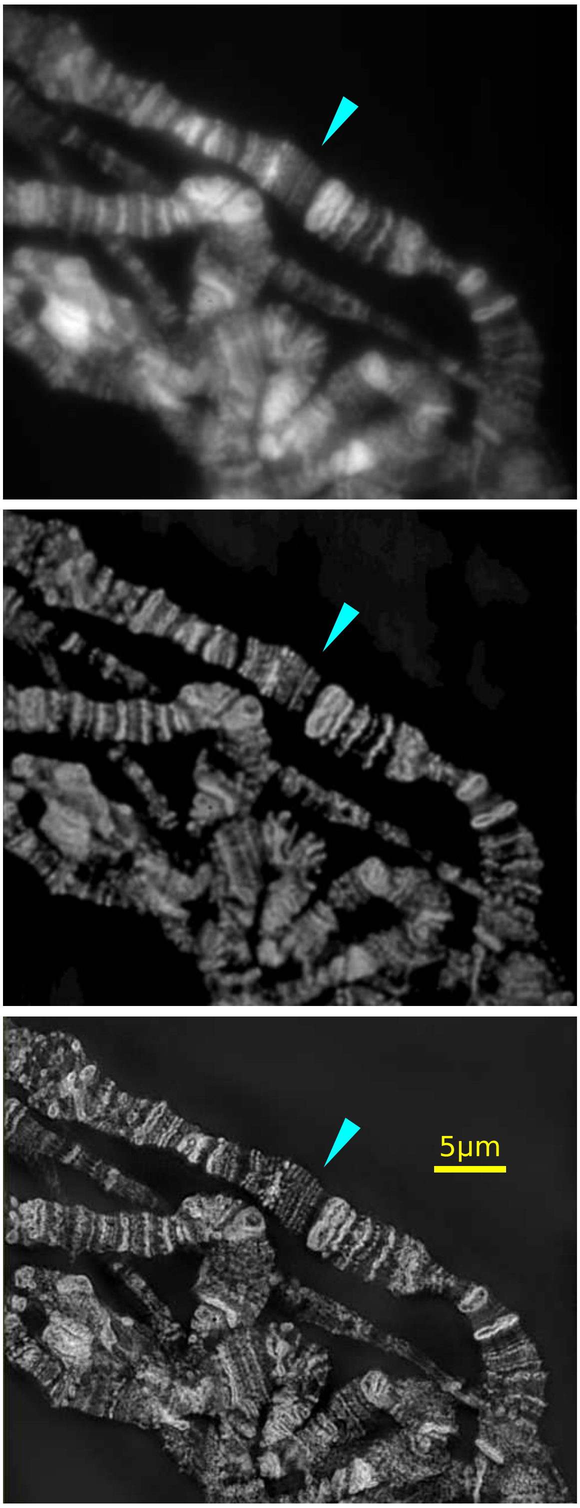

Figure 12.1: A *Drosophila* polytene X chromosome shown in conventional wide-field, deconvolution and SI mode. Shown is a section of the X chromosome with the marker pointing at the 8E1 to 9A1 region.

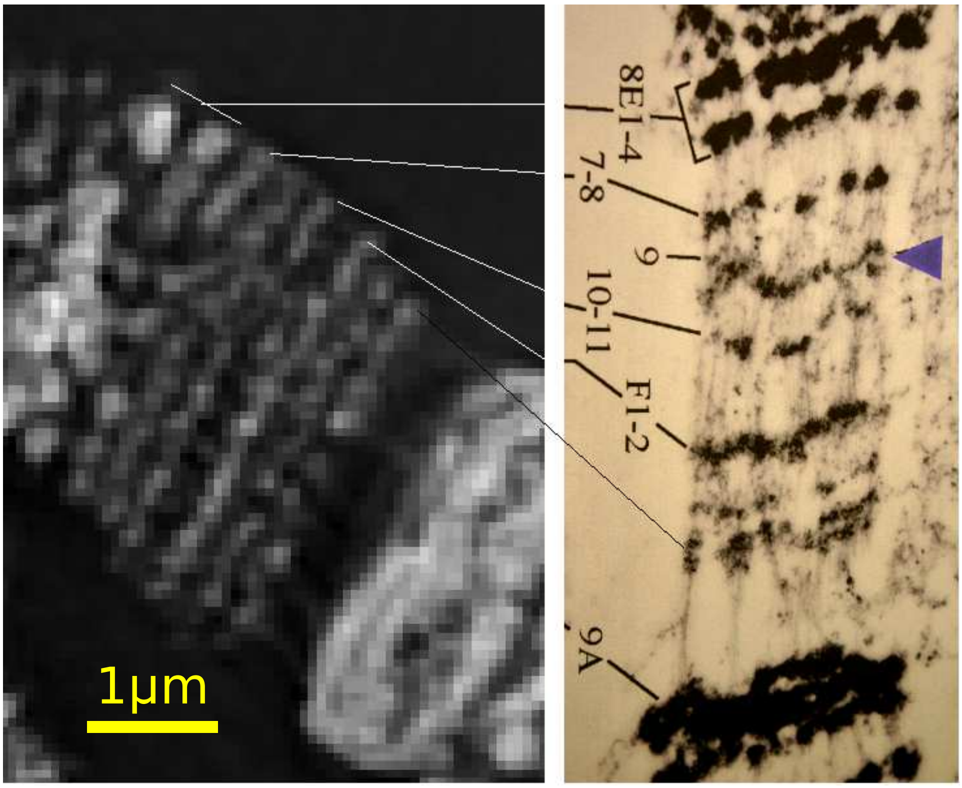

Figure 12.2: Comparison with electron microscopy shows that every known band can easily be recognized in SIM. Shown is the same 8E1 to 9A1 region on the X chromosome.

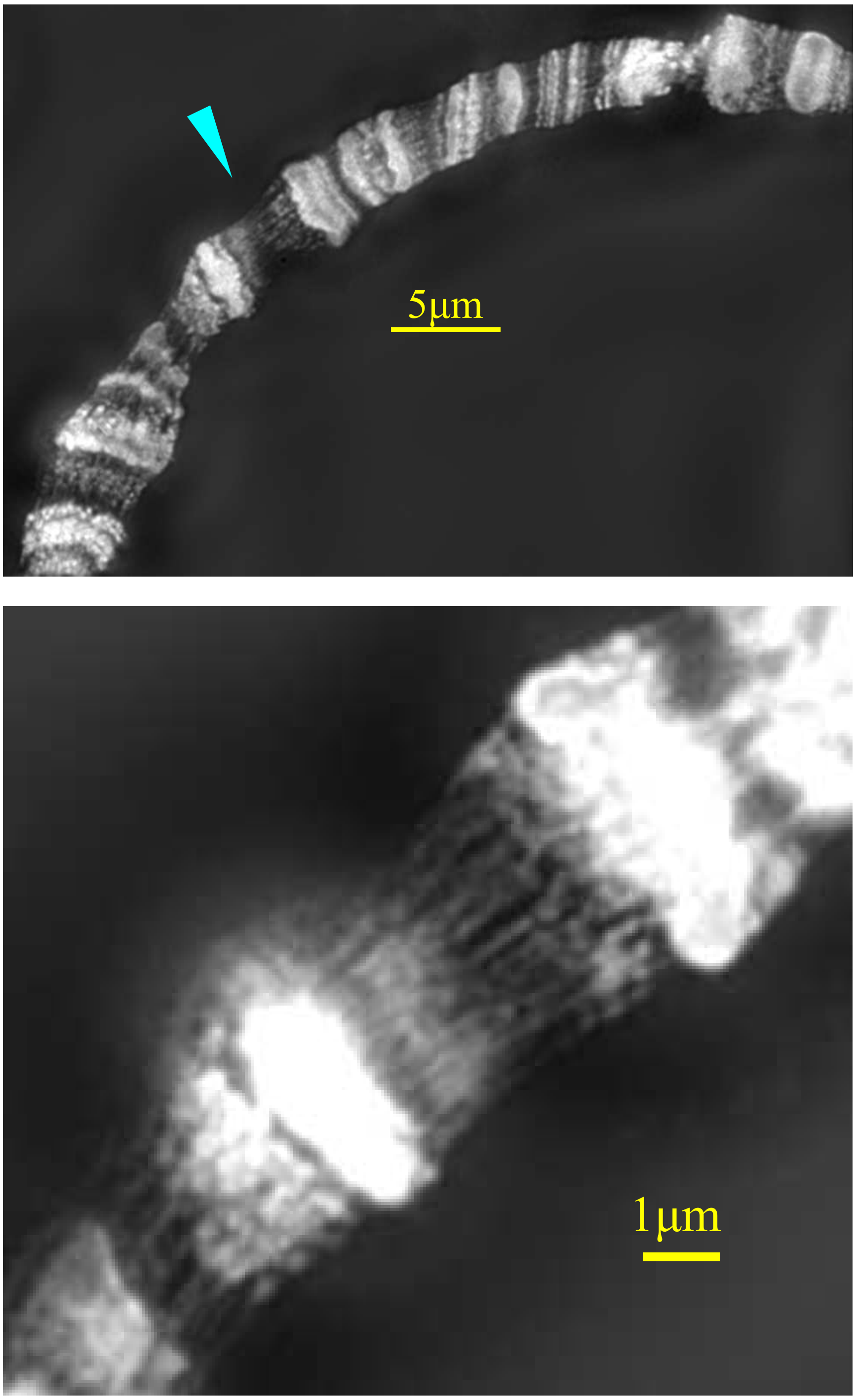

(a) sub-region

Figure 12.3: SIM can visualize longitudinal chromatin fibers in polytene chromosomes. Before these were only known from electron microscope images. The region shown is on the 2R(?) chromosome.

Chapter 13

Nuclear pores in SIM

In order to transport RNA and other molecules into and out of the the nucleus, the double membrane surrounding the eukaryotic cell nucleus is perforated by numerous channels. These nuclear pores are formed by large membrane spanning protein complexes of about 120 nm in size. A schematic diagram is shown in figure 13.1. In total an animal cell contains about 3000–4000 nuclear pore complexes inside the nuclear envelope.

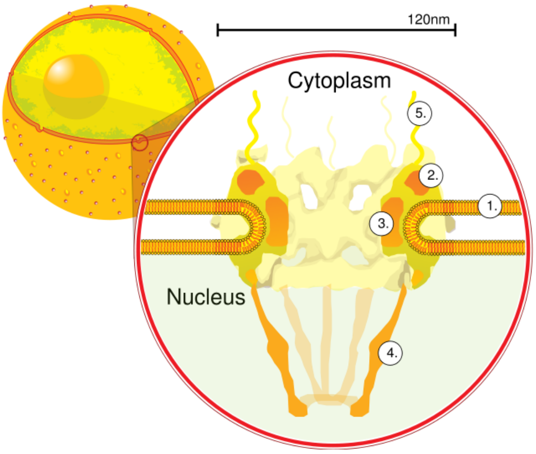

Figure 13.1: A schematic diagram showing a nuclear pore. The cell nucleus is sketched together with nucleus in the top left. The nuclear envelope contains about 3000–4000 nuclear pores. The schematic in front shows a side view of a single nuclear pore. 1. Nuclear envelope. 2. Outer ring. 3. Spokes. 4. Basket. 5. Filaments. [Wikipedia, 2006b]

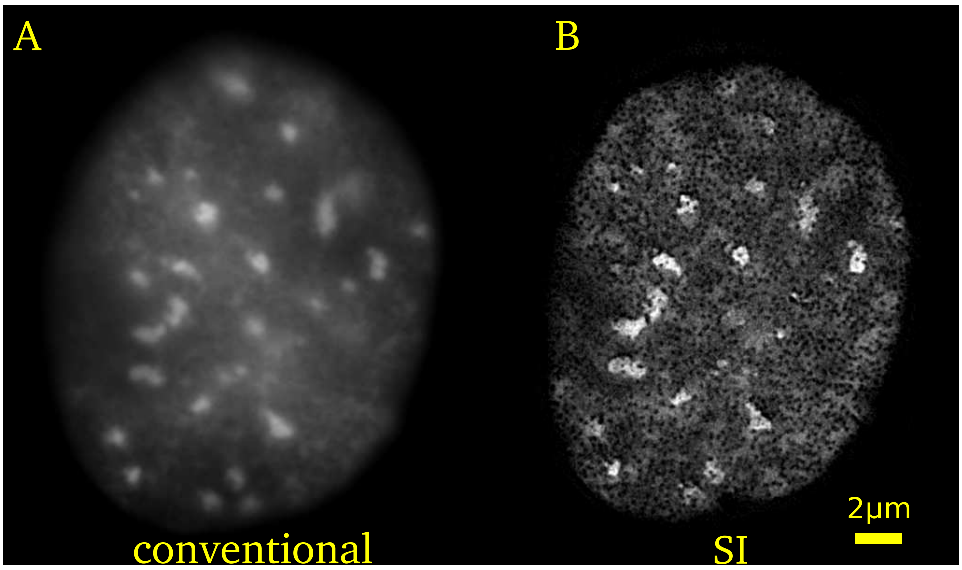

Figure 13.2: (A) Nuclear pores are not resolvable with conventional microscopy since their size is smaller than the diffraction limit. (B) However, Structured Illumination Microscopy shows clearly that the nuclear pores exclude the DAPI staining visible everywhere else in the nucleus. Shown is a single optical section through the nuclear envelope.

Condensed heterochromatin is often found at the nuclear periphery, however, as seen in the EM, nuclear pore containing areas are free of heterochromatin consistent with the observation that the inner side of nuclear pores appears to be a site of transcriptional activity. Since the pore is smaller than the Abbe diffraction limit, the nuclear pores in the envelope cannot be seen with conventional microscopy. Figure 13.2 compares the conventional image with the SI image both taken on OMX. Each shows DAPI staining in the same optical section through the nuclear envelope. In the conventional image only the heterochromatin is seen as bright spots. In the SI image dark holes are clearly visible where the DAPI staining is excluded by the nuclear pores.

To confirm the identity of the dark spots as nuclear pores, in a different preparation the nuclear pore protein Nup153 was detected by immunofluorescence using Alexa-555-conjugated secondary anti-bodies. Figure 13.3 shows that the dark spots in DAPI co-localize with the nuclear pores. The samples are mouse C2C12 myoblast tissue culture cell and were kindly provided by Lothar Schermelleh (LMU Munich).

These images are the first demonstration of resolving nuclear pore complexes after immunofluorescence labeling. Being able to resolve each pore allows to initiate new studies. Apparently, in tissue culture mouse cells, the pore distribution is uniform over the nuclear envelope surface and its density could be measured as a function of cell cycle stage or other various parameters.

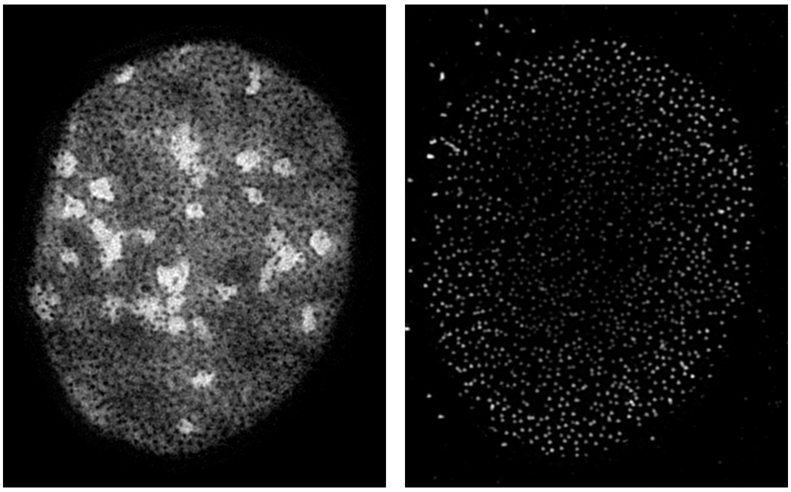

(a) DAPI (b) nuclear pores

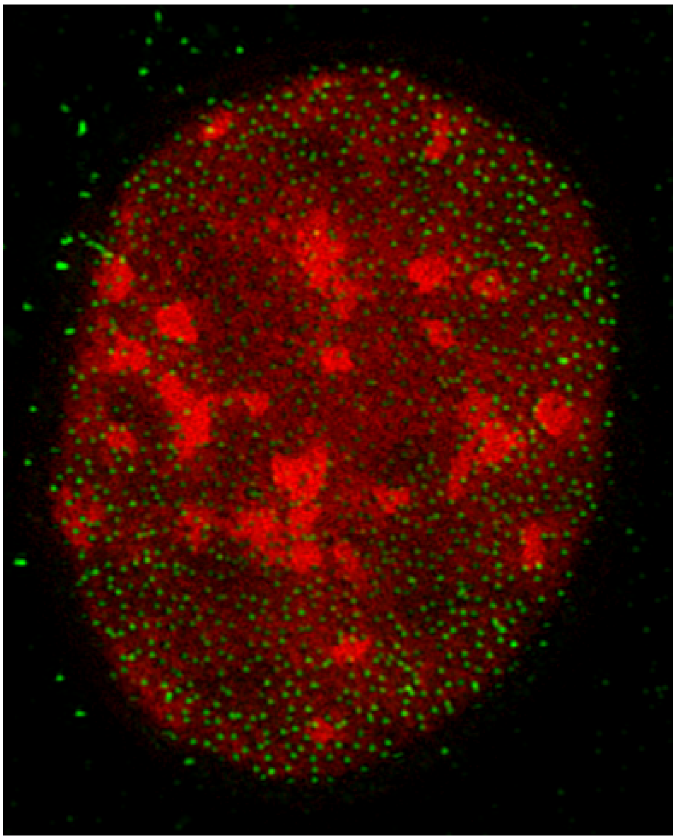

(c) overlay

Figure 13.3: The nuclear pore protein Nup153 was detected by immunofluorescence using Alexa-555-conjugated secondary antibodies. The protein co-localizes with the dark spots where DAPI staining is excluded. DAPI is shown in red, Alexa-555 is shown in green. If the two were not co-localized the Alexa-555 spots would appear in yellow.

Part IV

Discussion

Chapter 14

Ultra-high resolution microscopy

OMX is the first microscope featuring Structured Illumination [Gustafsson, 2000; Gustafsson et al., 2007] that is geared towards biological research. The resulting images show a considerable increase in resolution. Features smaller than the diffraction limit become visible and images can often be directly compared to equivalent electron microscopy images. At the same time, the advantages of fluorescent light microscopy, namely the much simpler sample preparation and the high specificity of the various fluorophores, are still preserved. So far up to three different fluorophores have been imaged in a given sample.

Recently other techniques were developed to increase the resolution of optical microscopy (see a review by [Heintzmann and Ficz, 2006]): STED (stimulated emission depletion microscopy), PALM (photoactivated localization microscopy), near-field scanning optical microscopy (NSOM), and SSIM (non-linear saturated structured illumination microscopy). All of these promise to improve the image resolution by another factor of two to ten. However each method has its specific inherent limitation. None have been demonstrated on living samples.

STED [Klar et al., 2000] is a confocal scanning method. Here a carefully shaped, very short and very intense laser pulse quenches all fluorophores in the immediate sub-resolution neighborhood of the to be observed object point. Consequently, the resolution at that point can be (almost) arbitrarily good. Obviously a big concern here is the intense light pulse, which could potentially destroy the sample. However, some initial results on biological samples have been demonstrated [Willig et al., 2006]. STED is limited to a sample depth of ≈ 2 μm and the data acquisition is so far restricted to one optical section, therefore, producing 2D images.

PALM [Betzig et al., 2006] is a localization method. A very similar method is called STORM (stochastic optical reconstruction microscopy) [Rust et al., 2006]. These methods require special photo-activatable fluorophores. A dim laser pulse (mostly near UV, 405 nm wavelength) activates only a small number of fluorophores. This ensures that by probability only well-separated molecules are imaged at a time. Then a green laser excites these activated molecules until they are entirely bleached. Using an EMCCD camera single photons emitted by these individual molecules are detected. Each is localized to within the diffraction limit (≈ 300 nm). Since, however, each molecule emits up to possibly 10^5 photons the location measurement can be repeated 10^5 times. Consequently the location as probabilistic average is more accurate by a factor of up to ≈ 300, the square root of the number of measurements. Hence, under best circumstances, a molecule is localized to within one or a few nanometers. After the first group of molecules has been irrecoverably bleached, the next group is activated by a short-wavelength laser pulse and the procedure is repeated. The total imaging time to produce one high-resolution image is many hours. To reduce background fluorescence, imaging is commonly done using total internal reflection fluorescence (TIRF) microscopy. Hence, the 3D thickness of the observable volume is less then 1 μm.

Near-field scanning optical microscopy (NSOM) [Wabuyele et al., 2005] is not governed by the Abbe resolution limit. Instead of creating an optical image using lenses, the sample is illuminated by laser light through a fiber with a very small tip aperture (diameter of 20–200 nm) [Garini et al., 2005]. With less than 100 nm penetration depth the surface is scanned to build up a high resolution 2D image. Zero working distance and extremely long scan times, when imaging at high resolution images or large specimen areas, complicate the practical application of NSOM.

Non-linear structured illumination was recently demonstrated in our lab to produce 50 nm resolution in a wide-field (i.e. non scanning) microscope setup [Gustafsson, 2005]. The scheme was demonstrated on fluorescent beads. The non-linear optical effect was achieved using a high powered pulse laser, however this has proven to be problematic for biological samples. Reconstruction of a 2D high-resolution image requires 108 (bright) exposures. So far we have not found fluorophores that could sustain this amount of excitation energy. An alternative avenue to achieve the needed nonlinear effect requires the use of photo-switchable fluorophores. It would be necessary to be able to reliably activate and deactivate these molecules many dozen or hundreds of times. It is subject of current research to find a satisfactory working system [Gustafsson, pers. comm.]. Once these hurdles are overcome OMX could be extended to acquire data using this imaging mode.

Generally the (linear) structured illumination on OMX requires thin samples. Optical distortion induced by the mounting medium and the specimen itself allow imaging only up to 12 μm deep. This is of course always measured from the cover slip, and preparation techniques that attach the object to the glass slide, instead of the cover slip, have to be modified accordingly. Even for squashed polytene chromosome samples mounted in VectaShield, which are only about 1 μm thin, the distance from coverslip to slide was measured to be 30 μm. After adjusting the preparation method by reducing the volume of mounting medium and pressing harder to squeeze out as much medium as possible, the distance was measured to be reduced to 20 μm. While this is still considerably larger then the recommended upper limit, the resulting images were of convincing quality.

Chapter 15

Application of SIM

15.1 Higher resolution of polytene banding patterns

The method of staining DNA in fixed polytene chromosome spreads by Hoechst or DAPI is relatively simple, however due to large differences in intensity and contrast the resolution is limited in conventional fluorescence microscopy and never attains that of EM techniques. The SIM images of *Drosophila* polytene chromosomes shown in chapter 12 display a clarity unprecedented in optical microscopy. It was possible to map the band/interband pattern directly at a precision comparable to images acquired using electron microscopy. This was demonstrated on the 8E1 to 9A1 region of the X chromosome. Although this may not hold true for all chromosomal regions to the same extent, the ease of sample preparation and the possibility to map specific protein binding at similar resolution will make OMX superior to the use of EM in the near future. A careful discussion and comparison of light and electron microscopic techniques in the analysis of polytene chromosomes can be found in Zhimulev, 1996.

The SIM imaging was done using a standard squash-sample preparation technique for optical microscopy. This attaches the chromosomes to the glass slide and the large distance from cover slip resulted in an increased degree of shadowing, resulting from refractive index mismatch and as a consequence spherical aberrations (see comments at the end of chapter 14). It should be easily possible to adjust the technique so that the chromosomes attach directly to the cover slip, thus reducing the imaging depth.

The demonstrated results were only a proof of principle showing the increase in resolution. Further studies applying SI microscopy would certainly use multi-labeled samples combining the DAPI staining with specific antibody stains in the green and red channels. This could answer question regarding the specific nature of bands and interbands in polytenes. Some researchers believe that there are special sequence elements recognized by specific proteins at the band-interband boundaries limiting decondensation at the interband edges. The extra crisp images of SIM would allow to locate such boundary elements with very high precision after FISH or antibody staining.

15.2 Higher resolution of nuclear pores

Imaging nuclear pores complexes *in situ* using optical fluorescent microscopy is generally limited by the optical resolution compared to their small size of about 120 nm diameter. Assuming the pores to be non-clustered, i.e. well separated, prior studies could localize pores by combining high resolution confocal microscopy with image processing and pattern recognition [Kubitscheck et al., 1996] to within 20 nm. Resolving individual nuclear pores under physiological conditions was done by Höppner et al. [Höppener et al., 2003, 2005]. They used near-field scanning optical microscopy to study the nuclear envelope of *Xenopus laevis* oocytes. Using two different antibodies, one against the nucleoporin Nup62 and another against the nucleoporin Nup153, they could measure different fluorescent spot sizes: ≈ 60 nm for Nup62 and 80–140 nm for Nup153. The differing size can be explained by the different location of the investigated nucleoporins in the nuclear pore complex.

These studies required a sample preparation protocol that removes the chromatin from the opened nuclei. This is needed to provide the flat surface necessary for near-field scanning microscopy. The SIM images presented in chapter 13 did not require any special protocol like this. Instead, the samples for OMX consisted of entirely in-tact mouse C2C12 myoblast tissue culture cells. The resulting image data is fully 3D. In our data we measured a size of 120 ± 20 nm for both the Nup153 nucleoporin as well as for the excluded area of chromatin.

It has been shown that Drosophila dosage compensation complex interacts with nuclear pore components [Mendjan et al., 2006]. This interaction is consistent with our observations that the X chromosome in males is almost always at the periphery of the nucleus during interphase and up until prophase in neuroblasts of dissected brains of male third instar larvae or embryonic culture cells. Using the increased resolution of OMX it is possible to study colocalization of different components of nuclear pores and dosage compensation complex stained with antibodies to see if there is any physical interaction between them. Furthermore, this could be studied at different stages of cell cycle.

Chapter 16

Chromosome structure

In section 11.1 we presented high resolution structured illumination images of anaphase cells fixed in buffer A *in situ*. The cells were taken from primary culture cells isolated from 5–6 hour old *Drosophila* embryos. The images show an unprecedented level of detail in fluorescence microscopy. 400–500 nm wide anaphase chromatids exhibit substructure consisting of continuous segments of 100–150 nm in width and 0.5–1.0 μm in length. These segments appear to be the lower compaction levels of chromatin fibers which were previously only observed in conventional EM samples. However, it must be noted that during preparation for conventional EM, chromatin has to be subjected to harsh conditions of permeabilization, fixation, dehydration and embedding. This makes interpretation of the structures observed by EM problematic. Sample preparation for SIM does not require permeabilization or dehydration, so that chromatin is fixed and mounted in conditions close to the native nuclear environment. Here, we confirm independently using the extra high resolution of SIM, the existence of 100–150 nm thick chromatin fibers in non-permeabilized, fixed, hydrated samples.

Some images of anaphase chromosomes aligned along the optical axis (figure 11.5) show an apparent reduction of DAPI intensity at the core regions. Apparently the DAPI stained DNA is preferably localized inside the outer layer of a chromatid "tube". The inner diameter of the DNA poor tube-core is about one third of the total chromosome diameter ($\approx$ 150 nm and $\approx$ 450 nm respectively). This is an interesting structural feature that has never been observed in diploid anaphase Drosophila chromosomes imaged with light microscopy.

Our interpretation of these images is that an anaphase chromosome has a large coil of DNA running along the chromosome axis. This fits with models for metaphase chromosomes proposed by Maeshima and Laemmli, 2003, and by Kireeva et al. [Kireeva et al., 2004; Belmont, 2006]. As they suggest there would be an axial topoisomerase II and condensin distribution along the center of the chromatin axis occupying approximately one third of its diameter. We are preparing further multi-label experiments that will allow direct imaging of this proteinaceous part using structured illumination microscopy.

Overall we have been able to distinguish two classes of cells with anaphase chromosomes of two different sizes. The chromosomes of the first kind (figures 11.1, 11.2 and 11.5) were only 400–500 nm thick and demonstrated elaborate substructure. The chromosomes of the second kind (figures 11.3 and 11.4) were 800–1000 nm thick, and homogeneously speckled inside chromatids similar to the chromosome structure during metaphase seen by scanning EM [Sumner, 1991]. The difference in size and structure between anaphase chromosomes of the two kinds is probably due to the difference in cell type, age, developmental stage or proliferation activity.

The above discussed images of anaphase chromosomes aligned along the optical axis were taken of cells of the first kind. Most images of these cells show two parallel bands. This appearance is what you would expect from a tube-like chromosome. An optical section perpendicular to the chromosome axis appears as a ring (figure 11.5) and an optical section along the center of that tube would appear as two parallel bands (see arrow in figure 11.1). The width of these bands and the size of the groove between them matches the respective sizes seen in the end-on cross section.

However, the tube-model has to be extended. The anaphase chromosomes shown in figure 11.2 are twisted and/or coiled multiple times in some regions, while in other regions they show a tube structure (see arrows in that figure). The “orderly” coiling showing up either as a ring or as two parallel bands seems to turn into a comparably more irregular coiling. This is the first time that such twisting was imaged by light microscopy in intact, untreated cells. The images are comparable to those shown by Maeshima and Laemmli of super condensed chromosomes [Maeshima and Laemmli, 2003, figure 2D].

The images of the second kind of cells (figures 11.3 and 11.4) showing large chromosomes of up to 1000 nm thickness did not show the substructure required to fit the above proposed model. Therefore, to explain all of our images, we argue that another structuring theme for *in situ* chromosome architecture can be realized. Considering the resolution limit of $\geq 100\,\mathrm{nm}$ the largest structural element comprising the observed chromosome architecture cannot be significantly larger than that. Therefore we propose that as the cells grow larger and their cell cycle duration becomes significantly longer (from 15 minutes to several hours) – either because of age or only occurring in certain cell types – the large scale coiling from the above model for smaller chromosomes transforms into a “comparably unorganized” network of 100 (or maybe 30) nm fiber. This would compare to the network model proposed by Poirier and Marko [Poirier and Marko, 2002; Pope et al., 2006]. However, since the defining structure is below the resolution limit even of SIM the details of a model remain speculation.

This is the first study that directly observes two seemingly incompatible forms of chromosome architecture (coiling vs. network model) in one organism using *in situ* anaphase chromosomes. Variations in the durations of cell cycles and, as a consequence, in mitosis lengths, with varying exposures of chromatin to condensing factors may lead to a dynamic range of mitotic chromosome structures. It would also be informative to compare cellular blastoderm mitotic cells to fast dividing synchronous mitotic cells from syncitial blastoderm embryos in terms of anaphase chromosome structure using SIM. However, so far our attempts to do such experiments have failed due to difficulties in isolating functional nuclei from stage 4 embryos. SIM on fixed whole embryos turned out to be problematic because of several factors. One of them is the mismatch of refractive index between the glycerol-based mounting medium and fixed embryos. Another is the relatively large axial distance of the nuclei away from the coverslip due to embryo geometry. Both lead to severe spherical aberration which prohibits using the Structured Illumination technique. Possible solutions to this problem might include the use of new mounting media that give a better refractive index match, e.g. thiodiethanol [Staudt et al., 2007], or the use of glycerol objectives for SIM. The later would however require some adjustments in the microscope optics. Alternatively, one could find a way to isolate anaphase chromosomes from syncitial blastoderm embryos while at the same time preserving their native morphology.

We believe that the observed structures are not artificial due to potential changes of the native morphology of chromosomes during fixation and SI imaging. To the best of our knowledge, fixatives such as 2% formaldehyde in buffer A are the best reagents for preservation of hydrated mitotic chromosomes from non-permeabilized cells and do not lead to obvious structural artifacts in mitotic chromosomes. Structured Illumination reconstruction parameters in all documented cases were optimal or nearly optimal. The obtained anaphase chromosome images did not exhibit any artifacts, like excessive shadows, which can sometimes occur after SI image processing.

Another concern was that the observed structure may reflect non-uniform staining of DNA with DAPI. DAPI is a minor groove DNA binding fluorescent dye associating with strong preference to AT clusters. It is therefore possible that DAPI does not reflect the distribution of DNA adequately. To confirm the peripheral distribution of DNA, we have performed SIM on anaphase chromosomes stained with Draq5, a DNA dye with no sequence preference. DNA distribution stained with Draq5 was identical to DAPI showing enhanced intensity at the periphery of chromatids [unpublished data by Y. Strukov].

Chapter 17

Chromosome dynamics

The microscopy data presented in chapter 10 shows live *Drosophila* tissue cells. For the first time we acquired live images with an unprecedented temporal and spatial resolution. Using the MSL3-GFP fusion protein it was possible to image a specific small fraction ($\approx 1/20$) out of the entire diploid *Drosophila* genome. About 20 subregions are visually recognizable within each nucleus. This is the first time that a regional specific binding of the dosage compensation complex was observed on diploid interphase cells and *in vivo*. We assume that the observed cells were diploid because the size of the labeled region, as well as the size of the cells themselves, was comparable to the size seen in dividing neuroblasts from similar tissue.

In contrast, on spread polytene chromosomes ≈ 300 sites can be distinguished. This suggests that these sites are clustered on the nonpolytene interphase X chromosome with an average of ≈ 15 sites coalescing into a common domain, reflecting the 3D folding of chromatin in diploid cells. A similar clustering into intranuclear domains was observed for insulator proteins belonging to the gypsy class of insulators (Su(Hw), Mod(mdg4) and CP190) that play a role in the formation of chromatin boundaries [Pai et al., 2004]. In the following I studied the dynamic 3D intranuclear distribution of these distinct Msl-3 domains.

The various approaches used to study the data confirm existing models of constrained chromosome domain motion. Heun et al. (2001) have observed non-Brownian motion at or faster than 0.5 μm/10 sec in interphase yeast cells. Vazquez et al. (2001) report two distinguishable types of motion in *Drosophila* spermatocyte nuclei. Depending on the cell cycle stage they saw both short-range and long-range motion in early G2, while for late G2 only short-range motion remains. The fastest motion they could measure was 300 nm per sec.

Using the increased 3D acquisition speed of OMX we were able to resolve short-term chromosomal motion of up to 3 μm per seconds [unpublished data by Y. Strukov]. These “jumps” occurred in the time interval between two consecutive images. Over the time of about 100 ms between them a given MSL3 domain would exhibit this very fast motion, while the surrounding areas would remain as a constant reference frame.

Since we did not image a small number of discrete markers, but rather a continuous sequence of MSL3 domains, our data is potentially richer in information while also being harder do evaluate. Future study will combine the presented GFP-MSL3 strains with distinct loci marked by fluorescent proteins of another color. This will make the data more interpretable and allow direct comparison to prior results reported by others.

In an independent study we also confirmed through the direct observation of primary embryonic cultures that MSL3-GFP, and probably the entire DCC too, stays associated with the euchromatic arm of the X chromosome throughout the cell cycle [unpublished data by Y. Strukov]. Using OMX we have shown this watching cell cycle progression in live neuroblasts from brains of third instar larvae. Embryonic cultures from early embryos contain a significant fraction of actively and asymmetrically dividing neuroblasts, about 800 per one embryo. We used primary embryonic cultures from 8–10 stage embryos because it is a relatively straightforward way to get live dividing cell culture full of neuroblasts, stem cell like cells. Cell cycle duration in neuroblasts is 40–55 minutes, which makes it a convenient object to study. Alternatively, dividing neuroblasts could be observed in dissected brains of third instar larvae, which is also a convenient source of a large number of dividing diploid cells.

The increased spatial and temporal resolution provided by OMX could be utilized to further study chromosome–chromosome interactions. The system presented by Vazquez et al., 2006, to study long-distance chromosome interaction in *Drosophila* could be used in genetic screens to understand molecular requirements for long-distance interactions. It is possible to undertake live-studies of these interactions to investigate the mode of chromosome dynamics: directed active movement or Brownian motion. It is still an important question in cell biology, if chromatin dynamics is passive and driven by thermal motion, or if chromosomes are pulled by some protein complexes that use the energy of ATP. The increased resolution capabilities of OMX would allow for live observations that could help answering these questions.

In another project in our lab we have generated fly lines with lac-operator inserts into defined sites on one of the arms of the second chromosome. Expressing GFP-labeled lac-repressor molecules in the same flies allows visualization of these sites in 4D [Vazquez et al., 2006]. One possible direction is to use fly embryos, homozygous for the labeled second chromosome, for studying the mechanisms of homologous pairing. Several models have been proposed: (a) "stochastic" model: homologous pairing is initiated at one or more sites randomly distributed along chromosomes and then later entire chromosome gets paired as a result of Brownian motion dynamics; (b) "zipper" model: pairing is reproducibly initiated at a certain site or sites and then pairing, not unlike in a zipper, is spread along the rest of chromosome. Chromosomal pairing in *Drosophila* occurs at cell cycle 14, around cellularization, the first cell cycle with long interphase. Using OMX the dynamics of the homologous lac operator spots could be followed *in vivo* with high temporal and spatial resolution.

Chapter 18

Further remarks

18.1 Multi color alignment

Different wavelengths are always imaged by separate cameras. Since there is generally a non-zero lateral displacement of the different CCD cameras relative to each other a special procedure for post-aligning the color channels is needed. The misalignment consists of both a translational offset and an angular rotation. Chromatic aberrations also contribute to the cross-channel misalignment, but since it is in the axial or focus direction it can be treated separately. Of course these are also not special to the OMX multi CCD design, but occur similarly on a single-CCD microscope.

The most general approach to determine the alignment parameters requires the use of multi-color bead slides. However, often the remaining wavelength bleed-through visible from biological sample features can be used to facilitate alignment. Alignment parameters have been found to be stable over many days. They tend to change after the optics-drawer was changed. The rotational angle parameter was found to be constant across drawer changes.

18.2 Spectral overlap – bleed-through correction

Designing filters and dichroics is always based on a compromise: A given wavelength band should be narrow enough to separate different fluorophores, but it has to be as broad as possible to not unnecessarily reject photons coming from the "correct" fluorophore. For OMX we decided to have broad wavelength bands and "open" the emission filter as much as possible. This is done because fast live imaging will always be limited by the total number of available photons. To correct the bleed-though an iterative algorithm should optimize for changing background levels. However, as a first approach a standard linear unmixing approach [Zimmermann et al., 2003; Zimmermann, 2005] has been implemented and produced a proof-of-principle that the OMX filter design is a viable choice.

18.3 Deconvolution and PSFs

Together with the development of the OMX microscope, we realize that a similar effort should be made to improve image processing and restoration. As discussed in Wallace et al. (2001) image deconvolution methods are in routine use today. New approaches however could improve on limitation in sample thickness by using phase retrieval methods developed in our lab [Hanser et al., 2003]. Using this method, sample sections distorted by more depth related aberration are deconvolved with an equally more aberrated PSF. To conserve computer memory the PSF is represented by using a concept called pupil functions. A second direction to improve the deconvolution algorithm was studied to reduce artifacts stemming from sub-optimal PSFs. This new type of deconvolution is called myopic deconvolution [Hom et al., 2007]. The myopic deconvolution equation could be rewritten using the pupil function formalism rather than operating with the full 3D PSF. This way it could be combined with the depth-dependent convolution.

A practical approach to improving the deconvolution performance was demonstrated in chapter 8. By automatically locating many well separated beads, acquiring their 3D images and finally averaging these, I generated a PSF with exceptionally low noise levels. The radially asymmetric fine-structure seen in the PSF might give clues about optical features of the objective and / or other components of the microscope. Its use for improving the deconvolution performance warrants further study. We could show a small but statistically significant improvement when deconvolving a bright data set. However, data sets showing a smaller signal-to-noise ratio did not show a conclusive improvement.

In practice all the deconvolution of OMX data is currently done using a measured PSF from a single bead – no multi-bead averaging is done. The PSF is then radially averaged. The PSF used for SIM image reconstruction is acquired using only one of the three angles usually done for standard 3D-stack SIM acquisition. This is possible because of the assumed radial symmetry. Future study and implementation of a more streamlined data reconstruction "pipeline" should improve on this and use the (theoretically) better approach discussed in chapter 8.

18.4 Software development

The core of the main OMX (GUI) program is written in C++. This is mostly a leftover from a historical choice made before Python code was added. A rewrite of the program would probably follow the approach used by UCSF Chimera [Pettersen et al., 2004] where only sub-modules requiring the extra speed of C++ are written in C++, while the main (starting) application is written in Python. This rewrite however *did* happen for all other programs running of the various other PCs making up the OMX system. The resulting development flexibility and new transparency provided by the Python Remote Object library (pyro) have justified this (I hope).

The early choice of wxWidgets as a the GUI programming library has proven to be a good one. The provided widget set is extensive. Most importantly the wrapper library wxPython allowed a very smooth and gradual transition to Python, so that now about 95% of the user interface code has migrated towards Python while the integrity of the C++ widget object stays intact.

Problematic was the use of the TCP socket class provided by wxWidgets. Real-time network communication requires the deactivation of a special TCP option – the so called Nagel-algorithm is by default on, and delays each command up to 80 ms to optimize for network bandwidth usage instead of speed. I proposed to add the possibility to deactivate Nagel's algorithm into the wxWidgets socket class, but concerns were raised by the original author that it might not work across different operation systems. So I had to "hack" the source file defining the underlying socket implementation as used by OMX. Switching to pyro eventually made changing the wxWidgets code unnecessary.

My general experience is that the volunteer based support of the many Open-Source projects used for the OMX and Priithon platforms is very dependable: problems are often solved within a few days and questions are frequently answered within the hour.

Future development of the OMX GUI program should port the application to run on GNU/Linux. The advantage would be higher productivity and higher security. The critical security aspect includes the simple fact that MS-Windows computers are constantly at risk of being infected by a new computer virus. At UCSF this occurred twice over the course of the past three years, even though our lab is behind a computer fire-wall. Using Linux would alleviate this risk. The increased productivity would come from the plethora of available software packages and the direct accessibility of the common working environment like the users home directory and access to all remote network disks using the correct user read/write permissions. Linux, as opposed to Windows, transparently supports multiple users and customizable program settings would be possible.

18.5 Andor iXon EMCCD cameras

The general experience with the Andor iXon EMCCD was positive. Often cumbersome though were the frequent updates through the various hardware and software versions before we received the final camera models. Many software updates included unannounced changes that would break existing code. However, support by telephone to Northern Ireland was good enough so that these incompatibilities could mostly be addressed within few days. The EEPROM reprogramming discussed at the end of section 4.7 that was needed to fix the drifting baseline is not documented at all! It requires editing a specific file in the Andor program application directory and adding the text `debug=1` at the right place. Once in the Andor CCD program the key command `Alt-v`, which is also not documented anywhere, opens an otherwise hidden dialog window. Most importantly, the allowed values of what to set the increased[1] border size to was never officially confirmed by anyone from Andor Technology.

All cameras that we received from Andor did not show bad or hot pixels. The only exception was the most recent camera that is installed on the FITC channel: a group of about 5–10 neighboring pixels in the center of the image measure systematically low counts.

18.6 LMX

Requiring a separate second microscope to support sample finding in a convenient way was initially regarded as a weakness in the OMX design. In fact the LMX concept was only added once initial calculations showed that scanning the entire slide exclusively using the 100x objective on OMX would take on the order of 20 hours. Having the LMX microscope is now seen as a very powerful and "experience enhancing" addition to the OMX system.

A technical complication when using LMX is the required re-alignment once the slide is on OMX. Under favorable circumstances the residual offset is less than 100 μm. Then only a 3 by 3 MOSAIC is needed to be acquired on OMX before matching features are found and the LMX navigation map can be shifted into place. However, the long lever arm on the LMX stage slide mount (about 25 cm beyond the kinematic 3-point mount) is not robust enough and can easily be "kicked" by accident and the alignment is off by almost 1 mm. Regular re-centering is needed. This is quickly done with a special cross-hair slide and some gentle knocking onto the side of the mount. A redesign avoiding the long lever arm would be desirable but not trivial.

The reproducibility of the OMX stage permits that acquired navigation maps for a given slide can even be reused after days without having to retake them. On the other hand, the non-realtime nature of the navigational information requires prefect control of the specimen being attached to the slide. If for example a living *C. elegans* worm is moving by any distance larger than maybe 0.1 mm the map acquired on LMX is rendered useless.

---

[1] In the dialog the actual number specified is the size of the border that is "electronically hidden". Consequently this number needs to be *decreased* towards the theoretical—but not working!—maximum read image-size of border = 0.

The same applies to cells or cell-clusters that might detach from the coverslip. The only conceivable solution to these kinds of scenarios would be to install a CCD camera above the OMX objective. This could be mounted in place of the DIC optics onto the Z-tower and an objective of reasonably low magnification could monitor the current slide in real-time.

18.7 Flat fielding

Flat fielding is a standard procedure to post-process CCD images. This is done in the same way for microscopy as it is done for telescope images in astronomy [Howell, 2000]. A problem specific to microscopy though is the dependence of the flat-field image on the focus position. Because of the much higher numerical aperture light rays throughout the optical system are not parallel anymore and their incident angles change with the focus position. As a consequence dust spots change their apparent size and contrast. Applying a flat field image acquired at a different focus position will then only correct dust spots in an approximate way and might in fact introduce high frequency rings at the edges of some or all dust spots.

For this reason we generally do not apply flat field correction on the fly, as was the original design where the camera PCs would immediately flat-field correct and discard the original image. The treatment of the unevenness of the field therefore remains still unresolved.

18.8 Mechanical stability

One of the key design features of the OMX microscope is its mechanical design as described in section 4.3. Strong emphasis was put on maximizing the stage stability and position repeatability. In our general experience this has been successfully achieved: samples stay in focus even over the course of one hour or more and recorded positions of interest can be approached to find the wanted object after the same time span.

The stability is especially important for Structured Illumination data acquisition. Some SIM data sets require more than 1000 exposures spaced out over the course of one hour. The stage drift during that time should be less than the equivalent of one pixel on the CCD, that is, it should be no more than 50 nm. The actual drift occurring during data collection is calculated as a byproduct of the SIM image reconstruction and sometimes the reconstruction fails because there is too much drift. While we do not have any satisfying explanation for this, it seems that waiting a few minutes after the sample is in focus, prior to taking data, helps to alleviate the problem. There might also be a correlation between the measured stage drift and the observed change in room temperature. However, to date this could not be confirmed.

18.9 2 $^1/_2$ D imaging mode

Assuming that the acquisition frame rate is limited by the CCD camera a novel way to acquire 3D information was conceived. Computationally combining two 3D projections, where the second projection is executed while the stage is also laterally moving in synchronous, produces quasi-stereo information as described in section 5.2.4.

Even though a proof-of-principle experiment with beads succeeded, preliminary experiments with GFP-tagged yeast have been discouraging. Apparently the projection integrates background noise to the extent that the GFP signal is being overwhelmed and is effectively too dim to detect. The signal became only strong enough with exposure times above 200 ms.

New laser shutters that can operate at speeds up to 150 Hz and the new model of Andor CCD cameras that can image (sub-fields) up to 100 Hz reduce the interest in this mode. Instead it becomes possible to acquire 3D stacks at rates of 10 Hz. These feature a superior signal-to-noise ratio since there is no integration of out-of-focus noise.

18.10 4D model-based motion dynamics of interphase chromatin

A new approach combining image analysis with a model based molecular dynamics simulation was demonstrated in section 10.6. Resulting chromosome traces appear to fit the images well. However, the current implementation does not yet take full advantage of the time-dimension, i.e. that image data was acquired for many time points. A trace found at time t is used as an initial guess to trace the next image at time $t + 1$.

A more elaborate scheme could be implemented to perform a minimization on the full 4D data set. This could be done by introducing "time-springs" that would interconnect trace-points directly from time t to time $t - 1$ and $t + 1$. A new minimisation parameter would be introduced to control the strength of this new "virtual force". This new force should add a new degree of robustness.

Chapter 19

Materials and methods

Chemicals

All chemicals were bought from Sigma.

19.1 Building the OMX microscope

Software

Part	Description
AutoCAD	AutoCAD Mechanical Desktop (Release 5, Autodesk, Inc., San Rafael, CA)
C++ compiler	Microsoft Visual C++ Toolkit Compiler
Python	Python version 2.4 from `www.python.org`
numarray	Second implementation of Numerical Python from `http://www.stsci.edu/resources/software_hardware/numarray`
SWIG	SWIG version 1.3.24 from `SWIG.org`

Hardware

Part	Description
EMCCD	iXon, Andor Technologies, Belfast, Northern Ireland
Ceramic	ZERODUR®, Schott Glass Technologies *SCHOTT Lithotec AG*, Jena, Germany

flip mirrors	Motorized Flipper (model 8892, New Focus, San Jose, CA)
shutters	programmable laser shutter(model LST200, nm LASER, Sunnyvale, CA)
DSP	DSP - M67 (Innovative Integration, Simi Valley, CA 93065) A4D4 extension
master PC	AMD dual Opteron 252, 2.6 GHz, 4 GB ram, PC tower, with 2 built-in Gigabit Ethernet and PCI-Express video
camera PCs	4 1U rack-mounted Inter 2.6 GHz Pentium-4 PCs, 500 MB ram, single processor
motor PC	Intel PIII desktop PC, 800 MHz, 128 MB ram – needs ISA slot for Nanomover controller card
DSP PC	Intel PIII desktop PC, 800 MHz, 128 MB ram
piezos	MICI 80 SG, piezosystem jena, Inc., Hopedale, MA 01747
OMX xyz stage	model 462-XYZ, Newport, Irvine, CA 92606
optical table	IsoStation VH30-36 W-OPT, Newport
active vibration control	Activator AD500, Newport
optical adjuster	MFM-075, Newport
LMX	M^{2}Bio Quad Stereo, Kramer Scientific, Zeiss Stemi SV 11 APO
LMX touch screen	LCD capacitive touch screen display, PT191MU, Planar Systems, Inc., Beaverton, OR 97006
LMX CCD camera	1024x1024 pixels, 10bit, SKC-141, Ikegami, Tsushinki Co., Ltd., Tokyo, Japan
LMX xy stage	model 462-XY, Newport, Irvine, CA 92606
micro stepper motors	Nanomover, Applied Precision, LLC, Issaquah, WA 98027

flippers	I/O board for flip mirrors and temperature measurements (NI 4351-PCI, National Instruments, Austin, TX 78730)
air filter	HEPA grade .22 μm (air quality is measured to a class 10–100)
dichroic mirrors	custom made by Chroma Technology, Rockingham, VT 05101, USA
beam traps	beam dump PL15, Newport, Irvine, CA 92606
tube lens	Olympus tube lens assemblies
light scrambler	holographic diffuser plate (FWHM 5 deg, Physical Optics, Torrance, CA 90501)
fiber (conv. mode)	conv.ill, Mitsubishi, core size 1mm, NA 0.12)
fiber (SI mode)	core size 100um, NA 0.12, Ceramptec, East Longmeadow, MA
SI phase grating	linear transmission phase grating (custom made by Diffraction Limited, Canada)
SI grating piezo actuator	Queensgate Instruments, Toraquay, UK – close-loop controlled using a capacitive distance sensor(Queensgate Instruments)
SI rotation stage	motorized rotation stage (National Aperture, Salem, NH 03079)
DIC optics motorized stage	TSV Series Precision Z Tower (TSV150DC F05S.1); with UniDrive 6000 Universal Motor Driver/Controller, Newport
spectrometer	Single Fiber Optic Spectrometer (S2000 + ADC2000-PCI), Ocean Optics, Inc. Dunedin, FL 34698

19.2 Protocol for isolation of *Drosophila* primary cell cultures

before starting:

1. Make sterile filtered Chan and Gehring's, add 2% defined FBS
2. Autoclave Dounce homogenizer (7ml) and collection basket (for step 9)
3. Acid clean and thoroughly wash 22x22 mm No1.5 coverslips
4. Coat coverslips with 1 mg/ml poly-L-lysine 1 hr at RT, wash and dry

experiment:

1. Collect embryos for 1 hour (after a one hour pre-collection)
2. Age embryos ≈ 4 hours
3. Rinse embryos into collection vial with water
4. Rinse with water to remove yeast
5. Swirl in 30% bleach for 60s
6. Wash with water 2+ minutes, until all bleach smell is gone
7. Transfer 20–50 μl embryos into 7 ml Dounce filled halfway with media: Chan and Gehring's with 2% defined FBS (make sure that you transfer only embryos and not extraneous fly parts for example adult wings or agar from your collection plate)
8. Homogenize with tight pestle...VERY IMPORTANT....do not twist pestle, just straight up and down four times and VERY IMPORTANT...no bubbles!
9. Using a Pasteur pipet, transfer homogenate through sterile embryo mesh into 15 ml conical
10. Centrifuge at +4 °C in a clinical centrifuge, we use speed 5: it should be pretty gentle, for 5 minutes or less, just to pellet cells
11. Remove supernatant, resuspend pellet in 1–2 ml media, centrifuge as above (again no BUBBLES!)
12. Repeat step 10 and 11
13. Resuspend in ≈ .2 to .5 ml, plate 200 μl per 22x22 mm coverslip (check the density of your culture and then make needed adjustments, i.e. lots of cells on coverslip, but not too dense)

14. Let cells sit 30 minutes and then fix if that is the next step.
15. Fix in PBS*(PBS + 0.1 mM EDTA + 5 mM $MgCl_2$) with 1.6% fresh made formaldehyde 30 minutes at RT or overnight at +4 °C
16. wash 10 minutes 3x in PBS*
17. stain with DAPI 1:1000 dilution of 1 mg/ml stock, 15 minutes at RT
18. wash in PBS* and mount in VectaShield, seal with nail polish or rubber cement

Chan and Gehring's Balanced Saline:

pH to 7.0 before aliquoting and freezing

	g/L
NaCl	3.2
$CaCl_2 \cdot 2\,H_2O$	3.0
$MgSO_4 \cdot 7\,H_20$	0.69
Tricine buffer, pH 7	1.79
Glucose	3.6
Sucrose	17.1
BSA (fraction V)	1.0

filter sterilize, store frozen in 50 ml aliquots

19.3 Protocol for staining *Drosophila* salivary gland squashes

Select third instar larvae from bottles kept at 18 °C. Place larvae on a moist filter paper on a Petri dish whilst preparing the required solutions.

Buffer A 10 x stock solution: 150 mM Tris HCl, pH 7.4, 600 mM KCl, 150 mM NaCl, 5 mM Spermidine, 1.5 mM Spermine

Prep solution: 100 μl 10% Triton X-100, 100 μl 10x buffer A, 800 μl H2O

Fix solution: 100 μl 10% Triton X-100, 100 μl 10x buffer A, 100 μl 37% formaldehyde, 700 μl H2O

Postfix solution: 100 μl 37% formaldehyde, 500 μl glacial acetic acid, 400 μl H2O

Prepare glands quickly in a drop of Prep solution on a slide, transfer glands for 30 sec into a drop of Fix solution and briefly into a drop of Postfix solution on the same slide. Then transfer each lobe separately to 12.5 μl of Postfix solution on an 18x18 mm No. 1 coverslip. Leave glands on coverslip for 3–4 min while preparing another pair of glands. Take up coverslip using a fresh slide and shear glands by sliding the coverslip upside the slide in all directions, taper them with blunt forceps (to the edges of coverslip only) shear them again and squash them by blotting away excess liquid.

Inspect quality of squash at 10x phase 1 and if good enough freeze slide by plunging it into liquid nitrogen. Prie off coverslip with a razor blade from one of its edges, mark the field of squash and the upside of the slide with a diamond pen.

Collect squashes in 96% EtOH for at least 10 min (longer times do not hurt). Wash twice 10 min in buffer A. Incubate for 3 h with first antibody in a moist chamber at RT (alternatively at +4 °C overnight). Wash twice 10 min in buffer A. Incubate for 3 h with second antibody in a moist chamber at RT. Wash twice 10 min in buffer A by adding 0.2 $\mu g/ml$ Hoechst dye to the second wash.

Using a pasteur pipette place a drop of 87% glycerol, 2% (w/v) n-propyl-gallate (dissolves only by warming up solution) onto a 22x22 mm No. 1 cover-slip and dip the slide with the area containing the chromosomes to the drop; blot off the excess of the glycerol/n-propyl-gallate and view immediately or store at $-20\,^{\circ}$C in the dark.

Abbreviations

abbreviation	meaning
3D	three dimensional
CCD	charged-coupled device
DAPI	4',6-diamidino-2-phenylindole
DIC	differential interference contrast
DNA	deoxyribo-nucleic acid
DSP	digital signal processor
DV	DeltaVision wide-field microscope made by API
EM	electron microscopy
EM	electron multiplication
EMCCD	electron multiplying CCD
FITC	fluorescein-isothiocyanat
FLIP	Fluorescence loss in photobleaching
FRAP	Fluorescence recovery after photobleaching
fps	frames per second
GFP	green fluorescent protein
GUI	graphical user interface
NA	numerical aperture
PC	personal computer
pixel	picture element
PSF	point spread function
OTF	object transfer function
CRT	Cathode Ray Tube
SI	structured illumination
TIRF	Total internal reflection fluorescence microscopy

Bibliography

Ernst Abbe. Beiträge zur Theorie des Mikroskops und der Mikroskopischen Wahrnehmung. *Archiv f. Mikroskop. Anat.*, 9:413–468, 1873.

D. A. Agard. *Optical sectioning microscopy: cellular architecture in three dimensions*, volume 13, pages 191–219. Annual Reviews, Inc., 1984.

A Akhtar and P B Becker. Activation of transcription through histone H4 acetylation by MOF, an acetyltransferase essential for dosage compensation in Drosophila. *Mol Cell*, 5(2):367–375, Feb 2000.

Bruce Alberts, Alexander Johnson, Julian Lewis, Martin Raff, Keith Roberts, and Peter Walter. *Molecular biology of the cell.* Garland Science, New York, fourth edition, 2002.

H Bauer and W Beermann. Die Polytänie der Riesenchromosomen. *Chromosoma*, 4:630–648, 1952.

D. M. Beazley. SWIG: an easy to use tool for integrating scripting languages with C and C++. In *Proceedings of the Fourth Annual USENIX Tcl/Tk Workshop*, pages 129–139, 1996.

David Beazley. SWIG and automated C/C++ scripting extensions. *Dr. Dobb's Journal of Software Tools*, 23(2):30, 32, 34–36, 100, February 1998. ISSN 1044-789X.

D.M. Beazley and P.S. Lomdahl. Lightweight computational steering of very large scale molecular dynamics simulations. In *Supercomputing, 1996. Proceedings of the 1996 ACM/IEEE Conference on*, page 50, 1996.

A S Belmont, J W Sedat, and D A Agard. A three-dimensional approach to mitotic chromosome structure: evidence for a complex hierarchical organization. *J Cell Biol*, 105(1):77–92, Jul 1987.

Andrew S Belmont. Mitotic chromosome structure and condensation. *Curr Opin Cell Biol*, 18(6):632–638, Dec 2006.

Eric Betzig, George H Patterson, Rachid Sougrat, O Wolf Lindwasser, Scott Olenych, Juan S Bonifacino, Michael W Davidson, Jennifer Lippincott-Schwartz, and Harald F Hess. Imaging intracellular fluorescent proteins at nanometer resolution. *Science*, 313(5793):1642–1645, Sep 2006.

J Bewersdorf, R Schmidt, and S W Hell. Comparison of I5M and 4Pi-microscopy. *J Microsc*, 222(Pt 2):105–117, May 2006.

Max Born and Emil Wolf. *Principles of Optics*. Cambridge University Press, Cambridge, UK, 6th edition, 1980.

E Boy de la Tour and U K Laemmli. The metaphase scaffold is helically folded: sister chromatids have predominantly opposite helical handedness. *Cell*, 55(6):937–944, Dec 1988.

Paula A Bubulya and David L Spector. "On the move"ments of nuclear components in living cells. *Exp Cell Res*, 296(1):4–11, May 2004.

Alessia Buscaino, Gaelle Legube, and Asifa Akhtar. X-chromosome targeting and dosage compensation are mediated by distinct domains in MSL-3. *EMBO Rep*, 7(5):531–538, May 2006.

M Chalfie, Y Tu, G Euskirchen, W W Ward, and D C Prasher. Green fluorescent protein as a marker for gene expression. *Science*, 263(5148): 802–805, Feb 1994.

Severine Chambeyron and Wendy A Bickmore. Chromatin decondensation and nuclear reorganization of the HoxB locus upon induction of transcription. *Genes Dev*, 18(10):1119–1130, May 2004.

M K Cheezum, W F Walker, and W H Guilford. Quantitative comparison of algorithms for tracking single fluorescent particles. *Biophys J*, 81(4): 2378–2388, Oct 2001.

H. Chen, W. Clyborne, J.W. Sedat, and D. A. Agard. PRIISM: an integrated system for display and analysis of three-dimensional microscope images. In *Biomedical Image Processing and Three-Dimensional Microscopy*, volume 1660, pages 784–790. SPIE, June 1992.

H. Chen, D. D. Hughes, T. A. Chan, J. W. Sedat, and D. A. Agard. IVE (Image Visualization Environment): a software platform for all three-dimensional microscopy applications. *J Struct Biol*, 116(1):56–60, Jan 1996.

Colin G Coates, Donal J Denvir, Noel G McHale, Keith D Thornbury, and Mark A Hollywood. Optimizing low-light microscopy with back-illuminated electron multiplying charge-coupled device: enhanced sensitivity, speed, and resolution. *J Biomed Opt*, 9(6):1244–1252, Nov 2004. Evaluation Studies.

P. F. Dubois, K. Hinsen, and J. Hugunin. Numerical Python. *Computers in Physics*, 10(3):262–267, May/June 1996.

Ann E Ehrenhofer-Murray. Chromatin dynamics at DNA replication, transcription and repair. *Eur J Biochem*, 271(12):2335–2349, Jun 2004.

Yuval Garini, Bart J Vermolen, and Ian T Young. From micro to nano: recent advances in high-resolution microscopy. *Curr Opin Biotechnol*, 16 (1):3–12, Feb 2005.

Susan M Gasser. Visualizing chromatin dynamics in interphase nuclei. *Science*, 296(5572):1412–1416, May 2002.

Gregor D Gilfillan, Tobias Straub, Elzo de Wit, Frauke Greil, Rosemarie Lamm, Bas van Steensel, and Peter B Becker. Chromosome-wide gene-specific targeting of the Drosophila dosage compensation complex. *Genes Dev*, 20(7):858–870, Apr 2006.

Perry Greenfield, Jay Todd Miller, Jin chung Hsu, and Richard L. White. numarray: A New Scientific Array Package for Python. In *PyCon 2003*, 3700 San Martin Dr, Baltimore, MD 21218, 2003. PyCon 2003, Space Telescope Science Institute.

M. Gu and C. J. R. Sheppard. Confocal fluorescent microscopy with a finite-sized circular detector. *J. Opt. Soc. Am. A*, 9(1):151–153, 1992.

M G L Gustafsson. Extended resolution fluorescence microscopy. *Curr Opin Struct Biol*, 9(5):627–634, Oct 1999.

M G L Gustafsson. Surpassing the lateral resolution limit by a factor of two using structured illumination microscopy. *J Microsc*, 198(Pt 2):82–87, May 2000.

M. G. L. Gustafsson, D. A. Agard, and J. W. Sedat. I^5M: 3D widefield light microscopy with better than 100 nm axial resolution. *J. Microsc.*, 195: 10–16, 1999.

M. G. L. Gustafsson, D. A. Agard, and J. W. Sedat. Doubling the lateral resolution of wide-field fluorescence microscopy using structured illumination. In *Three-Dimensional and Multidimensional Microscopy: Image Acquisition Processing VII*, volume 3919, pages 141–150, San Jose, CA, USA, 2000. SPIE.

M G L Gustafsson, L Shao, D A Agard, and J W Sedat. Three-dimensional fluorescence microscopy beyond the diffraction limit using structured illumination. Manuscript in preparation., 2007.

Mats G L Gustafsson. Nonlinear structured-illumination microscopy: wide-field fluorescence imaging with theoretically unlimited resolution. *Proc Natl Acad Sci U S A*, 102(37):13081–13086, Sep 2005.

F A Habermann, M Cremer, J Walter, G Kreth, J von Hase, K Bauer, J Wienberg, C Cremer, T Cremer, and I Solovei. Arrangements of macro- and microchromosomes in chicken cells. *Chromosome Res*, 9(7):569–584, 2001.

B M Hanser, M G L Gustafsson, D A Agard, and J W Sedat. Phase-retrieved pupil functions in wide-field fluorescence microscopy. *J Microsc*, 216(Pt 1):32–48, Oct 2004.

Bridget M Hanser, M G L Gustafsson, David A Agard, and John W Sedat. Phase retrieval for high-numerical-aperture optical systems. *Opt Lett*, 28 (10):801–803, May 2003.

Rainer Heintzmann and Gabriella Ficz. Breaking the resolution limit in light microscopy. *Brief Funct Genomic Proteomic*, 5(4):289–301, Dec 2006.

S. Hell and E. H. K. Stelzer. Properties of a 4Pi confocal fluorescence microscope. *J. Opt. Soc. Am. A*, 9(12):2159–2166, Dec 1992.

P Heun, T Laroche, K Shimada, P Furrer, and S M Gasser. Chromosome dynamics in the yeast interphase nucleus. *Science*, 294(5549):2181–2186, Dec 2001.

Y Hiraoka, J W Sedat, and D A Agard. The use of a charge-coupled device for quantitative optical microscopy of biological structures. *Science*, 238 (4823):36–41, Oct 1987.

E F Y Hom, F Marchis, T K Lee, S Haase, D A Agard, and J W Sedat. AIDA: An Adaptive Image Deconvolution Algorithm with Application to Multi-Frame and Three-Dimensional Data. *J. Opt. Soc. Amer. A*, 24(6): 1580–1600, June 2007.

Erik F.Y. Hom. *Distilling Information from Noisy Data: Examples from Microscopy.* PhD thesis, UCSF, 2006.

C Höppener, D Molenda, H Fuchs, and A Naber. Scanning near-field optical microscopy of a cell membrane in liquid. *J Microsc*, 210(Pt 3):288–293, Jun 2003.

C Höppener, J P Siebrasse, R Peters, U Kubitscheck, and A Naber. High-resolution near-field optical imaging of single nuclear pore complexes under physiological conditions. *Biophys J*, 88(5):3681–3688, May 2005.

Steve B. Howell. *Handbook of CCD Astronomy*, chapter 4. Cambridge University Press, Cambridge, UK, 2000.

J. Huisken, J. Swoger, F. Del Bene, J. Wittbrodt, and E. H. K. Stelzer. Optical sectioning deep inside live embryos by selective plane illumination microscopy. *Science*, 305(5686):1007–1009, 2004.

S. Inoué and H. Sato. *Deoxyribonucleic acid arrangement in living sperm*, pages 209–248. Prentice-Hall, Englewood Cliffs, NJ, 1964.

Shinya Inoué. *Video Microscopy.* Plenum Press, New York, 1989.

Z. Kam, M. Jones, H. Chen, D.A. Agard, and J.W. Sedat. Design and construction of an optimal illumination system for quantitative wide-field multi-dimensional microscopy. *Bioimaging*, 1:71–81, 1993.

Z. Kam, B. Hanser, M. G. L. Gustafsson, D. A. Agard, and J. W Sedat. Computational adaptive optics for live three-dimensional biological imaging. *Proc. Natl. Acad. Sci. U.S.A.*, 98(7):3790–3795, Mar 2001.

Natashe Kireeva, Margot Lakonishok, Igor Kireev, Tatsuya Hirano, and Andrew S Belmont. Visualization of early chromosome condensation: a hierarchical folding, axial glue model of chromosome structure. *J Cell Biol*, 166(6):775–785, Sep 2004. Comparative Study.

T. A. Klar, S. Jakobs, M. Dyba, A. Egner, and S. W. Hell. Fluorescence microscopy with diffraction resolution barrier broken by stimulated emission. *Proc. Natl. Acad. Sci. U.S.A.*, 97(15):8206–8210, 2000.

Andrei Korostelev, Richard Bertram, and Michael S Chapman. Simulated-annealing real-space refinement as a tool in model building. *Acta Crystallogr D Biol Crystallogr*, 58(Pt 5):761–767, May 2002.

I V Kotlikova, O V Demakova, V F Semeshin, V V Shloma, L V Boldyreva, M I Kuroda, and I F Zhimulev. The Drosophila dosage compensation complex binds to polytene chromosomes independently of developmental changes in transcription. *Genetics*, 172(2):963–974, Feb 2006.

U Kubitscheck, P Wedekind, O Zeidler, M Grote, and R Peters. Single nuclear pores visualized by confocal microscopy and image processing. *Biophys J*, 70(5):2067–2077, May 1996.

Fang Li, David A D Parry, and Maxwell J Scott. The amino-terminal region of Drosophila MSL1 contains basic, glycine-rich, and leucine zipper-like motifs that promote X chromosome binding, self-association, and MSL2 binding, respectively. *Mol Cell Biol*, 25(20):8913–8924, Oct 2005.

P S Maddox, K S Bloom, and E D Salmon. The polarity and dynamics of microtubule assembly in the budding yeast Saccharomyces cerevisiae. *Nat Cell Biol*, 2(1):36–41, Jan 2000.

Kazuhiro Maeshima and Ulrich K Laemmli. A two-step scaffolding model for mitotic chromosome assembly. *Dev Cell*, 4(4):467–480, Apr 2003.

A Mallavarapu, K Sawin, and T Mitchison. A switch in microtubule dynamics at the onset of anaphase B in the mitotic spindle of Schizosaccharomyces pombe. *Curr Biol*, 9(23):1423–1426, Dec 1999.

Sascha Mendjan, Mikko Taipale, Jop Kind, Herbert Holz, Philipp Gebhardt, Malgorzata Schelder, Michiel Vermeulen, Alessia Buscaino, Kent Duncan, Juerg Mueller, Matthias Wilm, Henk G Stunnenberg, Harald Saumweber, and Asifa Akhtar. Nuclear pore components are involved in the transcriptional regulation of dosage compensation in Drosophila. *Mol Cell*, 21(6): 811–823, Mar 2006.

M. Minsky. US patent 3,013,467: Microscopy apparatus, Dec. 19, 1961.

W C Moss, S Haase, J M Lyle, D A Agard, and J W Sedat. A novel 3D wavelet-based filter for visualizing features in noisy biological data. *J Microsc*, 219(Pt 2):43–49, Aug 2005.

Chi-Yun Pai, Elissa P Lei, Dolanchanpa Ghosh, and Victor G Corces. The centrosomal protein CP190 is a component of the gypsy chromatin insulator. *Mol Cell*, 16(5):737–748, Dec 2004.

G Patterson, R N Day, and D Piston. Fluorescent protein spectra. *J Cell Sci*, 114(Pt 5):837–838, Mar 2001.

J R Paulson and U K Laemmli. The structure of histone-depleted metaphase chromosomes. *Cell*, 12(3):817–828, Nov 1977.

Eric F Pettersen, Thomas D Goddard, Conrad C Huang, Gregory S Couch, Daniel M Greenblatt, Elaine C Meng, and Thomas E Ferrin. UCSF Chimera–a visualization system for exploratory research and analysis. *J Comput Chem*, 25(13):1605–1612, Oct 2004.

Michael G Poirier and John F Marko. Mitotic chromosomes are chromatin networks without a mechanically contiguous protein scaffold. *Proc Natl Acad Sci U S A*, 99(24):15393–15397, Nov 2002.

Lisa H Pope, Chee Xiong, and John F Marko. Proteolysis of mitotic chromosomes induces gradual and anisotropic decondensation correlated with a reduction of elastic modulus and structural sensitivity to rarely cutting restriction enzymes. *Mol Biol Cell*, 17(1):104–113, Jan 2006.

D C Prasher, V K Eckenrode, W W Ward, F G Prendergast, and M J Cormier. Primary structure of the Aequorea victoria green-fluorescent protein. *Gene*, 111(2):229–233, Feb 1992.

L Rastelli, R Richman, and M I Kuroda. The dosage compensation regulators MLE, MSL-1 and MSL-2 are interdependent since early embryogenesis in Drosophila. *Mech Dev*, 53(2):223–233, Oct 1995.

Barbara P Rattner and Victoria H Meller. Drosophila male-specific lethal 2 protein controls sex-specific expression of the roX genes. *Genetics*, 166 (4):1825–1832, Apr 2004.

Michael J Rust, Mark Bates, and Xiaowei Zhuang. Sub-diffraction-limit imaging by stochastic optical reconstruction microscopy (STORM). *Nat Methods*, 3(10):793–795, Oct 2006.

Daniel Sage, Franck R Neumann, Florence Hediger, Susan M Gasser, and Michael Unser. Automatic tracking of individual fluorescence particles: application to the study of chromosome dynamics. *IEEE Trans Image Process*, 14(9):1372–1383, Sep 2005. Evaluation Studies.

Meredith Johnson Sagolla, Satoru Uzawa, and W Zacheus Cande. Individual microtubule dynamics contribute to the function of mitotic and cytoplasmic arrays in fission yeast. *J Cell Sci*, 116(Pt 24):4891–4903, Dec 2003.

Schott AG. Product information, 2006. `http://www.us.schott.com/optics_devices/english/products/zerodur`.

J Sedat and L Manuelidis. A direct approach to the structure of eukaryotic chromosomes. *Cold Spring Harb Symp Quant Biol*, 42 Pt 1:331–350, 1978.

S Shah, E F Y Hom, S Haase, K Yonekura, D A Agard, and J W Sedat. A fully automatic 2D method for CTF estimation for cryo- and cryo-tomographic EM images. Manuscript in preparation., May 2006a.

S Shah, E F Y Hom, S Haase, K Yonekura, D A Agard, and J W Sedat. Edge preserving deconvolution for cryo-Electron Microscopy. Manuscript in preparation., July 2006b.

Nathan C Shaner, Paul A Steinbach, and Roger Y Tsien. A guide to choosing fluorescent proteins. *Nat Methods*, 2(12):905–909, Dec 2005.

Lin Shao. *Ultra-High Resolution Fluorescence Microscopy and Its Application in Biology.* PhD thesis, UCSF, 2005.

E R Smith, A Pannuti, W Gu, A Steurnagel, R G Cook, C D Allis, and J C Lucchesi. The drosophila MSL complex acetylates histone H4 at lysine 16, a chromatin modification linked to dosage compensation. *Mol Cell Biol*, 20(1):312–318, Jan 2000.

Thorsten Staudt, Marion C Lang, Rebecca Medda, Johann Engelhardt, and Stefan W Hell. 2,2'-thiodiethanol: a new water soluble mounting medium for high resolution optical microscopy. *Microsc Res Tech*, 70(1):1–9, Jan 2007.

E. H. K. Stelzer and S. Lindek. Fundamental reduction of the observation volume in far-field light-microscopy by detection orthogonal to the illumination axis - confocal theta microscopy. *Opt. Comm.*, 111(5-6):536–547, 1994.

Tobias Straub, Ina K Dahlsveen, and Peter B Becker. Dosage compensation in flies: mechanism, models, mystery. *FEBS Lett*, 579(15):3258–3263, Jun 2005.

E Stubblefield and W Wray. Architecture of the Chinese hamster metaphase chromosome. *Chromosoma*, 32(3):262–294, 1971.

A T Sumner. Scanning electron microscopy of mammalian chromosomes from prophase to telophase. *Chromosoma*, 100(6):410–418, Jul 1991.

Jason R Swedlow and Tatsuya Hirano. The making of the mitotic chromosome: modern insights into classical questions. *Mol Cell*, 11(3):557–569, Mar 2003.

Jason R Swedlow and Melpomeni Platani. Live cell imaging using wide-field microscopy and deconvolution. *Cell Struct Funct*, 27(5):335–341, Oct 2002.

Jason R. Swedlow, John W. Sedat, and David A. Agard. *Deconvolution in optical microscopy*, pages 284–309. Academic Press, Inc., Orlando, FL, USA, 2nd edition, 1997. ISBN 0-12-380222-9.

Maya Topf and Andrej Sali. Combining electron microscopy and comparative protein structure modeling. *Curr Opin Struct Biol*, 15(5):578–585, Oct 2005.

Guido van Rossum. Python library reference. Report CS-R9524, Centrum voor Wiskunde en Informatica, P. O. Box 4079, 1009 AB Amsterdam, The Netherlands, April 1995.

J Vazquez, A S Belmont, and J W Sedat. Multiple regimes of constrained chromosome motion are regulated in the interphase Drosophila nucleus. *Curr Biol*, 11(16):1227–1239, Aug 2001.

Julio Vazquez, Andrew S Belmont, and John W Sedat. The dynamics of homologous chromosome pairing during male Drosophila meiosis. *Curr Biol*, 12(17):1473–1483, Sep 2002.

Julio Vazquez, Martin Muller, Vincenzo Pirrotta, and John W Sedat. The Mcp element mediates stable long-range chromosome-chromosome interactions in Drosophila. *Mol Biol Cell*, 17(5):2158–2165, May 2006.

Musundi B Wabuyele, Mustafa Culha, Guy D Griffin, Pierre M Viallet, and Tuan Vo-Dinh. Near-field scanning optical microscopy for bioanalysis at nanometer resolution. *Methods Mol Biol*, 300:437–452, 2005.

W Wallace, L H Schaefer, and J R Swedlow. A workingperson's guide to deconvolution in light microscopy. *Biotechniques*, 31(5):1076–1078, Nov 2001.

E Wang, C M Babbey, and K W Dunn. Performance comparison between the high-speed Yokogawa spinning disc confocal system and single-point scanning confocal systems. *J Microsc*, 218(Pt 2):148–159, May 2005. Evaluation Studies.

Wikipedia. Optical microscope — wikipedia, the free encyclopedia, 2006a. [Online; accessed 22-August-2006].

Wikipedia. Nuclear pore — wikipedia, the free encyclopedia, 2006b. [Online; accessed 3-November-2006].

Wikipedia. Angular resolution — wikipedia, the free encyclopedia, 2006c. [Online; accessed 1-October-2006].

Wikipedia. Electron-multiplying CCD — wikipedia, the free encyclopedia, 2006d. [Online; accessed 27-August-2006].

Katrin I Willig, Silvio O Rizzoli, Volker Westphal, Reinhard Jahn, and Stefan W Hell. STED microscopy reveals that synaptotagmin remains clustered after synaptic vesicle exocytosis. *Nature*, 440(7086):935–939, Apr 2006.

T. Wilson. The role of the pinhole in confocal imaging system. In J. B. Pawley, editor, *Handbook of Biological Confocal Microscopy*. Plenum Press, New York, 1995.

I F Zhimulev. Morphology and structure of polytene chromosomes. *Adv Genet*, 34:1–497, 1996. Historical Article.

Timo Zimmermann. Spectral imaging and linear unmixing in light microscopy. *Adv Biochem Eng Biotechnol*, 95:245–265, 2005.

Timo Zimmermann, Jens Rietdorf, and Rainer Pepperkok. Spectral imaging and its applications in live cell microscopy. *FEBS Lett*, 546(1):87–92, Jul 2003.

Curriculum Vitae

Sebastian Haase
born 2nd November, 1974, in Stadthagen, Germany

Academic Education and Degrees

2003-07	PhD program in Biology, Humboldt-University, Berlin, Germany
1999	Diplom in Physics, University of Konstanz, Germany
1996	Vordiplom, University of Tübingen, Germany
1994	Abitur, Ratsgymnasium Stadthagen, Germany

Professional Employment

2001-07	Programmer Analyst, Department of Biochemistry and Biophysics, Development of novel high-resolution microscope system, University of California, San Francisco
2000-01	System and Network Administrator, Web-Engineer at ARTEMIA, San Francisco, CA, USA
1998-99	Assistant System Admin, Department of Physics, University Konstanz
1996-99	Assistant Research Programmer, Object-Oriented Database development (Java), Department of Informatics, University Konstanz
1994-96	Assistant Research Programmer, Text analysis, Department of Informatics, University Tübingen

Publications

Haase S., Frisch H.L., Nielaba P. Quantum Corrections for the liquid-gas transition of Lennard-Jones particles in two dimensions, Phys.Rev E, 69,012501, Jan 2004.

Moss WC, Haase S, Lyle JM, Agard DA, Sedat JW. A novel 3D wavelet-based filter for visualizing features in noisy biological data. J Microsc, 219(Pt 2):43-49, Aug 2005.

Hom EFY, Marchis F, Lee TK, Haase S, Agard DA, Sedat JW. AIDA: An Adaptive Image Deconvolution Algorithm with Application to Multi-Frame and Three-Dimensional Data. J. Opt. Soc. Amer. A 24 (6), 1580-1600.

Patent Application

W.Moss, S.Haase, J.W.Sedat. 3D Wavelet-based Filter.

Selbstständigkeitserklärung

Hiermit versichere ich, daß ich die vorliegende Arbeit selbständig verfaßt und keine anderen als die angegebenen Quellen und Hilfsmittel verwendet habe.

Berlin, June 20, 2007

Sebastian Haase